

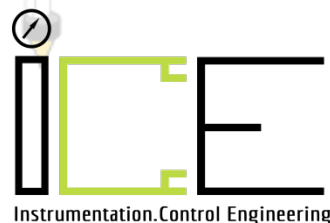


Universiti
Malaysia
PAHANG
Engineering • Technology • Creativity

**Addie Irawan,
Mohd Helmi Suid
Saifudin Razali (Eds.)**

PROCEEDING OF COLLOQUIUM ON ROBOTICS, UNMANNED SYSTEMS AND CYBERNETICS 2014

**November 20 2014, Faculty of Electrical & Electronics Engineering
Universiti Malaysia Pahang, Pekan, Pahang, MALAYSIA**

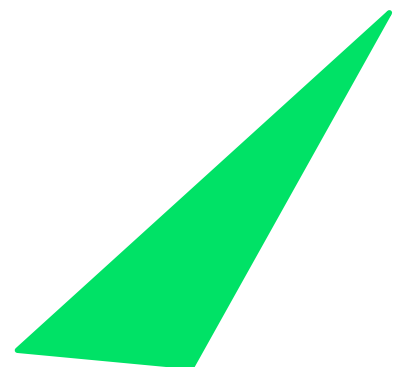




PROCEEDING OF COLLOQUIUM ON ROBOTICS, UNMANNED SYSTEMS AND CYBERNETICS 2014

**NOVEMBER 20 2014, FACULTY OF ELECTRICAL & ELECTRONICS ENGINEERING
UNIVERSITI MALAYSIA PAHANG, PEKAN, PAHANG, MALAYSIA**

**Editors:
Addie Irawan
Mohd Helmi Suid
Saifudin Razali**



Copyright© Penerbit Universiti Malaysia Pahang

First Print 2015

All rights reserved. No part of this publication may be reproduced, stored in a retrieval system, or transmitted, in any form or by any means, electronic, mechanical, photocopying, recording or otherwise without the prior written permission of the publisher, Penerbit Universiti Malaysia Pahang.

Perpustakaan Negara Malaysia

Cataloguing-in-Publication Data

Colloquium On Robotics, Unmanned Systems & Cybernetics (2014: Pekan, Pahang)
PROCEEDING OF COLLOQUIUM ON ROBOTICS, UNMANNED
SYSTEMS & CYBERNETICS 2014, NOVEMBER 20 2014, Faculty of
Electrical & Electronics Engineering Universiti Malaysia Pahang, Pekan,
Pahang, Malaysia.
ISBN 978-967-0691-42-8
1. Robotics--Congresses 2. Cybernetics--Congresses.
I. Title.
629.892

Published by:

PENERBIT UNIVERSITI MALAYSIA PAHANG,
Universiti Malaysia Pahang,
Lebuhraya Tun Razak,
Pahang Darul Makmur.
Tel: 09-5493320 Faks: 09-5493381

Printed by:

Anugerah Ilham Management & Services (CA 00558226 W)
B-44, Tingkat 1, Lorong IM5/2, Persiaran Sultan Abu Bakar, Indera Mahkota 5,
25200 Kuantan, Pahang Darul Makmur.
Tel: 09-5733175/3177 Fax: 09-5733176

CRUSC 2014 Organizing Committee

Advisor

Assoc.Prof Dr. Kamarul Hawari Ghazali

Organizing Chair

Dr. Addie Irawan Hashim

Program Chair

Dr. Mohammad Fadhil Abas

Finance Chair

Dr. Zainah Md. Zain

Publication Chair

Dr. Mohd Razali Daud

Promotion Chair

Mohd Helmi Suid

Secretariat

Assoc. Prof. Dr. Hamzah Ahmad

(Program Advisor)

Mohd Zaidi Mohd Tumari (Promotion –
Graphic Design)

Mohd Falfadzli Jusoh (Promotion –
Graphic Design)

Dr. Saifudin Razali (Promotion – Logistic)

Dr. Dwi Pebrianti (Publication – Peer-
review)

Maziyah Md. Noh (Program -
Organization)

Siti Nurbadri Sheikh Ismail (Finance)

Salmiah Salim (Program – Desk
management)

Table of Content

CONTENT	PAGE
Introduction	i
Summary on Plenary Session: Session 1	ii
Summary on Plenary Session: Session 2	iii
Presented Papers	
Cooperative Positioning of Multiple AUVs for Underwater Docking: A Framework	1-6
Classification of Ammonia Odor-profile Using k-NN Technique	7-11
Classification of Ammonia in water for Oil and Gas Industry using Case Based Reasoning (CBR)	12-16
An Experimental Study Of Combinational Logic Circuit Minimization Using Firefly Algorithm	17-21
An Analysis of γ effects to H_{∞} Filter based Localization	22-27
Gaharu Sensor: Classification Using Case Based Reasoning (CBR)	28-31
Gravitational Search Algorithm for Assembly Sequence Planning	32-36
An Approach to Reduce Computational Cost for Localization Problem	37-43
Comparison of Manually-Designed and Automatically-Evolved Hybrid Articulated-Wheeled Robot	43-47
Multiple Non-Identical Four DC Motor Synchronous Speed Control: Initial Hardware and Control Scheme	48-51
CFD Analysis For Moving Rigid Body in The High Tidal Environment of Sea-bed	52-55
Combination of Transverse-Trot Gait Pattern for Quadruped Walking Robot	56-60
Combining Tree-based Genetic Programming with Pareto Multi-Objective Optimization for Evolving Modular Robots	61-66
A Study of Drift Force on Submerged Body in X4-AUV Development	67-70
Backstepping Approach for Underactuated System	71-75
3D Image Construction Using Single LRF Hokuyo URG-04LX	76-79
Simulation Study Of Space Robot Dynamics	80-85

Introduction

Colloquium on Robotics, Unmanned Systems and Cybernetics 2014 (CRUSC 2014) is one of the initiatives from **Robotics and Unmanned System (RUS)** research group under the **Instrumentation and Control Engineering (iCE)** Cluster, **Faculty of Electrical & Electronics Engineering**, Universiti Malaysia Pahang (UMP) to bring together the researchers that related to the field of robotics, unmanned systems and cybernetics. In this first CRUS event the targeted is to bring majority participants among the **undergraduates** and **postgraduate** under related research/focus group to submit **research papers, concept papers, technical report or undergraduate final year project report**. This first event is going to be held at Faculty of Electrical & Electronics Engineering, Universiti Malaysia Pahang, Pekan, Pahang on **November 20, 2014** as a part of the **FKEE Visiting Professor Lectures and Keysight Technologies Advanced Laboratory Opening Ceremony** event.

Topics (not limited)

Robotics & Unmanned Systems

Robot mechanism and control, Supervision Systems, Underactuated systems and control, Legged/Multi-legged systems, Tele-robotics and Tele-operation, Unmanned and autonomous vehicle technology, Human- Robots Interfaces, Network robotics, Intelligent transportation technologies, Space and Underwater robots, Robot modelling, Simulation and system architecture, Human-machine interfaces, Collective and social robots, Humanoid robots, Cognitive approach for robotics, Mechatronics systems, Virtual environment, Virtual and Augmented Reality, Perception and awareness; Surveillance, fault detection and diagnosis; Robotics in medical, Bioinspired/Biomimetic systems.

Cybernetics & Informatics

Agent-Based modelling, Artificial immune systems, Artificial life, Swarm intelligence, Optimization and evolutionary computation, Biometric systems/Bioinformatics, Computational Life Science, Cybernetics for informatics, Evolutionary computation, Expert and knowledge-based systems, Information assurance and intelligent multimedia computation, Heuristic algorithms, Hybrid models of Neural Network, Image processing/pattern recognition, Fuzzy systems and its applications, Knowledge acquisition in Intelligent, Machine vision, Self-Organization.

Summary on Plenary Session: Session 1



Professor Dr. Shamsudin Mohd Amin

CAIRO, Materials and Manufacturing Research Alliance, Universiti Teknologi Malaysia

Topic: An Experimental Approach in Designing Multi-Robot Systems

Abstract:

There are many pertinent issues and complex challenges confronting the robotics community at large. It could be in the form of the complex mechanisms required to accomplish some required tasks, or it could be in the form of advanced architectures of the controllers to emulate intelligence levels in the decision making processes, or in the challenges in the communication technologies being deployed. The multi-robot approach can be further extended into multi-team robot systems deploying homogeneous and heterogeneous robots at the same time. Issues such as robot team interaction and inter-robot communications become forefront challenges to be overcome by the robotics community. Several approaches have been introduced in designing robotic systems. The design methodologies could be classified as ethological guided/constraint approach, situated activity design approach, experimentally driven design approach. In this presentation, we attempt to share the experimentally driven design approach in building various generations of mobile robots leading to the intelligent multi robot systems for specific task achievement, i.e. transferring oversized objects. A step by step development and testing is presented, supported by video clip presentations of the experiments.

Biography:

Professor Shamsudin is currently Professor of Robotics at Faculty of Electrical, Universiti Teknologi Malaysia (UTM) under the Department of Control and Mechatronics Engineering and CAIRO in Materials and Manufacturing Research Alliance. He has involved, chaired and founded in several professional bodies such as Asian Mechatronics Association, Malaysian Society for Engineers and Technologies (MySET), Instrumentation and Control Society of Malaysia (ICSM), Institute of Electrical and Electronics Engineers, Malaysia Section (2001), Asian Control Professors Association (ACPA) and Robotics and Automation Association of Malaysia (RAAM). Detail about professor can be found at <http://www.cairo.utm.my/cairo/>

Summary on Plenary Session: Session 2



Assoc. Prof. Dr. Mohd Rizal Arshad

Underwater Control and Robotics Research Group (UCRG), Universiti Sains Malaysia

Topic: Where am I? The Problem of Localisation and Mapping In The Ocean

Abstract:

One major obstacle in operating an autonomous underwater robotics platform in the ocean is the question of localisation and mapping. The turbidity, damping and turbulent characteristics of the ocean waves limit the utilization of electromagnetic signals which are pervasively used for terrain or land applications. GPS and RF signals are attenuated significantly. Optical signal faces the problem of high reflectivity which hinders the distance of signal penetration. Hence, the option boiled down to acoustic signal which in itself is saturated with noise. Hence, the talk will embark to discuss some related issues and potential solutions.

Speaker Detail:

Dr. Mohd Rizal Arshad is currently an Associate Professor and the deputy dean of the School of Electrical and Electronic Engineering, Universiti Sains Malaysia and with his team of researcher, is also the pioneer of underwater system technology research efforts in Malaysia. The main project for the research group is the development of a fleet of underwater robotics platform that covers nearly the whole water column, i.e. to a maximum depth of 500m. This fleet of underwater robotics platforms consists of, among others, an underwater glider and vertical profiler system. He has also been involved with a number of industry-based research projects such as the development of an intelligent culvert inspection system for highway inspection, and the development of Techno-Centre in one of the technology park in Malaysia. Dr. M.R.Arshad is very interested in investigating the fusion of the natural world with the modern engineering pool of knowledge. This is the reason his group has embarked on the bio-inspired research efforts and the utilization of nature to complement the current robotics system. The multi-disciplinary nature of the research scope is reflected in the groups' researchers whom came from different technical background. The research group is also currently the secretariat of the National Underwater Research Network (NURN), for Malaysia. His group website is available at <http://urrg.eng.usm.my/>

**Organized by: Robotics and Unmanned Systems (RUS) group,
Partial of Instrumentation and Control Engineering (iCE) Cluster annual activities**

Cooperative Positioning of Multiple AUVs for Underwater Docking: A Framework

M. H. A. Majid¹, M. F. Yahya¹, S. Y. Siang¹ and, M. R. Arshad¹

¹ Underwater, Control, and Robotic Group, School of Electrical and Electronic Engineering, Engineering Campus, Universiti Sains Malaysia, 14300 Nibong Tebal, Penang, Malaysia.
(E-mail: helmi_mjd@yahoo.com¹)

Abstract – Underwater docking is important for battery recharging and retrieving the AUV after deployment. Accurate docking system required accurate positioning system. In this paper, a framework of a sophisticated docking system is proposed for multiple AUVs operation with swarm of ASVs platform as the position guidance. This system is divided into three major subsystems namely underwater localization system, ASVs cooperative system and underwater docking system. It is expected that this system could lead to a reliable, flexible and portable AUVs operation for underwater tasking such as underwater surveying and monitoring.

Keywords – cooperative navigation, swarm localization, AUV docking, ASV, underwater monitoring.

1. Introduction

Developments of the underwater vehicles have improved method of underwater surveying, monitoring and tasking technique. However, there are many challenges remain to be resolved for technology maturity and operating reliability such as underwater communication, vehicle positioning, data transfer and vehicle power sources. Cooperation of multiple AUVs has recently grabbed the researcher attention because it provides an improved performance in terms of area of coverage, data accurateness and task completing capability. In this paper, we will cover three major sections of the aforementioned problems which are underwater localization, cooperative AUVs and underwater docking for power recharging. Thus, a review on these three areas of research will be presented in this section to evaluate their research state of art.

Underwater localization or positioning is very important for underwater operation especially after deployment of the underwater deployment. There are three common principles used for underwater positioning known as ultra-short base line (USBL) or sometimes called as super-short base line (SSBL), short base line system (SBL) and long base line system (LBL). In addition, GPS intelligent buoy (GIB) is known as the latest technology used for underwater positioning system. However, these methods of positioning are solely depending on the fixed beacon or limited range of baseline. Basically, position estimation is based on time-

of-arrival (TOA) or time-of-flight (TOF) estimation of the acoustic signals operated between a transponder and a transducer array placed on the vehicle [1].

Swarm robotics is a new approach to the coordination of multirobot systems which consist of large numbers of robots [2]. An example of swarm robot used for localization applications are autonomous quadcopter swarm robots for object localization and tracking [3] and localization using triangulation in swarms of autonomous rescue robots [4]. In addition, swarm robot also used for target's position estimation [5], deployment and localization of the sensor nodes [6], surveillance, target acquisition, and tracking [7] and last but not least for distributed simultaneous localization and mapping (SLAM) [8]. A unique example of swarm robot for underwater application is acoustical signal tracking for underwater mobile robots [9]. However, swarm robot for underwater application is still lack of research attention and most available implementation used a single ASV to support AUVs navigation [10, 11]. Despite of using only one ASV, two ASVs were used and general framework was developed for cooperative navigation in [12].

There are many ideas of AUV cooperative navigation has been published. The idea of cooperative positioning using range-only measurements between survey AUV and beacon AUV is one of those ideas [13]. Survey AUV is equipped with sensors required for survey whereas beacon AUV is equipped with high accuracy navigational sensor. By using acoustic communication, beacon AUV helps the survey AUV to improve its positional accuracy by sharing its own location to survey AUV periodically. Then, the survey AUV will estimate its distance from beacon AUV by measuring the propagation delay of the acoustic signal. By using this information, the survey AUV is able to reduce error of position estimated in the radial direction of the ranging circle centered at beacon AUV. However, the error in the tangential direction remains unchanged. Commonly, the members of a group of AUVs exchange navigation information with one another so as to improve their individual position estimates [14].

In Moving Long Baseline (MLBL) system, two AUVs are used as mobile beacon nodes [15]. They are configured with high accuracy navigation system. These two mobile beacons are positioned on the sides and at the rear of the other AUVs to form the moving baseline array. The mobile beacons will resurface to obtain GPS

data periodically. All the vehicles will synchronize to GPS time before submerge. The mobile beacon will give out a pre-scheduled ping followed by its own position. Upon reception of the ping, the other AUVs will be able to calculate their range to the mobile beacon. They will use this range information to correct their prediction of position. An alternative approach which integrates position information of other vehicles to reduce the error and uncertainty of the on-board position estimates of the AUV without going for surfacing. This approach uses the acoustic modem to exchange vehicle localization estimates while simultaneously estimating inter-vehicle range [16].

Multiple AUVs cooperative system has the advantage of allowing AUVs to work together on a common goal without involvement of human action. Every AUV in the system, however, does not have plenty of energy and limited amount of data storage. By using a ship or surface vessel to recover each and every AUV will skyrocket mission costs. Therefore, a mobile or floor-standing station is a better approach to realize a longer AUV mission execution while cutting additional costs needed to send a ship to retrieve the AUVs. As an AUV recharges its battery and transmits or get data through the station, the capability of the AUV to autonomously docks inside the station is of importance.

There are many research had been conducted in developing docking methods for cruising AUVs, most notably on REMUS100 as described in [17, 18]. As for the station types, although a mobile station is easily manageable as highlighted in [19], a floor-standing station is more scalable as explained in [20]. In contrast to cruising AUV, reports on docking methods for hovering AUV are limited but still available as shown in [21]. In short, a lot of research had been devoted into polishing docking technique for single AUV, but to date, there is no research has been done on the docking of multiple AUVs. Apart from discerning localization and multiple AUVs cooperative methods, this paper also proposes a novel docking method for multiple hovering AUVs on solving the issue of power limitation.

2. System Structure

2.1 Overall System

The overall system of the proposed method is illustrated in Fig. 1. This system consists of three subsystems namely underwater localization system, AUV cooperative navigation system and underwater docking system. The overall process of the system is described in the block diagram as shown in Fig. 2 and Fig. 3.

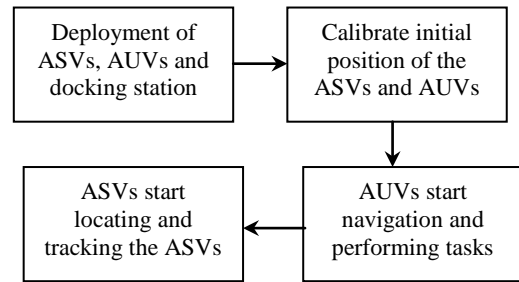


Fig.2. Initialization process

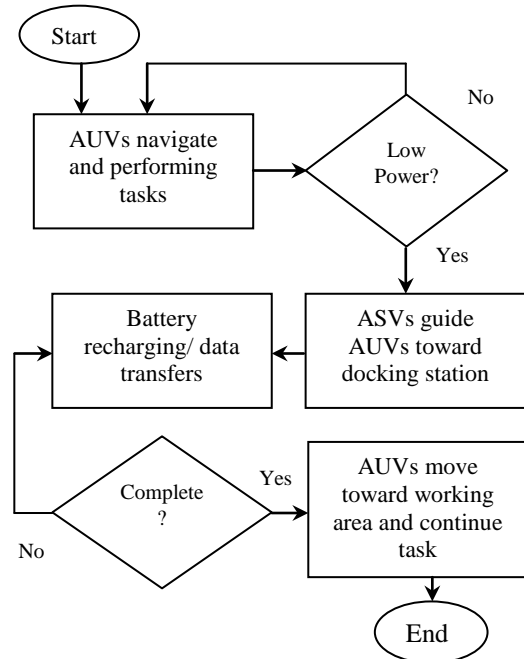


Fig. 3. Docking process

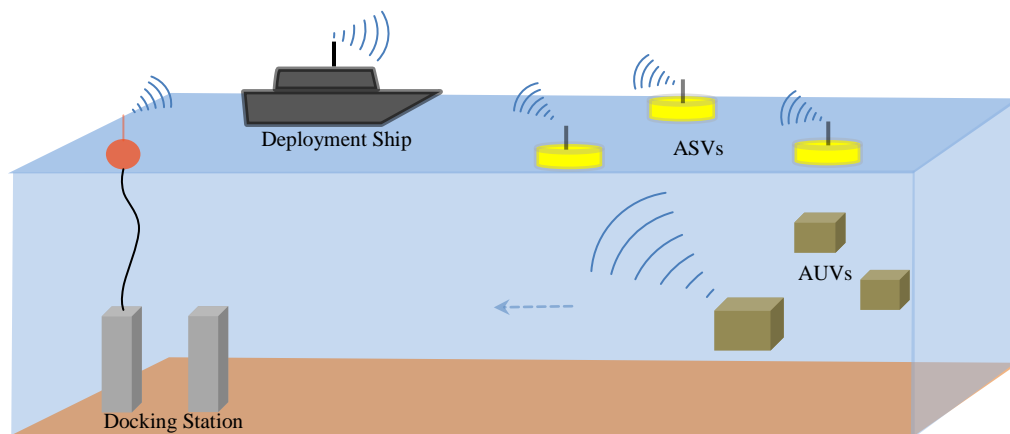


Fig. 1. Overall system illustration

From Fig. 2, the process starts by deploying the ASVs, AUVs and docking station by the deployment ship. Once the deployment is done, the initial position of the AUVs and ASVs is calibrated using the attached GPS system. The position of the docking station is also recorded. Once the initial position is recorded, the AUVs now can start cooperative navigation and performing their task accordingly. At the same time, ASVs will track the position of the AUVs from the surface and report it to the deployment ship. This process continue until any AUVs encounter low power or need to transfer data to the deployment ship as demonstrated in Fig. 3. Once the AUV send signal of low power to the ASVs, the ASVs will guide the AUVs towards the docking station. After completing power charging or data transfer, ASVs will guide the AUVs back to the working area to continue their task. The detail of each system involves will be explained in the next section of this paper.

2.2 Cooperative Localization System

Self-localization of an underwater vehicle is particularly challenging due to the absence of Global Positioning System (GPS) reception or features at known positions that could otherwise have been used for position computation. Thus, we proposed ASVs swarming as a solution for invisibility of the GPS in underwater environment. By using a swarm robotic platform which equipped with GPS and acoustic devices, underwater positioning is possible.

A. AUV Positioning

The proposed concept underwater localization is illustrated in Fig. 2. Note that the localization only involves a leader of the AUVs to be tracked by the swarm ASVs. The master-follower concept implemented in the cooperative AUVs reduced the complexity of the tracking system. In this case, the positions of the other AUVs are locally measured with respect to the AUV master using acoustic modem. The detail explanation of this principle will be explained in the next section. Referring to Fig. 2, acoustic signal with specified bandwidth emitted by the AUV (Master) are detected and measured by the hydrophone attached to each of the ASVs.

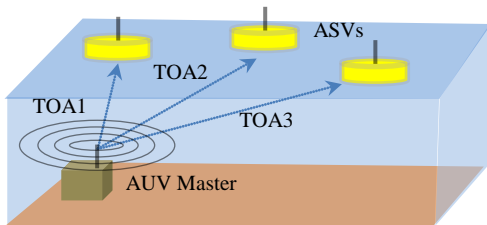


Fig. 2. Illustration of the acoustic signal retrieving

Time of arrival (TOA) of the acoustic signal is recorded by the ASVs internal processor and timer. The value for at least three TOA from at least three ASVs will be recorded. The three values of the TOA will be used by the processor to perform triangulation of the incoming

signals. The position of each of the ASV is determined by the GPS attached on board. Thus, the accuracy of the position measurement depends on the accuracy of the GPS used to locate the position for each of the ASV.

From the triangulation process, the position of the ASV is determined with respect to the earth coordinate. The triangulation algorithm is instilled in every ASV so that each of them could perform triangulation based on the set condition. Each of the ASV will shared the TOA value among each other wirelessly. After comparison is made the ASV with large TOA will perform triangulation process and will inform other ASVs about the location of the AUV. This approach avoids the position reporting from all ASV at the same time and caused information overlapping. Finally, all ASVs will move according to the computed coordinate. This method might take several microseconds before location is confirmed depending on the processing speed and the accuracy of the timer.

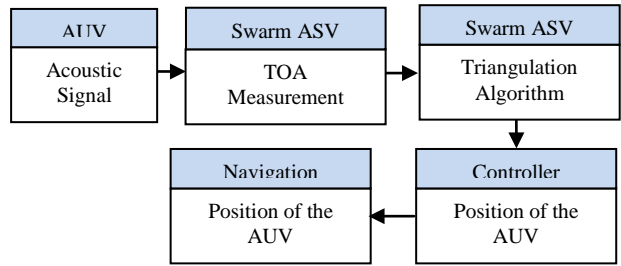


Fig. 3. Overall localization process

B. AUV Tracking

Once the position of the AUV is known, the ASVs will move towards the latest updated AUV's location based on the navigation control block diagram shown in Fig. 4. The updated position will also be send to the deployment ship for monitoring purpose. The swarm ASV should update the position of the AUV every certain period of time to avoid loss of tracking. In this case, ASVs have dual function which are localizing the AUV and track the AUV as it is moving. The position calculated by triangulation method as discussed earlier will be used for tracking the AUV. Compass will direct the ASV towards the AUV position in the close loop system.

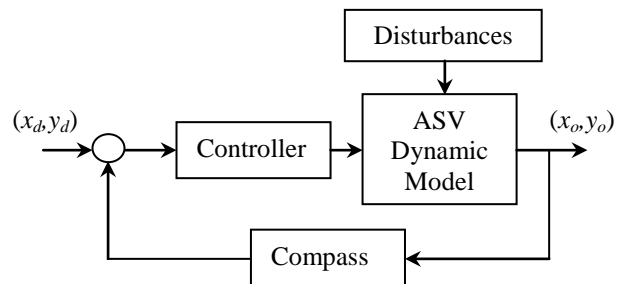


Fig. 4. Control block diagram of the ASV navigation

This process will take place to guide the AUV to the docking station. This localization and tracking just take

place in the global scope from docking system point of view. Once the AUVs are assisted close to the docking station, the positioning system is change from acoustic-based positioning to vision-based positioning (in local scope of the docking system). The detail of the procedure will be discussed in the next section.

C. Advantages and Disadvantages

The proposed method has advantages in term of flexibility, robustness and scalability as possess by the swarm robotic system. In addition, this method of localization could reduce operating cost, avoid prolong human operator and covers larger area of operation. It introduces operation flexibly where area of operation could be expanded easily since transceivers are mobile and could possibly tracking multiple underwater vehicles at the same time. Required minimum supervision because the transceivers (swarm ASV) are autonomous and the instilled swarm characteristics allow the ASV to make appropriate decision such as move relative to the underwater vehicle position without the external intervention. The proposed method is expected to give relatively accurate positioning as conventional method even though it is limited by the capability of the devices or components used in the process.

However, this system requires a precise and accurate time measurement devices for accurate position estimation. Inaccurate time measurement will result in positioning error and relatively inaccurate tracking. This system also need a robust ASV system where it possibly maintains its position with minimum position error while undergo external disturbances such as wave, current and wheatear changes. This issue mostly related to the robust controller design and appropriate ASV structural design. In addition, this system requires a real time process which sometimes will cause delay in the process if the processor is slow for processing the signal. It also depends on the frequency of the data processing. However, for proof of concepts, acceptable low frequency data update is possible. The received signal will consist of coarse noise and other unwanted signal. To obtain accurate results extensive signal processing should be performed which sometimes will be challenging process especially when real time processing involves.

2.3 AUV Cooperative Navigation System

Each of the AUVs will carry its own inertial navigation sensor and GPS. Before submerge into the water, all the three AUVs will record their initial position using GPS at the surface of the water. After submerge into the water, each of them will continuously run its inertial navigation system to estimate its position.

As discuss before, the lead AUV will obtain a high accuracy position from ASVs. The lead AUV (master) will synchronize with other two AUVs in order to help them achieve a higher accuracy of positioning system. The lead AUV will send its coordinate to other AUVs periodically by using acoustic modem. By calculating

propagation delay of the acoustic signal send by lead AUV, the other two AUVs are able to calculate their distance from the lead AUV as labeled by D_1 and D_2 in Fig. 5. This range information will be used to correct the position estimated by the inertial navigation system.

The three AUV will follow their predefined path to the docking station as set by the ASV based on the location of the docking station. When the docking station is in sight of the camera, the vision system will be activated to guild the AUV go inside the docking station. The detail of the docking process in discussed in the next section.

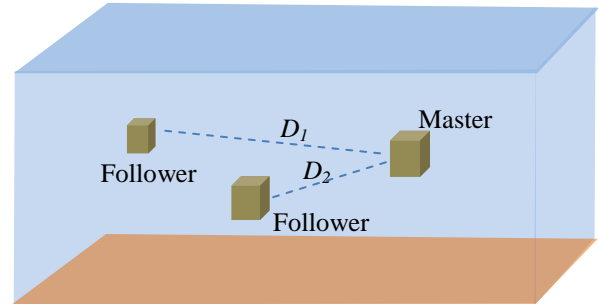


Fig. 5. Master-follower of the AUV

2.4 Underwater Docking System

The docking process consists of four stages and each of them is described in the following subsections.

A. Stage 1: Power Status Monitoring System

A master AUV is programmed to monitor the power level of each and every AUV under its command periodically. In this paper, the power level and conditioning rule for docking of AUVs can be broken down into three rules. In the first rule, an AUV which has more than 20% of its total power does not need to be recharge. Then, in the second rule, if the master AUV detected a slave AUV which has power percentage in between 10% to 20%, the slave AUV is considered to be low on power and subjected to either needs or does not need to be recharge. Finally, in the third rule, an AUV which has less than 10% of its total power is in urgent need to be recharge right away. Figure 6 shows a master AUV M currently monitoring the power level of each slave AUV denoted by S1, S2, and S3.

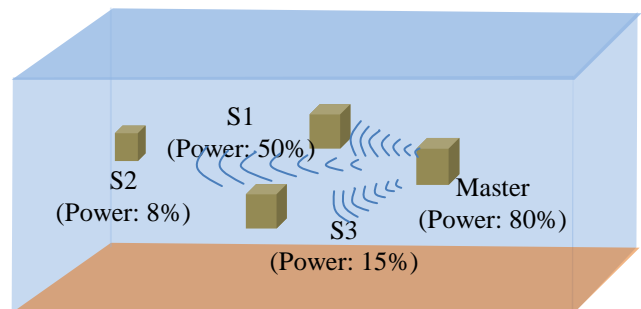


Fig. 6. Master AUV monitors slave AUVs' powers.

B. Stage 2: Global Docking Procedure

Once the master AUV notices a slave AUV in dire needs for recharging, it will guide the slave AUV along with all second level powered AUVs towards an underwater docking station. The underwater docking station location information is provided and transmitted by surface vessels and further received by master AUV. Once the master AUV received the information, the guidance system will be like master AUV leads and slave AUVs will follow. In the meantime, other first level slave AUVs were left to continue to perform their tasks. Figure 7 shows a master AUV M leading slave AUVs S2 and S3 towards an underwater docking station, UDS using the information provided by the surface vessels.

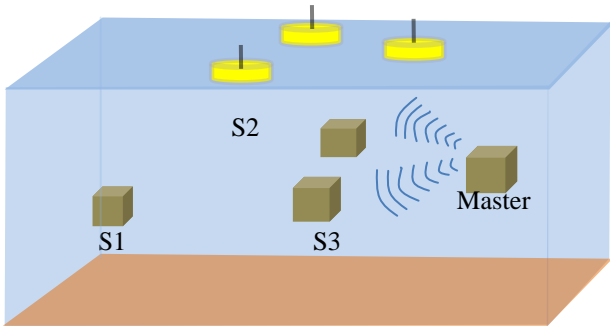


Fig. 7. Master AUV leading slave AUVs heading towards underwater docking station.

C. Stage 3: Local Docking Procedure

Once all of the AUVs had arrived at the underwater docking station site, they will dock systematically inside the station and subsequently recharges their batteries. This docking procedure is done optically using a camera mounted on each AUV.

The underwater docking station can only accommodate one AUV at any given time. Therefore, least powered AUV is given topmost priority to dock inside the station and recharges its battery first. While waiting for the AUV to be fully recharged, the other AUVs will dock and wait inside a multi-level waiting platform. And while waiting in the platform, the AUVs will turn off all of its actuators as well as their sensors except their modem in order to conserve as much power as it can. The modem is turned on for communication purposes and awaiting their turn for recharging.

Once the least powered AUV is fully recharged, it will undock from the docking station and docks into the waiting platform. Consequently, another low powered AUV will undock from the waiting platform and starts docking into the station to power up its battery. This sequence will keep going on until all of the AUVs are fully recharged. Figure 8(a) illustrates by using vision, Master AUV M and slave AUV S3 dock inside multi-story waiting platform while slave AUV S2 docks inside the docking station. Figure 8(b) shows master AUV M and slave AUV S3 waiting for slave AUV S2 to be fully recharge.

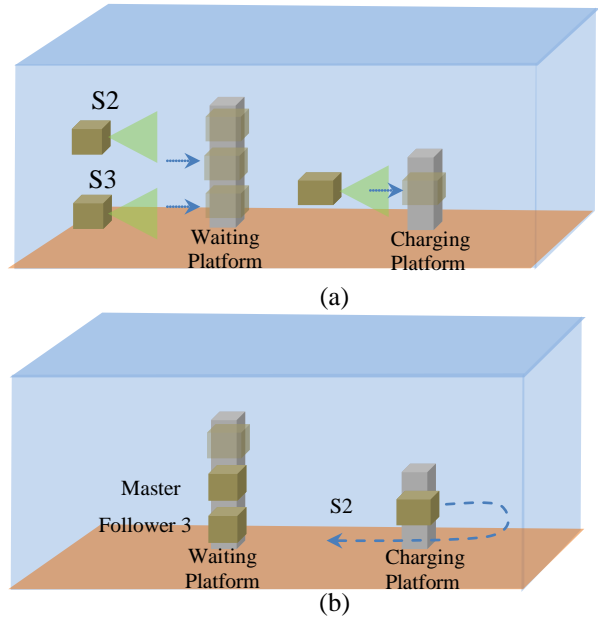


Fig. 8. Local docking procedure: (a) docking using vision, (b) two AUVs waiting for an AUV to be fully recharged.

D. Stage 4: Undocking Procedure and Mission Continuation

After all of the AUVs are fully recharged, the master AUV will instruct the entire slave AUVs to undock from the waiting platform. Next, the master AUV will guide the slave AUVs towards their last known mission location. Once they have arrived at the respective location, the master AUV will order slave AUVs to continue where they left from their previous missions. Figure 9(a) demonstrates AUVs undocked from waiting platform while Fig. 9(b) shows Master AUV M leading two fully charged slaves AUVs S2 and S3 back to their previous mission location.

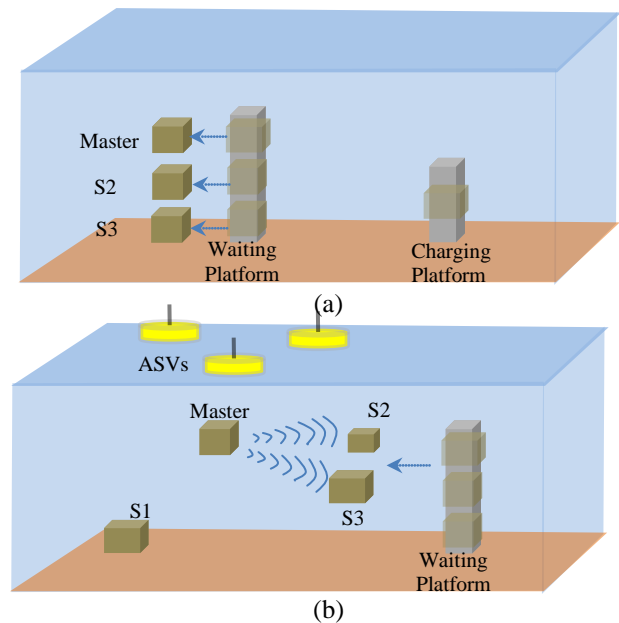


Fig. 9. Undocking procedure (a) undocked from waiting platform (b) move toward mission site

3. Conclusion

In this paper, a system framework for cooperative positioning of multiple AUV has been presented which includes cooperative localization using swarming robot, cooperative navigation system and underwater docking system. It is expected that the proposed method of localization is produced more reliable and flexible underwater operation especially for docking operation. In the future, realizing this works required an extensive research work and multi-disciplines engineering and thus, a modular design for each system could be considered for easy development and maintenance.

Acknowledgement

Thank for all members of Underwater, Control, and Robotic Group (UCRG), Universiti Sains Malaysia for supportive idea and contribution for this project proposal. This research work is supported by: Prototype Research Grant Scheme (PRGS-6740003)

References

- [1] F. V. F. Lima, and C. M. Furukawa, "Development and testing of an acoustic positioning system-description and signal processing," in IEEE Electronics Symposium, pp. 849-852, 2002.
- [2] M. E. B. Cerda, and A. R. Serrano, "A 3-D localization algorithm for robot swarm under the presence of failures," in Fifth International Conference on Automatic Autonomous Systems, pp. 226-232, 2009.
- [3] M. A. Ma'sum, G. Jati, K. Arrofi, A. Wibawo, P. Mursanto, and W. Jatmiko, "Autonomous quadcopter swarm robots for object localization and tracking"
- [4] D. P. Stormont, and A. Kutiyawala, "Localization using triangulation in swarms of autonomous rescue robots," in Proceeding of the IEEE International Workshop on Safety, Security and Rescue Robotics, 2007.
- [5] Z. Yunlong, X. Songdong, Z. Jianchoa, and D. Jing, "Target position estimation aided swarm robotic search under conditions of relative localization mechanism," in International Conference on Computing, Measurement, Control and Sensor Network, pp. 183-187, 2012.
- [6] R. V. Kulkarni, and G. K. Venayagamoorthy, "Bio-inspired algorithms for autonomous deployment and localization of sensor nodes," IEEE Transactions on Systems, Man, and Cybernetics, Vol. 40, No. 6, pp. 663-626, 2010.
- [7] J. A. Sauter, R. Matthews, H. V. D. Parunak, and S. A. Brueckner, "Performance of digital pheromones for swarming vehicle control," in AAMAS, pp. 903-910, 2005.
- [8] J. A. Rothermich, M. I. Ecemis, and P. Gaudiano, "Distributed localization and mapping with a robotic swarm," in LNCS, pp. 58-69, 2005.
- [9] F. Arvin, S. Doraisamy, K. Samsudin, and A. R. Ramli, "Self-localization of swarm robots based on voice signal acquisition," in International Conference on Computer and Communication Engineering, 2010.
- [10] J. Curcio, J. Leonard, J. Vaganay, A. Patrikalakis, A. Bahr, D. Battle, H. Schmidt, and M. Grund, "Experiments in moving baseline navigation using autonomous surface craft," in Proc. MTS/IEEE OCEANS Conf., pp. 730-735, 2005.
- [11] J. Vaganay, J. Leonard, J. Curcio, and J. Willcox, "Experimental validation of the moving long baseline navigation concept," in Proc. IEEE/OES Autonom. Underwater Veh. Conf., pp. 59-65, 2004.
- [12] A. Bahr and J. J. Leonard, "Cooperative localization for autonomous underwater vehicles," in Proc. Int. Symp. Exp. Robot., pp. 1-10, 2006.
- [13] Gao Rui and Mandar Chitre, Cooperative positioning using range-only measurements between two AUVs.
- [14] Alexander Bahr, (February 2009), "Cooperative Localization for Autonomous Underwater Vehicles", Doctoral Dissertation, Massachusetts Institute of Technology.
- [15] Scoot Willcox, Dani Golberg, Jerome Vaganary, and Joseph A. Curcio. Multi-vehicle Cooperative Navigation and Autonomy with the Bluefin CADRE System.
- [16] Maurice F. Fallon, Georgios Papadopoulos and John J. Leonard, Cooperative AUV Navigation using a Single Surface Craft, Massachusetts Institute of Technology, 77 Massachusetts Avenue, Cambridge.
- [17] M. Purcell, N. Forrester, T. Austin, R. Goldsborough, B. Allen, and C. von Alt, "A docking system for REMUS, an autonomous underwater vehicle," *OCEANS, IEEE Conference Proceedings*, Vol. 2, pp. 1132-1136, 1997.
- [18] Hydroid, a Kongsberg Company, "Underwater mobile docking of autonomous underwater vehicles," *OCEANS*, pp. 1-15, 2012.
- [19] B. Allen, T. Austin, N. Forrester, R. Goldsborough, A. Kukulya, G. Packard, M. Purcell, and R. Stokey, "Autonomous Docking Demonstrations with Enhanced REMUS Technology," *OCEANS*, pp. 1-6, 2006.
- [20] B. W. Hobson, R. S. McEwen, J. Erickson, T. Hoover, L. McBride, F. Shane, and J. G. Bellingham, "The Development and Ocean Testing of an AUV Docking Station for a 21" AUV," *OCEANS*, pp. 1-6, 2007.
- [21] T. Maki, R. Shiroku, Y. Sato, T. Matsuda, T. Sakamaki, and T. Ura, "Docking method for hovering type AUVs by acoustic and visual positioning," IEEE International Underwater Technology Symposium, pp. 1-6, 2013.

Classification of Ammonia Odor-profile Using k-NN Technique

Fathimah Abdul Halim¹, Muhammad Sharfi Najib², Kamarul Hawari Ghazali³, Muhamad Faruqi Zahari⁴, Abd. Aziz Mohd Azoddein⁵

^{1,2,3,4} Faculty of Electrical & Electronic Engineering, Universiti Malaysia Pahang, 26 600, Pahang, Malaysia
(E-mail: fathimah.halim@yahoo.com¹, sharfi@ump.edu.my², kamarul@ump.edu.my³, mei13002@stdmail.ump.edu.my⁴)

⁵ Faculty of Chemical and Natural Resources, University Malaysia Pahang, Gambang, 26300, Pahang, Malaysia
(E-mail: aaziz@ump.edu.my⁵)

Abstract - This paper presents the application of k-NN in classifying the low and high concentration of ammonia. High concentration of ammonia in water causes serious problematic to water environment and living things in water. Instruments that can directly detect ammonia concentration without any chemical treatment added is limited. Thus, this paper presents detection of ammonia using E-nose and the classification of ammonia in water using k- nearest neighbor (k-NN).

Keywords - Ammonia, Classification, k-NN, E-Nose.

1. Introduction

Ammonia (NH₃) is a combination of one hydrogen and three nitrogen atoms that have characteristics such as dissolve easily in water, colorless, and have a unique pungent odor one. Ammonia in water gives more serious harm because it is very toxic to aquatic organism. Additionally, the concentration of ammonia in water can increase due to agricultural excess and decomposition of biological waste [1]. The high concentration of ammonia resulting increases ammonia toxicity, especially for fishes and mammals [2]. Its toxicity effects on the brains of vertebrates, lead to convulsion and death [3, 4]. Nevertheless, monitoring and controlling the ammonia level in the water is very crucial for the water environment, fish and farming industry. The conventional ammonia detection methods that have been used to determine ammonia are Kjeldahl method [5, 6], Nessler's reagent calorimetric method [7], and the most common method are spectrometers and spectrophotometers [8]. However, these types of detection methods have limitations in labor intensive, expensive, complex operation and not suitable for outdoor use. On the other hand, the samples used for these instruments require samples to be added and treated with toxic chemical reagent. The availability of instrument that can straight away detect the presence of ammonia in water is currently limited.

However, beside of these methods, Electronic Nose (E-nose) is one of an electronic-based instrument that is used to detect the ammonia based on the unique profile of an ammonia odor [9]. An E- nose is the intelligent instrument that classifies the chemical odors mimicking a human. It consists of gas sensor array and various pattern recognition algorithms which are the sensor are used to

produce a unique profile of an odor. This odor will be analyzed using pattern classification methods [10, 11]. The sensor functioning as sniffs the vapor from a sample and provides a set of measurements. Gas sensors tend to have very wide-ranging selectivity, it will respond to many different samples provided. The detection of odors and gases has been applied to many industrial applications such as medical [12], environmental [13], and food product [14, 15] and one of the most important applications is the detection of hazardous gases [16]. The sensor used to ultimately be very portable and small for convenient, diverse operations and with analysis and detecting capabilities [17]. Electronic nose is inexpensive, fast, simple and convenient method to detect ammonia in water. There are several pattern recognition systems that are used for classification such as Principal Component Analysis (PCA) [18], Support Vector Machine (SVM) [19], Discriminant Factor Analysis [20], and Artificial Neural Network [21] and also KNN. In this study, K-nearest neighbor method is used to compare the concentration level of ammonia samples. Previously researchers' results, k-NN couple with e-nose produced accuracy percentage above 95% [19], [22].K-nearest neighbor (KNN) characteristics are simple but robust classifier and qualified to produce high performance outcomes even for complex applications [23-35].

This study presents implementing k-NN classification technique using sensor reading from the E - nose for Ammonia classification. The E - nose is used to produce a unique profile of ammonia in water. Using these features and profile of ammonia in k-NN classifying will produce the percentage accuracy performance. This accuracy is indicating the reliability of k-NN in the pattern recognition of ammonia.

2. Methodology

2.1 Ammonia Sampling and Preparation

There are two categories of ammonia solution, high concentration (25 ppm) and low concentration (5 ppm) respectively. The concentration range can be referred in Department of Environment (D.O.E) standard [26].The fresh sample of ammonia was diluted into standard specific concentration and was kept as a stock solution. From the stock solution, the sample then was diluted into specific concentration by using molarity formula. The

ammonia sample will be prepared into five different dilutions. The samples were filled into 5 closed vials for each different diluted solution. The solution will be diluted until each vial contains 10ml of solution. Each sample of five different concentrations has ten repeated reading data taken by the E - nose. Before the concentration samples was insert in E-nose, the samples concentration were validated using chemical laboratory standard method known as spectrometer to make sure the diluted ammonia concentration follow the standard range stated by DOE. The confirmed concentration of high and low ppm then were proceed using E-nose detection. Then there are supposed to have 50 sample data ready. The E-nose consists of 4 array sensors that will detect the odors of ammonia concentration at the same time. Ultimately, the E-nose reading will has a dimension of 4 x 10 for each sample. Each sample will consist of 40 E-nose reading. With five different concentrations, sensor inside E-nose was activated and senses the odors of ammonia concentration and was produced in total of 2000 raw data samples reading.

2.2 Data analysis

After completing the raw data samples, the preprocessing technique was applied. Before beginning with k-NN training and testing data, all the sample data sets were normalized per sample region, to obtain the features and odor-profiles graph. The features also were analyzed by using box plot to visualize and summarize the data. The mean of normalized data sample also were obtained. These mean of normalized data set then were divided into k-NN training and testing data. K-NN operational principle is to classify whole data into training and sample data point. By implementing a k-NN algorithm for classification odor profiles of ammonia are effective because KNN are suitable for large training data and capable to produce high performance result even for complex operation.

3. Results

The raw data has been normalized and pre-processed in order to obtain unique profile odor of ammonia with different concentration. Five different concentration of ammonia were divided into group of high and low concentration. All the sample data sets were normalized per sample region.

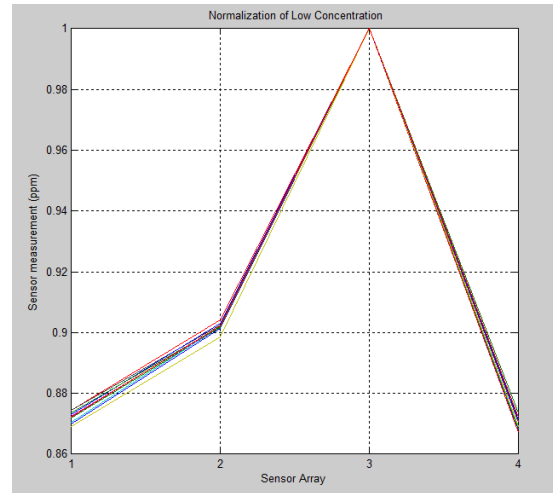


Fig. 1. A sample of Normalized data for low concentration of ammonia.

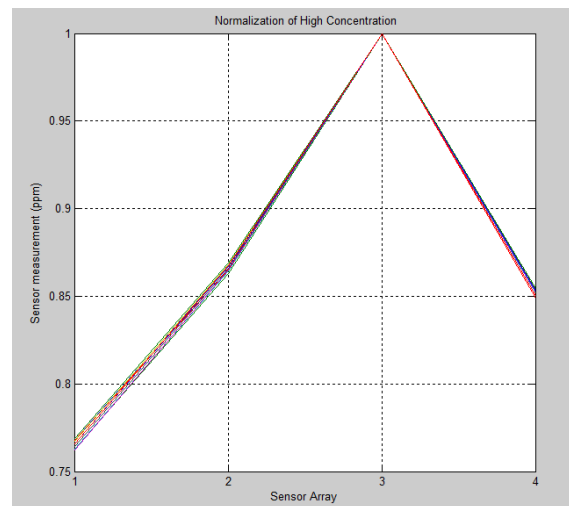


Fig. 2. A sample of Normalized data for High concentration of ammonia.

Fig. 1 and Fig. 2 show a sample measurement of normalized data for High and low concentration of ammonia. Based on the figures above, both graphs show the data collected from the sensor 1, 2 and 4 have noticeable differences in patterns and values. These graphs shows low and high concentration of ammonia has dissimilar features and profile. After normalization technique was applied, these features were improved by using boxplot. Boxplot is used to summarize and visualize the set data in a graph.

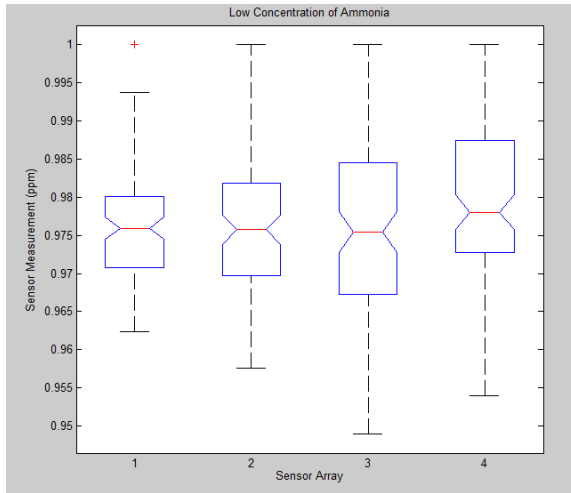


Fig.3. Box plot for low concentration of ammonia

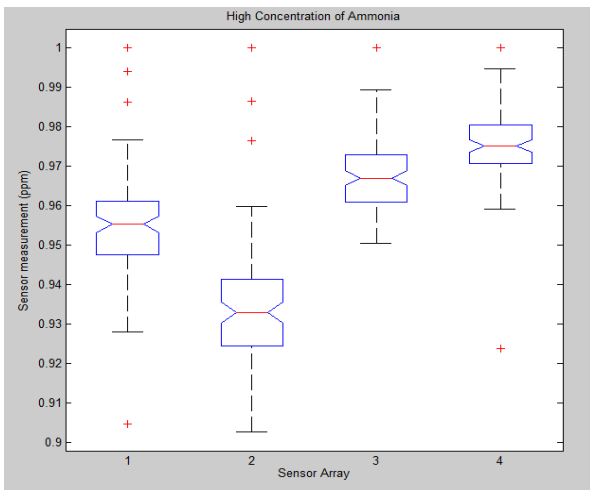


Fig.4. Box plot for high concentration of ammonia

Box plot consists of median, the approximate quartiles, and the lowest and highest data point. Based on the figures 3 and 4, the median for each dataset is indicated by the red center line, the lower and upper quartiles are the edges of the blue line, which is known as the inter-quartile range (IQR). The maximum and minimum values are indicated by the end of the black line and known as a whisker. In figure 4, the four boxplots have nearly identical median values. Figure 3 shows the notches in the boxplot are not overlapped, it is concluded that the median of the four sensors is significantly different. It is because notches display the variability of the median between sensors. The sample data sets, then were proceeding to the mean of normalized data pattern.

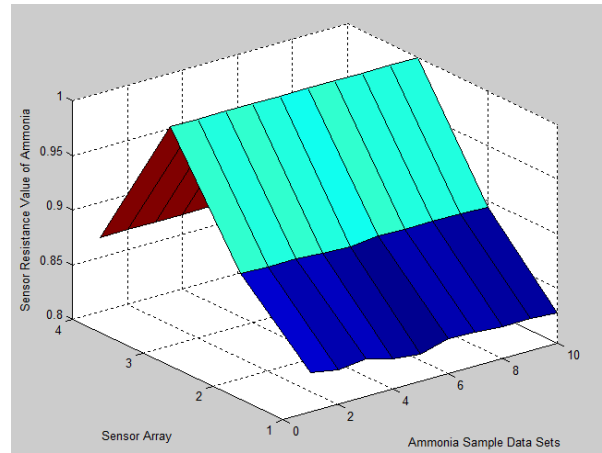


Fig.5. Mean of Normalized Data Samples from Low Ammonia Concentration

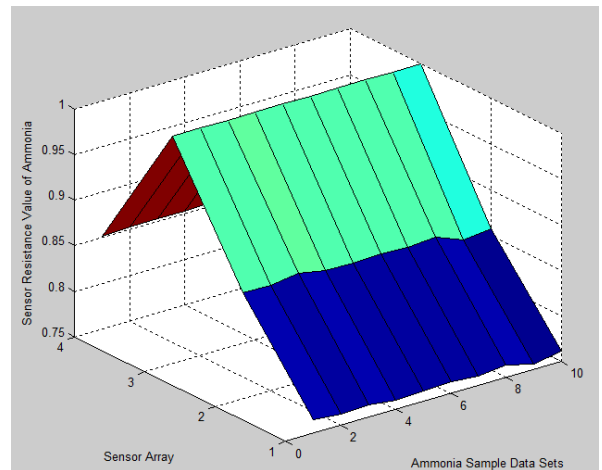


Fig.6. Mean of Normalized Data Samples from High Ammonia Concentration

Figures 5 and 6 are three dimensional parametric surfaces graph of mean by x, y and z axes. X-axis is ammonia sample data set, y-axis is sensor array, and z-axis is sensor resistance value from the E-nose. These 3-D graph pattern shows the different pattern of mean respectively. From the pattern of boxplot, normalization and mean of normalized data sets, there are significant different in features and graph pattern of high and low level concentration. The significant sensors data were selected as an input data for training. These mean of normalized data sets were divided into two groups for training and testing. The classifier success rate for the sample data test is 97%. The data were classified by using different values of k which are 1, 3 and 5 nearest neighbor the different distance didn't change the classifier rate.

ErrorRate: 0
LastCorrectRate: 1
LastErrorRate: 0
InconclusiveRate: 0.0300
ClassifiedRate: 0.9700
Sensitivity: 1
Specificity: 0.9697
PositivePredictiveValue: 0.2500
NegativePredictiveValue: 1
PositiveLikelihood: 33
NegativeLikelihood: 0

Fig.7. Classifier Performance of Ammonia Concentration.

Figure 7 shows the classifier performance of ammonia concentration for the whole data sets. Character correctly classified samples without counting Inconclusive result. InconclusiveRate is non classified samples. CorrectRate will counted inconclusiveRate sample are correct, which its lead the accuracy performance of ammonia is 100%. The performance measures using specificity and sensitivity are 97% and 100% respectively.

3. Conclusion

This paper presents the reliability of k-NN classification technique in classify the features and odor profiles of ammonia. The analysis and result show the differences between high and low concentration of ammonia in term of odor profile graph pattern. These odor profile result then have been analyzed by using intelligent classification technique KNN which is successfully approaches 100%.

Acknowledgement

The authors would like thank the financial support from the excellent fund UMP Research Grant coded RDU13037 and all staff and student involved from Faculty of Electrical and Electronics Engineering and Faculty of Chemical and Natural Resources.

References

[1] D. J. Randall and T. K. N. Tsui, "Ammonia toxicity in fish." *Mar. Pollut. Bull.*, vol. 45, pp. 17–23, 2002.

[2] J. Sashaw, M. Nawata, S. Thompson, C. M. Wood, and P. a Wright, "Rhesus glycoprotein and urea transporter genes in rainbow trout embryos are upregulated in response to alkaline water (pH 9.7) but not elevated water ammonia.," *Aquat. Toxicol.*, vol. 96, no. 4, pp. 308–13, Mar. 2010.

[3] N. L. J. Wee, Y. Y. M. Tng, H. T. Cheng, S. M. L. Lee, S. F. Chew, and Y. K. Ip, "Ammonia toxicity and tolerance in the brain of the African sharptooth catfish,

Clarias gariepinus.," *Aquat. Toxicol.*, vol. 82, no. 3, pp. 204–13, May 2007.

[4] M. M. Hegazi and S. S. Hasanein, "Effects of chronic exposure to ammonia concentrations on brain monoamines and ATPases of Nile tilapia (*Oreochromis niloticus*).," *Comp. Biochem. Physiol. C. Toxicol. Pharmacol.*, vol. 151, no. 4, pp. 420–5, May 2010.

[5] P. Campins-Falco, S. Meseguer-Lloret, T. Climent-Santamaria, and C. Molins-Legua, "A microscale Kjeldahl nitrogen determination for environmental waters." *Talanta*, vol. 75, no. 4, pp. 1123–6, May 2008.

[6] S. M. Lloret, J. V. Andrés, C. M. Legua, and P. C. Falcó, "Determination of ammonia and primary amine compounds and Kjeldahl nitrogen in water samples with a modified Roth's fluorimetric method.," *Talanta*, vol. 65, no. 4, pp. 869–75, Feb. 2005.

[7] H. Jeong, J. Park, and H. Kim, "Determination of NH₄⁺ in Environmental Water with Interfering Substances Using the Modified Nessler Method," vol. 2013, 2013.

[8] A. Baker, D. Ward, S. H. Lieten, R. Periera, E. C. Simpson, and M. Slater, "Measurement of protein-like fluorescence in river and waste water using a handheld spectrophotometer," *Water Res.*, vol. 38, pp. 2934–2938, 2004.

[9] X. F. X. Fang, X. G. X. Guo, H. S. H. Shi, and Q. C. Q. Cai, "Determination of Ammonia Nitrogen in Wastewater Using Electronic Nose," *Bioinforma. Biomed. Eng. iCBBE 2010 4th Int. Conf.*, 2010.

[10] F. Tian, S. X. Yang, and K. Dong, "Circuit and Noise Analysis of Odorant Gas Sensors in an E-Nose," no. December 2004, pp. 85–96, 2005.

[11] L. Zhang and F. C. Tian, "A new kernel discriminant analysis framework for electronic nose recognition," *Anal. Chim. Acta*, vol. 816, pp. 8–17, 2014.

[12] A. D'Amico, G. Pennazza, M. Santonico, E. Martinelli, C. Roscioni, G. Galluccio, R. Paolesse, and C. Di Natale, "An investigation on electronic nose diagnosis of lung cancer.," *Lung Cancer*, vol. 68, pp. 170–176, 2010.

[13] B. Rajbansi, U. Sarkar, and S. E. Hobbs, "Hazardous odor markers from sewage wastewater: A step towards simultaneous assessment, dearomatization and removal," *Journal of the Taiwan Institute of Chemical Engineers*, 2013.

[14] M. L. Rodriguez-Mendez, C. Apetrei, M. Gay, C. Medina-Plaza, J. A. De Saja, S. Vidal, O. Aagaard, M. Ugliano, J. Wirth, and V. Cheynier, "Evaluation of oxygen exposure levels and polyphenolic content of red wines using an electronic panel formed by an electronic nose and an electronic tongue," *Food Chem.*, vol. 155, pp. 91–97, 2014.

[15] X. Hong and J. Wang, "Detection of adulteration in cherry tomato juices based on electronic nose and tongue: Comparison of different data fusion approaches," *J. Food Eng.*, vol. 126, pp. 89–97, 2014.

[16] P. E. Keller, "Electronic noses and their applications," *IEEE Tech. Appl. Conf. Work. Northcon95 Conf. Rec.*, 1995.

- [17] Z. T. Z. Tao, W. L. W. Lei, and J. T. J. Teng, "Pattern Recognition of the Universal Electronic Nose," 2008 Second Int. Symp. Intell. Inf. Technol. Appl., vol. 3, pp. 249–253, 2008.
- [18] B. Tudu, A. Metla, B. Das, N. Bhattacharyya, A. Jana, D. Ghosh, and R. Bandyopadhyay, "Towards versatile electronic nose pattern classifier for black tea quality evaluation: An incremental fuzzy approach," IEEE Trans. Instrum. Meas., vol. 58, pp. 3069–3078, 2009.
- [19] K.-T. Tang, S.-W. Chiu, C.-H. Pan, H.-Y. Hsieh, Y.-S. Liang, and S.-C. Liu, "Development of a Portable Electronic Nose System for the Detection and Classification of Fruity Odors," Sensors (Peterborough), vol. 10, pp. 9179–9193, 2010.
- [20] M. Zhang, X. Wang, Y. Liu, X. Xu, and G. Zhou, "Species Discrimination among Three Kinds of Puffer Fish Using an Electronic Nose Combined with Olfactory Sensory Evaluation," Sensors, vol. 12, pp. 12562–12571, 2012.
- [21] M. S. Najib, N. A. M. Ali, M. N. M. Arip, A. M. Jalil, and M. N. Taib, "Classification of Agarwood region using ANN," 2010 IEEE Control Syst. Grad. Res. Colloq. (ICSGRC 2010), pp. 7–13, Jun. 2010.
- [22] S. Guney and A. Atasoy, "Classification of n-butanol concentrations with k-NN algorithm and ANN in electronic nose," Innov. Intell. Syst. ..., pp. 138–142, 2011.
- [23] N. Bhatia and C. Author, "Survey of Nearest Neighbor Techniques," vol. 8, no. 2, pp. 302–305, 2010.
- [24] I. Saini, D. Singh, and A. Khosla, "QRS detection using K-Nearest Neighbor algorithm (KNN) and evaluation on standard ECG databases," J. Adv. Res., vol. 4, no. 4, pp. 331–344, Jul. 2013.
- [25] M. Mustafa, M. N. Taib, Z. H. Murat, and N. Sulaiman, "Comparison between KNN and ANN Classification in Brain Balancing Application via Spectrogram Image," vol. 2, no. 4, pp. 17–22, 2012.
- [26] "Department of Environment | Ministry of Natural Resources & Environment." [Online]. Available: <http://www.doe.gov.my/portalv1/en/>. [Accessed: 14-Nov-2014].

Classification of Ammonia in water for Oil and Gas Industry using Case Based Reasoning (CBR)

Muhamad Faruqi Zahari¹, Muhammad Sharfi Najib², Kamarul Hawari Ghazali³, Fathimah Abdul Halim⁴, Abd. Aziz Mohd Azoddein⁵,

^{1, 2, 3, 4} Faculty of Electrical and Electronic Engineering, University Malaysia Pahang, Pekan, 26600, Pahang, Malaysia
(E-mail: mei13002@stdmail.ump.edu.my¹, sharfi@ump.edu.my², kamarul@ump.edu.my³, fathimah.halim@yahoo.com⁴)

⁵Faculty of Chemical and Natural Resources, University Malaysia Pahang, Gambang, 26300, Pahang, Malaysia
(E-mail: aaziz@ump.edu.my⁵)

Abstract – Toxic gasses are exists in environment such as benzene, ammonia and others. Ammonia highly dissolves in water which is sources of human and other species. If the ammonia have high concentration, the effect of human health will be dangerous. Then, using proper monitoring and wastewater management the hazard can be prevented. This paper proposed the intelligence classification technique using an Electronic Nose (E-nose) measurement. The sensor array in the E - nose are used for the inputs of the Case Based Reasoning (CBR) for intelligent classification. The experimental result shows that the technique accomplished to classify with high accuracy which is 100% of accuracy.

Keywords – CBR, e-nose, ammonia, classification, water.

1. Introduction

Nowadays, there are common toxic gasses exists in an environment such as benzene, ammonia, and others [1]. There are several industries that contribute to this toxic gasses in an environment such as medical , food packaging, agriculture, oil and gas and others [2]–[4]. The industries have own regulations to protect human or earth from hazards such as wastewater regulations, hazard managements and others [5]–[8]. Furthermore, water environmental issues have continued since long years ago, which source of the clean water being contaminated due to poor management and monitoring by various unpermitted activities [9]–[12].

One of the famous chemicals in water is Ammonia which caused lung edema, failure of the nervous system, acidosis and kidney damage [13], [14]. In addition, ammonia have highly dissolve in water, which have colorless fluid and pungent smell . Thus, monitoring and management of wastewater that consist of toxic substance are compulsory to prevent environmental pollution [10], [17].

There are several methods for monitoring such as thermal image processing, Light Detection and Ranging (LIDAR), Electronic Nose (e-nose) and others [18]. E-nose using a concept sensor array for odor classification device [13]. The widely used sensor for chemical detection was metal-oxide gas sensors which used for varied application [19]. Metal-oxide sensor have advantages of

low cost, short time response and high sensitivity [20], [21].

The E - nose was a device that functions as human olfactory system which detect the odor and the human brain will classify the odor based on the knowledge [22]. Thus, e-nose will take over the human nose to detect toxic gasses and using intelligence classification in order to define the odor of toxic gasses [23].

The e-nose detection data will analyze using normalization techniques which enables the comparison between ammonia concentration [24], [25]. In addition, the normalization technique was corrected systematic error which often present and can be removed by normalization method [26], [27]. Furthermore, normalization has several methods such as Range scale, relative scale, baseline subtraction, global method and local method [28], [29]. While, the data analyze using range scale which is [0, 1] as a fixed range for all samples [30], [31].

The simple boxplot displays the several categories of a discrete variable by separating the continuous variable of five statistic which is minimum, first quartile, median value, third quartile and maximum value [32]. The boxplot can differentiate the features of each sensor for each sample by statistical features as mentioned[33], [34].

Regression one of the methods to determine the validity of data point through a set of data point, regression analysis can be used in combination with statistical techniques .

There are several classification methods such as an Artificial Neural Network (ANN), k-Nearest Neighbor (KNN), Case Based Reasoning (CBR) and others [38]. CBR was created as a four step process of human or computer reasoning which called CBR cycled [39]. CBR cycled contain of retrieve, reuse, revise and retain which the crucial step of CBR was the retrieval case in order to classify similar cases that stored in the library [38], [40].

2. Experimental Section

2.1 Ammonia Preparation

The Ammonia will be prepared based on Oil and Gas industry environment. Ammonia in water sample is used for experimental process using 28% - 30% of ammonia in ammonia hydroxide which is a laboratory specification. Then, the ammonia in water was diluted into specific concentration for 10ml for each sample cell. The concentration was diluted using dilution equation. Each sample of concentration has five repeated measures data using an e-nose.

The concentration validated using chemical method which called Total Nitrogen Test (TNT) to confirm the concentration of ammonia in water. Then, the confirmed concentration was inserted to sample cell and being moved to the e-nose detection for further process.

E- Nose were consist of array sensor that will measure the different odor of ammonia in water concentration. Data measured by e-nose for each sample has dimension of 4x5 which in total 20 measured data. Each sensor will measure the concentration in 1000 of data which in total 4000 raw data at one time. Then, raw measured data were applied preprocessing method which is to reduce the error between the measured data.

Furthermore, the raw measured data was normalized in range [0 to 1] for reduction of error and noise of the measured data. Then, it was used to obtain the profile graph for visualizing the different of concentration. In addition, boxplot technique used for summarizing normalized data into five statistical analysis, which is minimum, maximum, first quartile, median and third quartile.

Then, the mean of the normalized data was used as features in CBR technique. By implementing a CBR algorithm, the classification of ammonia in water concentration can be accomplish.

2.2 Data Collection

The data collection will be recorded as in Table 1. The sample of ammonia water will contain different percentages of ammonia.

Table 1: Data Measured

<i>Sensors</i>	<i>Sensor 1</i>	<i>Sensor 2</i>	<i>Sensor 3</i>	<i>Sensor 4</i>
<i>D₁</i>	<i>D₁₁</i>	<i>D₁₂</i>	<i>D₁₃</i>	<i>D₁₄</i>
<i>D₂</i>	<i>D₂₁</i>	<i>D₂₂</i>	<i>D₂₃</i>	<i>D₂₄</i>
<i>D₃</i>	<i>D₃₁</i>	<i>D₃₂</i>	<i>D₃₃</i>	<i>D₃₄</i>
<i>⋮</i>	<i>⋮</i>	<i>⋮</i>	<i>⋮</i>	<i>⋮</i>
<i>D_N</i>	<i>D_{N1}</i>	<i>D_{N2}</i>	<i>D_{N3}</i>	<i>D_{N4}</i>

3. Result and Discussion

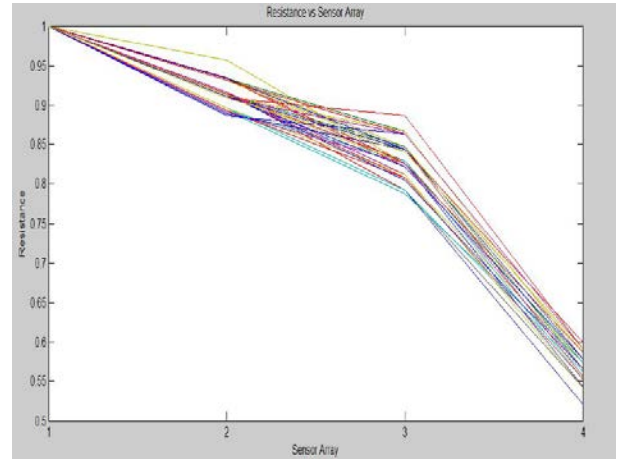


Fig. 1: Low ppm of ammonia pattern

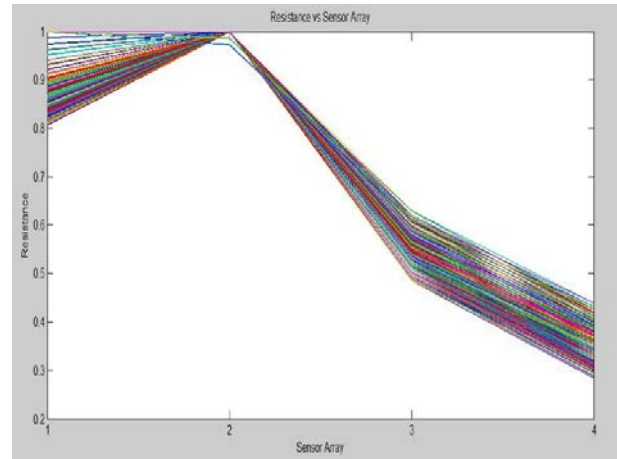


Fig. 2: High ppm of ammonia pattern

The raw data have been normalized to obtain a unique profile of odor concentration of ammonia in water as shown in Figure 1 and Figure 2 for high and low concentration of ammonia. The graph shows that there are differences between two classes based on pattern and values.

Based on pattern recognition, low ppm of ammonia have a different pattern compared to high ppm of ammonia as shown in Fig. 1 and Fig. 2. The graph features were improved by statistical analysis using boxplot as shown in Fig. 3 and Fig. 4.

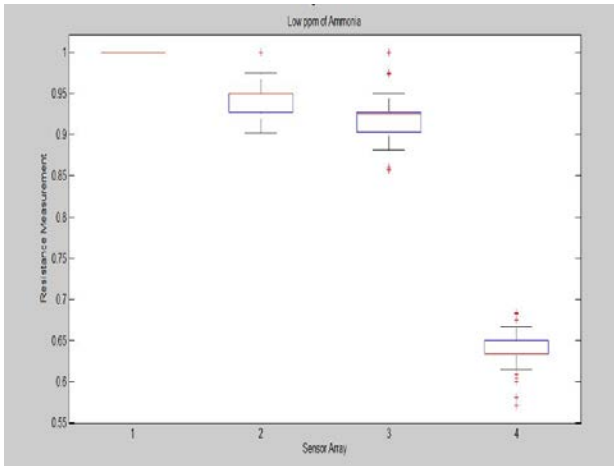


Fig. 3: Low ppm of ammonia boxplot

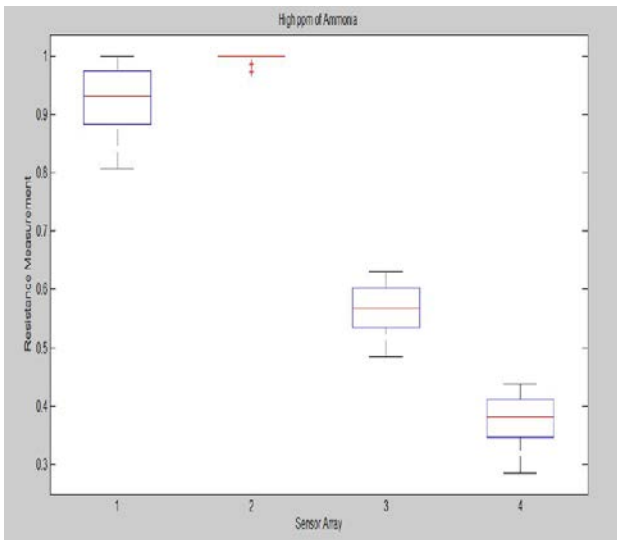


Fig. 4: High ppm of ammonia boxplot

Boxplot consists of minimum, maximum, first quartile, median and third quartile features point. Based on Figure 3 and Figure 4, the blue line of the boxplot indicates the first quartile and third quartile. The median was indicated as a red line in the boxplot graph. While, the minimum and maximum point was indicated as black line which known as a whisker.

Based on the Fig. 3 and Fig. 4, there are significantly different between the low ppm and higher ppm, which is the significant sensor for low ppm ammonia in water was the sensor number one while significant sensor for high ppm ammonia in water was sensor number 2.

To validate the data, regression was used to differentiate the high ppm and low ppm as shown in Fig. 5. The regression show of 100% of classification data between low and high ppm of ammonia.

Regression data and the CBR data was used same features in order to validate the classification. While the CBR has shown the 100% of accuracy percentage in classification of mean features between low and high ppm of ammonia.

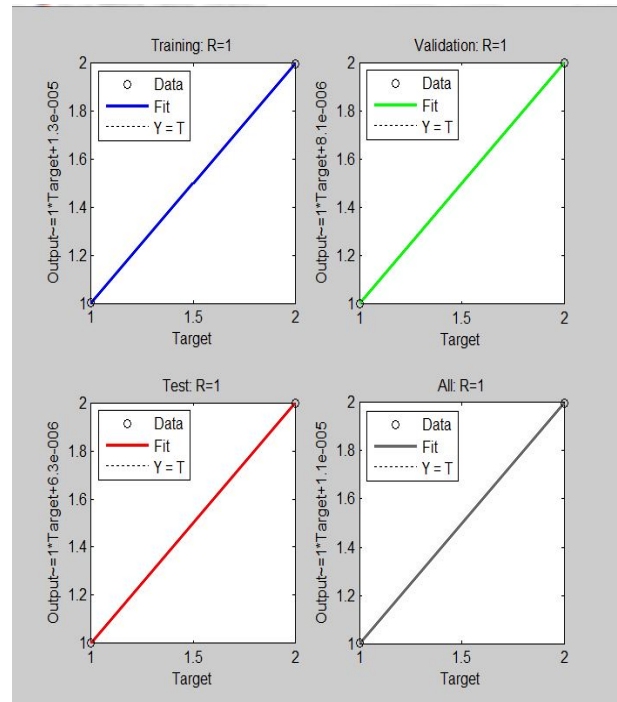


Fig. 5: Regression between Low and High ppm of ammonia

4. Conclusion

This paper presents the reliability of CBR technique in classification of ammonia in water concentration using mean features. The analysis of the profile, boxplot and ANN regression shows the different between two concentration classes. Then, using intelligent classification which is CBR the result was successful approach 100% of classification between two classes.

Acknowledgement

The authors would like to thank all staff and student involved, Faculty of Electrical and Electronics Engineering, Faculty of Chemical and Natural Resources, UMP and excellent fund from UMP Research Grant coded RDU130606.

References

- [1] V. Georgieva, L. Spassov, And V. Georgiev, "An Attempt For Nh, Detection Based On Quartz Resonator With Thin Soot Film," Pp. 1086–1088, 1999.
- [2] A. Yoshio, "Heavy Industry.Pdf," *The Formation Of Heavy Industry*. Pp. 450–470.
- [3] R. O. A. Rahman, H. A. Ibrahim, And Y.-T. Hung, "Liquid Radioactive Wastes Treatment: A Review," *Water*, Vol. 3. Pp. 551–565, 2011.
- [4] C. Klotz-Ingram And K. Day-Rubenstein, "The Changing Agricultural Research Environment: What Does It Mean For Public-Private

- Innovation?," *Agbioforum*, Vol. 2. Pp. 24–32, 1999.
- [5] P. Principal, D. Allison, And J. Witte, "Critical Issues In Healthcare Environments."
- [6] H. Roopadevi And R. K. Somashekar, "Assessment Of The Toxicity Of Waste Water From A Textile Industry To *Cyprinus Carpio*," *J. Environ. Biol.*, Vol. 33, Pp. 167–171, 2012.
- [7] G. Liu, Z. Yang, B. Chen, Y. Zhang, M. Su, And L. Zhang, "Emergy Evaluation Of The Urban Solid Waste Handling In Liaoning Province, China," *Energies*, Vol. 6, Pp. 5486–5506, 2013.
- [8] C. H. Drew, D. A. Grace, S. M. Silbernagel, E. S. Hemmings, A. Smith, W. C. Griffith, T. K. Takaro, And E. M. Faustman, "Nuclear Waste Transportation: Case Studies Of Identifying Stakeholder Risk Information Needs," *Environmental Health Perspectives*, Vol. 111. Pp. 263–272, 2003.
- [9] C. Wochnowski, S. Metev, And G. Sepold, "Uv–Laser-Assisted Modification Of The Optical Properties Of Polymethylmethacrylate," *Appl. Surf. Sci.*, Vol. 154–155, Pp. 706–711, 2000.
- [10] J. A. Awomeso, A. M. Taiwo, A. M. Gbadebo, And A. O. Arimoro, "Waste Disposal And Pollution Management In Urban Areas: A Workable Remedy For The Environment In Developing Countries," *Am. J. Environ. Sci.*, Vol. 6, Pp. 26–32, 2010.
- [11] N. P. Randall And K. L. James, "The Effectiveness Of Integrated Farm Management, Organic Farming And Agri-Environment Schemes For Conserving Biodiversity In Temperate Europe - A Systematic Map," *Environmental Evidence*, Vol. 1. P. 4, 2012.
- [12] S. Broadmeadow And T. R. Nisbet, "The Effects Of Riparian Forest Management On The Freshwater Environment: A Literature Review Of Best Management Practice," *Hydrology And Earth System Sciences*, Vol. 8. Pp. 286–305, 2004.
- [13] Q. Ameer And S. B. Adeloju, "Polypyrrole-Based Electronic Noses For Environmental And Industrial Analysis," *Sensors Actuators B Chem.*, Vol. 106, No. 2, Pp. 541–552, May 2005.
- [14] I. Trebs, F. X. Meixner, J. Slanina, R. Otjes, P. Jongejan, And M. O. Andreae, "Real-Time Measurements Of Ammonia, Acidic Trace Gases And Water-Soluble Inorganic Aerosol Species At A Rural Site In The Amazon Basin," *Atmospheric Chemistry And Physics Discussions*, Vol. 4. Pp. 1203–1246, 2004.
- [15] A. P. Seitsonen, A. M. Saitta, T. Wassmann, M. Lazzeri, And F. Mauri, "Ammonia," *Water*, Vol. 5, P. 1966, 2010.
- [16] "Ammonia In Drinking Water," Canada, 2013.
- [17] K. Jahn, "Ecologically Sound Disposal Methods In Ammonia Technology," No. 5, Pp. 3–6, 2009.
- [18] P. Murvay And I. Silea, "A Survey On Gas Leak Detection And Localization Techniques," 2005.
- [19] A. Vergara And E. Llobet, "Sensor Selection And Chemo-Sensory Optimization: Toward An Adaptable Chemo-Sensory System," *Frontiers In Neuroengineering*, Vol. 4. 2012.
- [20] J. R. Cordeiro, M. I. V. Martinez, R. W. C. Li, A. P. Cardoso, L. C. Nunes, F. J. Krug, T. R. L. C. Paixão, C. S. Nomura, And J. Gruber, "Identification Of Four Wood Species By An Electronic Nose And By Libs," *Int. J. Electrochem.*, Vol. 2012, Pp. 1–5, 2012.
- [21] K. Song, Q. Wang, Q. Liu, H. Zhang, And Y. Cheng, "A Wireless Electronic Nose System Using A Fe₂O₃ Gas Sensing Array And Least Squares Support Vector Regression," *Sensors*, Vol. 11. Pp. 485–505, 2011.
- [22] H. V. Ramamoorthy, S. N. Mohamed, And D. S. Devi, "E-Nose And E-Tongue: Applications And Advances In Sensor Technology," *Journal Of Nanoscience And Nanotechnology*, Vol. 2. Pp. 370–376, 2014.
- [23] D. Hodgins, "The Development Of An Electronic 'Nose' For Industrial And Environmental Applications," Vol. 27, Pp. 255–258, 1995.
- [24] G. Gomez, "Normalization Methods And Data Preprocessing," 2010.
- [25] F. S. Cabo, Z. Trajanoski, And K. Cho, "A Graphical Users Interface To Normalize Microarray Data," No. Dsc, 2003.
- [26] S. R. Taghizadeh, "Digital Signal Processing," No. January, Pp. 1–48, 2000.
- [27] D. Venet, "Matarray: A Matlab Toolbox For Microarray Data," *Bioinformatics*, Vol. 19, No. 5, Pp. 659–660, Mar. 2003.
- [28] B. Tudu, B. Kow, N. Bhattacharyya, And R. Bandyopadhyay, "Normalization Techniques For Gas Sensor Array As Applied To Classification For Black Tea," Vol. 2, No. 1, Pp. 176–189, 2009.
- [29] M. Astrand, "Normalization And Differential Gene Expression Analysis Of Microarray Data,"

Chalmers University Of Technology And Goteborg University, 2008.

- [30] J. C. Miecznikowski And K. F. Sellers, "Statistical Analysis Of Chemical Sensor Data," 2002.
- [31] J. Yosinski And R. Paffenroth, "Nonlinear Estimation For Arrays Of Chemical Sensors," 2000.
- [32] H. M. Rodriguez And A. J.O, "Simple Boxplot," In *Building Spss Graphs To Understand Data*, J. P. Donnelly, Ed. 2013, Pp. 200–209.
- [33] M. Pfannkuch, "Comparing Box Plot Distributions : 4 A Teacher ' S Reasoning," Vol. 5, No. 2, Pp. 27–45, 2006.
- [34] F. Marmolejo-Ramos And U. Valle, "The Shifting Boxplot . A Boxplot Based On Essential Summary Statistics Around The Mean .," Vol. 3, No. 1, Pp. 37–45, 2011.
- [35] L. Pace, "Correlation And Regression," In *Beginning R: An Introduction To Statistical Programming*, No. I, Apress, 2012, Pp. 215–242.
- [36] J. S. Simonoff, "Statistical Analysis Using Microsoft Excel Microsoft," Pp. 1–12, 2008.
- [37] K. Y. Wang And T. T. Chau, "An Association Between Air Pollution And Daily Outpatient Visits For Respiratory Disease In A Heavy Industry Area," *Plos One*, Vol. 8, 2013.
- [38] M. S. Najib, M. N. Taib, N. A. M. Ali, M. N. M. Arip, And A. M. Jalil, "Classification Of Agarwood Grades Using Ann," *Int. Conf. Electr. Control Comput. Eng. 2011*, Pp. 367–372, 2011.
- [39] M. S. Najib, M. U. Ahmad, P. Funk, M. N. Taib, U. T. Mara, A. Measurement, And A. Sample, "Agarwood Classification : A Case-Based Reasoning Approach Based On E-Nose," Pp. 120–126, 2012.
- [40] M. G. Voskoglou, "Fuzzy Sets In Case-Based Reasoning," *2009 Sixth Int. Conf. Fuzzy Syst. Knowl. Discov.*, Vol. 6, Pp. 345–373, 2009.

An Experimental Study Of Combinational Logic Circuit Minimization Using Firefly Algorithm

Aznilinda Zainodin², Aida Khairunnisaa Ab. Kadir¹, M. Nasir Ayob¹, Ahmad Fariz Hassan¹
Amar Faiz Zainal Abidin², Fazlinashatul Suhaidah Zahid², Hazriq Izzuan Jaafar³, Ismail Mohd Khairuddin⁴

¹School of Mechatronic Engineering, Universiti Malaysia Perlis,
Pauh Putra Campus, 02600 Arau, Perlis, Malaysia

(E-mail: aidakhairunnisaa@yahoo.com, nasirayob@unimap.edu.my, farizhasan@unimap.edu.my)

²Faculty of Electrical Engineering, Universiti Teknologi MARA (UiTM)
Kampus Pasir Gudang, 81750 Masai, Johor, Malaysia

(E-mail: aznilinda@johor.uitm.edu.my, amarf408@johor.uitm.edu.my, fazlina7803@johor.uitm.edu.my)

³Faculty of Electrical Engineering, Universiti Teknikal Malaysia Melaka,
76100 Durian Tunggal, Melaka, Malaysia

(E-mail: hazriq@utem.edu.my)

⁴Faculty of Manufacturing Engineering, Universiti Malaysia Pahang,
26600 Pekan, Pahang, Malaysia

(E-mail: ismailkhai@ump.edu.my)

Abstract - Combinatorial logic circuit minimization is usually done using Karnaugh's Map or Boolean equation. This paper presents an application of Firefly Algorithm to design combinational logic circuit in which the objective function is to minimize the total number of gates used. Then, the algorithm is benchmarked with other literatures. Result indicates that it able to find optimal solution but further analysis is required for a more complex combinatorial logic circuit minimization.

Keywords - Combinational logic circuit minimization; Computational intelligence; Firefly algorithm; Numbers of gates; Swarm intelligence.

1. Introduction

A minimized combinatorial logic circuit brings a lot benefits to the electronic industries. Based on common sense a minimized combinatorial circuit design should bring at least one out of these four benefits: smaller circuit board, reduces propagation, minimizes error, and reduce cost. Thus, it is essential to ensure any circuit design takes into account the minimization of the number gates used.

Nowadays, there are a lot of ways to minimize the design combinatorial logic circuit. Based on the work done by other researchers, they had proposed different model and algorithms to solve the problem. One of them is using Genetic Algorithm (GA) in design the combinatorial logic circuit. This method proposed by S. J. Louis and G. J. E. Rawlins. Two dimensional array structures (phenotype) will be map for each genotype. This array will be presented as circuit design [1].

On the other hands, X.Wang *et.al* [2] proposed an approach to enhance the designing process by using variable topology cartesian genetic programming for combinational circuit. In this paper it used a combination

of GA Evolvable Hardware (EHW), Chromosome Genetic Programming (CGP) and Variable Cartesian Genetic Programming (VCGP). Moreover, it also increases the complexity of space search using random circuit matrix. Besides that, they used symbols to represent a direction such as "*" for horizontal direction and "+" for vertical direction. These symbols were also been used by G.Papa and his co-workers in their binary tree expression [3].

In addition the same method can be used in designing the combinational logic circuit with different algorithms such as GA, Ant Colony System (ACS), and Particle Swarm Optimization (PSO). The model proposes a matrix to represent circuit logic, which is bi-dimensional space, consists of a string of combination gates inputs, gates type, gates outputs. The encoded of the matrix elements for gate type consist of 4 types of gates: AND, NOT, OR, XOR, and WIRE [4].

This paper proposes the application of Firefly Algorithm (FA) in minimizing the number of gates of the combinational logic circuit. The model is adapted from A.Tyrell *et.al* [4] which makes it suitable for direct benchmarking between the algorithms.

2. Combinatorial Logic Circuit Minimization

All of the modern computers consist of logic gates which functioning as a building block of a digital circuit. The computers' microchips are arranged in hundred of combinational logical gates to make sure the efficiency and consistently reliable outputs. Even though, there are no limitation in the number of gates that can be used and with the advancement of microchip technology; the designers need to minimize the amount of logic gate [5].

The case study taken for implementing Firefly Algorithm in minimizing the combinational logic circuit's gates was referred based on study by C. A. Coello *et al.*

[4]. The truth table is as shown in Table 1. From a work done by Tyrell *et.al* [4] they found that by using PSO-based approach it is able to find the solution by using only 4 gates (2 ANDs, 1 OR, 1 XOR) as stated in equation (1) below.

Table 1 Truth table for Combinational Logic Circuit Minimization using Firefly Algorithm

Input			Output
x	y	z	F
0	0	0	0
0	0	1	0
0	1	0	0
0	1	1	1
1	1	0	1
1	1	1	0
1	0	0	0
1	0	1	1

$$F = ((y + z)x)'yz + ((y + z)x)(yz)' \quad (1)$$

3. Implementation of Firefly Algorithm

Firefly Algorithm was proposed by X. S. Yang *et.al* as another SI algorithm that can compete with PSO [6]. The main motivation for using Firefly Algorithm (FA) to design combinational logic circuit is that this algorithm has been found very efficient in a variety of tasks such as solving Traveling Salesman Problem (TSP) [7], routing Very Large Scale Integration (VLSI) circuit [8] and path optimization in PCB holes drilling process [9].

In implementing any Swarm Intelligence (SI) algorithms, the most importance step is to model the problem so that the algorithm can fit the problem. Generally, firefly positions in the search space represent a candidate solution of the problem. A candidate solution should be a feasible solution where feasible solution is solution that produces the desired output according to the truth table. The firefly position x can be translated into a d -dimension of search space where each dimension represents a part of the candidate solution. For this approach, we adopted the model proposed by [4] which can be translated in equation (2) below.

$$x = [Gate1'sID, Gate2'sID, \dots, Gated'sID] \quad (2)$$

As rule of thumb, the number of dimension is dictated by equation (3) which was proposed by Sadiq M. Sait *et.al* [10] where n_i is the number of input in logic circuit.

$$d = n_i^2 \quad (3)$$

Thus, for a 3 inputs logic circuit, the number of dimensions required is 9.

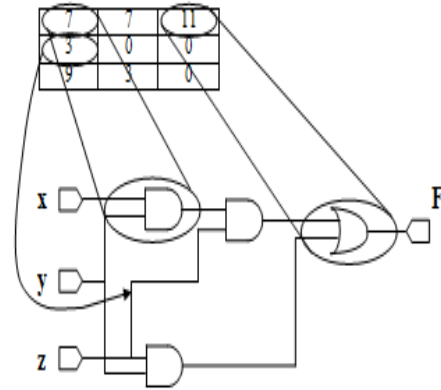


Fig.1. Example of a circuit and its encoding

As stated earlier, the model taken from [4] where each Gate ID can be an integer number range from 0 to 15. Each number has unique combinations of inputs and gate type which presented in Table 2 below.

Table 2 Gate ID and gate types [4]

Gate ID	Inputs	Gate	Output
0	None	None	None
1	x	WIRE1	x
2	y	WIRE2	y
3	z	WIRE3	z
4	x	NOT1	$\sim x$
5	y	NOT2	$\sim y$
6	z	NOT3	$\sim z$
7	x, y	AND1	$x . y$
8	x, z	AND2	$x . z$
9	y, z	AND3	$y . z$
10	x, y	OR1	$x + y$
11	x, z	OR2	$x + z$
12	y, z	OR3	$y + z$
13	x, y	EX-OR1	$\sim x . y + x . \sim y$
14	x, z	EX-OR2	$\sim x . z + x . \sim z$
15	y, z	EX-OR3	$\sim y . z + y . \sim z$

Note that input for 2nd and higher level is based on the input of first level where row 1 is input a, row 2 is input b while row 3 is input c and so on.

3.1 Fitness formulation of Firefly Algorithm

The fitness formulation for FA is the total gates used. The smaller the number of the gates used the better the fitness of that firefly. Figure 2 displays the flowchart of the implementation of FA in solving the combinatorial logic circuit minimization problem. The program starts by initializing the FA parameters. At the same time, the fireflies' positions are randomly generated. Only feasible solutions are accepted, if there any firefly represented unfeasible solution, the position of the firefly is randomly generated again until it found a feasible solution. Then, the fitness of each firefly is evaluated.

Next, the intensity of each firefly is calculated using formula stated in [6]. After that, the intensity of between two fireflies are compared, firefly with better intensity will attract the firefly with lower intensity towards it. The new position of the firefly will be check if it represents a feasible solution. If the new position is a feasible solution, the new solution is accepted, otherwise, the firefly will remained at the old position. Note that during updating the firefly position, two conditions might occur.

First, out of boundary condition in which the new position of the firefly is outside the desired range, in this case, the range is 0 to 15. If this happened, the modulus after division by 16 of the new position is taken as the new solution. For example, 17 will become 2 and -1 will become 15. Another condition that might occur frequently is the new position is a floating number. For this condition, the new solution will be the rounding of the new position. For example, 3.42 will be 3 while 9.91 become 10. The process will be repeated until the maximum iteration reached.

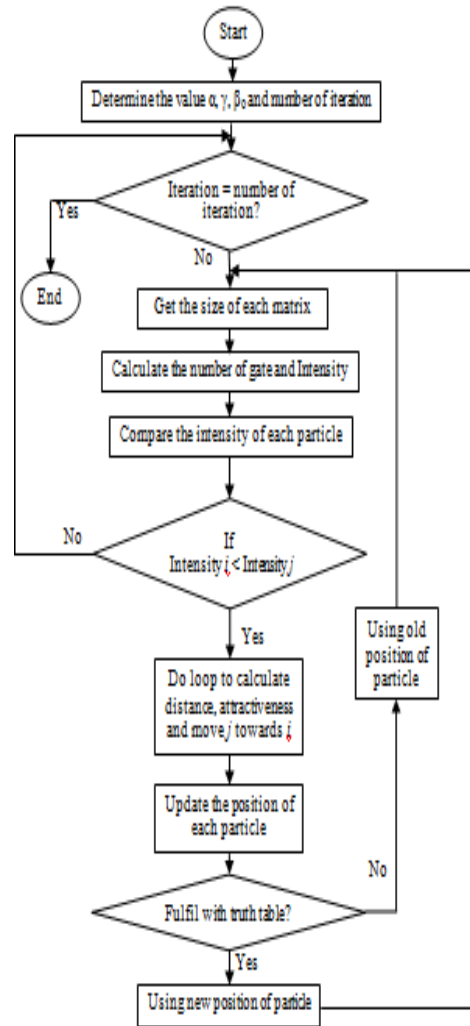


Fig.2. Flowchart of the implementation of FA in solving the combinatorial logic circuit minimization problem.

4. Result and Discussion

4.1 Result and Analysis

The approach is written using MatlabR2010a and run on a laptop with Pentium(R) Dual-Core CPU, 1GB of RAM, 32-bit of operating system and 2.0 GHz of speed. Table 3 stated the parameters used in FA & PSO [4] for the implementation of the proposed approach. Table 4 shows the result obtained from the proposed approach. It can clearly be seen that FA able to find the optimal solution [4].

Table 3 Comparison of the PSO Parameters used by in previous research with this study

	PSO	FA
Common Parameters		
Number of agents, q	90	3
Number of iteration, t	300	15000
Number of computations	20	20
PSO Parameters		
Inertia weight, ω	0.8	Not Applicable
Cognitive component, c_1	Not Applicable	Not Applicable
Social component, c_2	Not Applicable	Not Applicable
r_1 and r_2	Not Applicable	No. of gates for each circuit
FA Parameters		
Attractiveness, β_0	Not Applicable	1
Randomization parameter, α	Not Applicable	0.7
Absorption coefficient, γ	Not Applicable	0.1

Table 4 Comparisons of FA results

PSO [4]	Human Designer 1 [4]
$F = ((y + z)x)'yz + ((y + z)x)(yz)'$ 4 gates 2 ANDs, 1 OR, 1 EXOR	$F = x'yz + xy'z + xyz'$ 11 gates 3 NOTs, 6 ANDs, 2 ORs
FA	Human Designer 1 [12]
$F = ((y + z)x)'yz + ((y + z)x)(yz)'$ 4 gates 2 ANDs, 1 OR, 1 EXOR	$F = x'yz + x(x'z + xz')$ 6 gates 3 ANDs, 1 OR, 1 EXOR, 1 NOT

Figure 4 is the encoded circuit after the simulation of FA using project modeling. From the encoded circuit, project is able to display the circuit using different logic gates. It is shows that circuit has 2 AND gates, 1 OR gate, 1 EXOR gate and 3 wires.

9	1	13	1
1	9	0	0
12	0	0	0

Fig.4. Encoded circuit from the project simulation

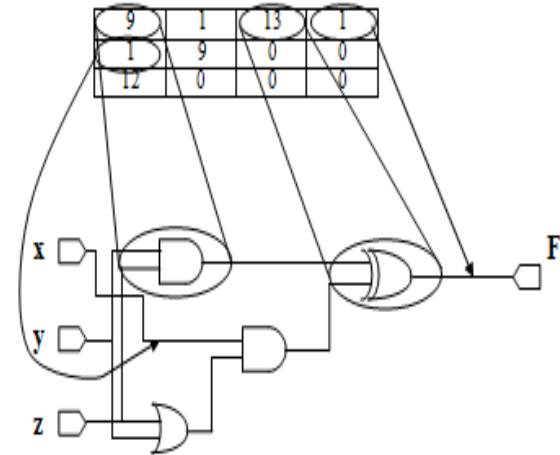


Fig.5. Circuit from the result

5. Conclusion

This paper presents an approach for minimizing number of gates for combinational logic circuit using Firefly Algorithm. The proposed approach is explained extensively and the experimental result also has proved that FA is an efficient algorithm.

Acknowledgment

A special thanks to my supervisor Mohd Nasir bin Ayob and for his advice, support and guidance throughout this research.

References

- [1] S. J. Louis and G. J. Rawlins, Using Genetic Algorithms to Design Structures, 1991.
- [2] W. Xiuqin, W. Hao, and M. Guangsheng, "Variable Topology Cartesian Genetic Programming for Combinational Circuit," in Fourth International Conference on Natural Computation 2008 (ICNC 2008), pp. 306-310, 2008.
- [3] G. Papa and J. Å ilc, "Automatic large-scale integrated circuit synthesis using allocation-based scheduling algorithm," Microprocessors and Microsystems, Vol. 26, pp. 139-147, 2002.
- [4] A. Tyrrell, P. Haddow, J. Torresen, C. Coello Coello, E.n. Luna, and A.n. Aguirre, "Use of Particle Swarm Optimization to Design Combinational Logic Circuits," in Evolvable Systems: From Biology to Hardware. Springer Berlin Heidelberg, Vol. 2606: pp. 398-409, 2003.

- [5] J. F. Wakerly, *Digital Design Principles & Practices*: Upper Saddle River, New Jersey Prentice Hall, 1999.
- [6] X.S. Yang, Firefly algorithm for multimodal optimization. *Stochastic Algorithms: Foundation and Application*, Vol. 5th, 2009.
- [7] S. F. M. Hussein, A. Faiz Zainal Abidin and M. Asraf Mansor, "A Preliminary Study on Firefly Algorithm Approach for Travelling Salesman Problem," in *Science & Engineering Technology National Conference*, 2013.
- [8] M. N. Ayob, F. Hassan, and A. H. Ismai, "A Firefly Algorithm Approach for Routing in VLSI," in *International Symposium on Computer Applications and Industrial Electronics*, pp. 98-102, 2012.
- [9] M. M. Ismail, M. A. Othman, H. A. Sulaiman, M. H. Misran, R. H. Ramlee, A. F. Z. Abidin, N. A. Nordin, M. I. Zakaria, M. N. Ayob, and F. Yakop, "Firefly algorithm for path optimization in PCB holes drilling process," in *Green and Ubiquitous Technology (GUT), 2012 International Conference on*, pp. 110-113, 2012.
- [10] M. Sadiq M. Sait, Abd-El-Barr, U. Al-Saiari, and B. A. B. Sarif, "Fuzzified Simulated Evolution Algorithm For Combinational Digital Logic Design Targeting Multi-Objective Optimization," in *IEEE International Symposium on Circuits and Systems, ISCAS*, 2004.

An Analysis of γ Effects to H_∞ Filter-based Localization

Hamzah Ahmad and Nur Aqilah Othman

Faculty of Electrical and Electronics Engineering, Universiti Malaysia Pahang, 26600 Pekan, Pahang, Malaysia
(E-mail: hamzah,aqilah@ump.edu.my)

Abstract – Instead of using the well-known Kalman filter (H_2 filter), H_∞ filter which is also known as minimax filter, can be used to estimate robot location as part of simultaneous localization and mapping problem. As γ can affects the H_∞ filter performance, the variation of its selection are demonstrated to grasp the overview of the estimation performance. The analysis is divided into two categories; non-moving mobile robot and moving robot for different values of γ . The comparison of the performance between H_∞ filter and Kalman filter is included to differentiate the capabilities of both filters in the localization problem. Simulation results show that, H_∞ filter exhibits better outcomes than the Kalman filter and thus provides another available methods for the solution of SLAM problem.

Keywords – gamma, H_∞ filter, Kalman filter, localization.

1. Introduction

Being designed in 1960's, Kalman Filter is known among the best minimum variance linear unbiased estimator using the Minimum Mean Square Estimation (MMSE) approach and a recursive filter for a system [1, 2]. Successfully applied for nowadays numerous applications, it is a statistical filter that requires modeling the process and measurement errors to have Gaussian white noise with zero mean. Since introduced, Kalman filter been widely used for numerous application worldwide such as in robotics, hydrological and environmental systems, navigation system etc. Unfortunately, it works well under some certain conditions. Above all of its advantages of resulting the smallest standard deviation of estimation error, Kalman filter suffers from some deficiencies such as all noise must be zero mean, and the requirement a priori knowledge for noise standard deviation for both process and measurement noise.

Despite of Kalman filter reputation among decades, some applications still experience problem and need further attention for development. Speaking in the field of autonomous system, estimation problem is a nontrivial issue to be apprehend. Even though Kalman filter may still provide good estimation for some systems, better estimator is still being demand to increase certain autonomous system performance. Practically noise is in uncertain manner and need to be considered carefully when designing a system. Thereby, rather than depending

on assumption of Gaussian white noise with zero mean, it is wise decision to model a system that able to take into account worst case of noise or when the statistics of noise is violated. Hence, the development of H_∞ filter.

In the research of simultaneous localization and mapping (SLAM) [3-9], the process error and measurement errors are often to be non-Gaussian errors and might be in unknown statistics. Therefore, it is a challenge to determine and obtain correct information of robot localization problems and landmarks estimation to build up and achieve a world representation of unknown map. To overcome such shortcomings for a systems of unknown noise characteristics and uncertainties, H_∞ [8, 10] is being proposed as a role of an estimators that able to tolerate with a robust system.

2. H_∞ Filtering: A Robust Filter

Robustness is one of the important criteria to be fulfilled in design a systems that needs a good control and estimation. Firstly introduced around 1987's by Mike Grimble, [2] the only uncertainties remains is in form of bounded energy noise signal in which there is no uncertainty in the matrices of system state space model. In the H_∞ filtering, the noise inputs are deterministic signals and required to be energy- bounded with no other knowledge of noise is needed. It's guarantees that the energy gain from the noise inputs to the estimation error is less than a certain level.

H_∞ filtering has been formulated into 3 main approach such as the Game approach, Riccati Approach and Interpolation theory approach. In contrast with the Kalman Filter, these kind of approach leads to different kinds of equations which lessen its popularity rather than the Kalman filter which is more easier and simpler to be applied. H_∞ filter is also need some tuning to obtain a good system performance which will be clearer through this paper. Eventually, it is worth to tune the filter to attain better performance to a level of desired outcome. The Riccati approach is being applied in this paper. One of the latest researches conducted on the H_∞ Filter was conducted by L. Cheng et al. [11] that investigate the wireless sensor network for indoor mobile robot localization. They proposed the mixed Kalman and H_∞ filter method in delivering the best estimation results especially for distance measurement which can overcome the Non Line of Sight (NLOS) problem. It is also shown in their results that the hybrid system has surpassed the normal EKF, H_∞ filter.

2.1 Prediction, Filtering and Smoothing

Similar to Kalman filtering, there are some other important keywords to be remind concerning about the estimation problem using the H_∞ filtering problem.

- *Filtering*: Estimation of signal process $x(t)$ at time n based on measurement $z(1), z(2), \dots, z(n)$.
- *Prediction*: Estimation of signal process $x(t)$ at future time point, that is beyond time frame of measurement $z(1), z(2), \dots, z(n)$.
- *Smoothing*: Estimation of signal process $x(t)$ at time before n and use subsequent measurement up to time n to “smooth” the estimation error.

3. Foundation of H_∞ Filtering Problem

The H_∞ filtering problem or the minimax estimation problem is represented in this section. Begin considering a linear systems described by the state space form,

$$\dot{x}(t) = Ax(t) + Bw(t), \quad x(0) = x_0 \quad (1)$$

$$y(t) = Hx(t) + Dv(t) \quad (2)$$

$$z = Lx(t) \quad (3)$$

where $x(t) \in \mathfrak{R}^n$ is the state, x_0 an unknown initial state, $w_t \in \mathfrak{R}^l$ the noise signal, $z_t \in \mathfrak{R}^p$ the measurement, and $s_t \in \mathfrak{R}^r$ is a linear combination of state variables to be estimate under horizon $[0, T]$, where $T > 0$ using the measurements $z(\tau), 0 \leq \tau \leq t$. If L matrix is an identity matrix, x will be the estimation to be obtained.

Assumption 1: $R \triangleq DD^T > 0$

Do note that above assumption is similar to the standard Kalman filter assumption filtering where all components of the measurement vector are assumed to be corrupted by noise.

Assumption 2: Bounded noise energy;

$$\sum_{t=0}^N \|w_t\|^2 < \infty, \quad \sum_{t=0}^N \|v_t\|^2 < \infty$$

From $\Sigma_0 > 0, Q_t > 0$, and $R_t > 0$ which is the weighting matrix for x_0 , noise w_t , and v_t respectively, for $\gamma > 0$, a finite horizon H_∞ filtering problem is a problem that must be satisfying the estimation of $\hat{z}_t = \hat{z}_t^*$, $t = 0, 1, 2, \dots, N$. This is shown as

$$\sup_{x_0, v, w} = \frac{\sum_{t=0}^N \|z_t - \hat{z}_t\|^2}{\|x_0 - \bar{x}_0\|_{\Sigma_0^{-1}}^2 + \sum_{t=0}^N \|v_t\|_{R_t^{-1}}^2 + \sum_{t=0}^N \|w_t\|_{Q_t^{-1}}^2} < \gamma^2 \quad (4)$$

The above equation represent that the ratio of estimation error noise and the noise energy bounded for all noise is less than a specified values which is γ in this problem. It is being proved that if the bigger the value of γ , the filter will be reacting familiar to Kalman filter.

A cost function can being applied to look from the aspect of Finite Horizon a priori and a posteriori H_∞ filtering problem as shown below.

$$J(\hat{z}; x_0, v, w) = \sum_{t=0}^N \|z_t - \hat{z}_t\|^2 - \gamma^2 \left(\|x_0 - \bar{x}_0\|_{\Sigma_0^{-1}}^2 + \sum_{t=0}^N \|v_t\|_{R_t^{-1}}^2 + \sum_{t=0}^N \|w_t\|_{Q_t^{-1}}^2 \right) \quad (5)$$

where $\hat{z} = (\hat{z}_0, \hat{z}_1, \dots, \hat{z}_N)$, $v = (v_0, v_1, \dots, v_N)$, and $w = (w_0, w_1, \dots, w_N)$. In comparison to (1), it is explicitly clear that,

$$\max_{x_0, v, w} J(\hat{z}; x_0, v, w) < 0, \quad (x_0 - \bar{x}_0, v, w) \neq 0$$

or

$$\min_{\hat{z}} \max_{x_0, v, w} J(\hat{z}; x_0, v, w) < 0, \quad (x_0 - \bar{x}_0, v, w) \neq 0$$

which is a minimax problem consisting of two main player, \hat{z} and (x_0, v, w) . \hat{z} will be minimizing $J(\hat{z}; x_0, v, w)$ while (x_0, v, w) will be maximizing $J(\hat{z}; x_0, v, w)$.

Rearranging above statements, it can be concluded that the H_∞ filtering problem can be stated as follows;

Given a prescribed level of “noise” attenuation $\gamma > 0$ and an initial state weighting matrix $\Sigma_0 = \Sigma_0^T > 0$, find linear causal filter F such that in the finite horizon case, $J(\hat{z}; x_0, v, w) < \gamma$ when $x_0 = 0$.

The resulting filter will be known as H_∞ suboptimal filters which is said to achieve a level of noise attenuation, γ .

In this paper, the a posteriori output of filter is being observed for comparison purposes with Kalman filter later on.

Assumption 3: Rank $F_t = n$, for all $t = 0, 1, \dots, N$.

If the above Assumption 3 is fulfilled, for a solution of a posteriori H_∞ filtering problem to be exist, the Riccati equation

$$P_{t+1} = F_t P_t \psi_t F_t^T + G_t Q_t G_t^T, \quad P_0 = \sigma_0 \quad (6)$$

$$\psi_t = I_n + \left(H_t^T R_t^{-1} H_t - \gamma^{-2} L_t^T L_t \right) P_t \quad (7)$$

holding a positive definite solution and

$$\hat{P}_t^{-1} - \gamma^{-2} L_t^T L_t > 0, \quad t = 0, 1, \dots, N \quad (8)$$

At this time, for $\gamma > 0$ suboptimal H_∞ filter are given by following equation:

$$\hat{z}_t^* = L_t \hat{x}_{t|t}, \quad \hat{x}_{t+1|t} = F_t \hat{x}_{t|t} \quad (9)$$

$$\hat{x}_{t|t} = \hat{x}_{t|t-1} + K_t [y_t - H_t \hat{x}_{t|t-1}], \quad \hat{x}_{0|t-1} = \bar{x}_0 \quad (10)$$

$$K_t = P_t H_t (H_t P_t H_t^T + R_t)^{-1} \quad (11)$$

4. Simulation Result and Discussion

In order to understand and evaluate the performance of H_∞ filter, some simulation is being carried out to observe the filter characteristics with some comparison with Kalman filter. Following simulation setup is being defined to obtain and achieve a good comparison:

- Noise are Gaussian white noise
- Zero mean noise
- Simulation are in planar world
- Landmarks are stationary
- Process noise, $Q = 0.03^2 * I(6)$
- Measurement noise, $R = 0.3 * I(2)$

4.1 Case 1: H_∞ Filter Performance Analysis

Here are some of the results obtained when the value of γ is changed. From the theoretical aspects, the bigger the value of γ , the results will be close to the Kalman filter characteristics as shown on Fig. 1. As shown on this figure, it is very critical in choosing the γ value. The significant value of γ can handsomely provides good estimation results, hence better accuracy (note that the true value is 1 for Fig.1, Fig.2, Fig.3, Fig.4 and Fig.5).

As been shown by the figure, the estimation varies as the γ changed but remains stable at a constant value after it reach some value. If the characteristic doesn't change hereafter, this feature is said to be close to the Kalman filter characteristics. Although that it is seems to be very small change of estimation value between γ , the characteristics will be slightly change when employing bigger noise effect to the systems. As can be seen, the $\gamma = 10$ shows some unexpected outcome for bigger noise effect than $\gamma = 100, 1000$ and still under analysis to determine its cause. This is shown later on Fig. 8 and Fig. 9.

Furthermore, by analyzing these characteristic in changing the values of γ , it is found that, the results will be diversely changing after below the value of 0.5. From Fig. 2, when the smaller value of γ applied on the filter, the estimation become more unstable and changing frequently due to more noise effect included into the system. The smaller the γ , H_∞ filter will become more sensitive to the measurement noise. Consequently, the solution for sub-optimal H_∞ filter will be not exist and systems cannot function well. This value will be an important reference point for designing an appropriate H_∞ filter to achieve certain desired output.

On the other hand, interestingly comparing these γ to acquire best γ value, $\gamma = 1.01$ gives the best results as shown on the Fig. 3. However, do note that the value may abruptly change for other conditions that are not specified here.

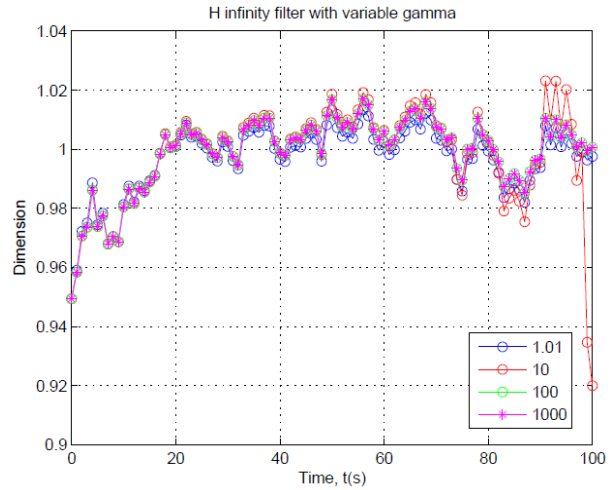


Fig. 1. H_∞ characteristics.

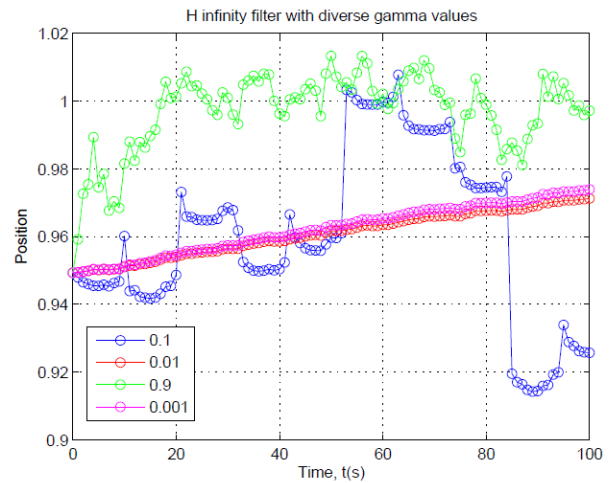


Fig. 2. H_∞ γ characteristics: Diverse γ values.

The investigation goes through the evaluation for noise effect to the system. Noise applied to the system is change in a manner to determine and examine its effects to H_∞ filter behavior. Results are shown below. As been shown on Fig. 4, the bigger value of noise will rapidly change the behavior of the filter or estimation. In contrast, the smaller the noise, estimation value will be approximating the true value of the systems.

4.2 Case 2: Non Moving Mobile Robot Observing One Landmark at World Coordinate System

The comparison to the well-known Kalman filter is presented. A non-moving case of a mobile robot that simultaneously observing one landmark and at the same time localizing itself to the unknown environment is being studied using an extended kalman filter and the robust H_∞ filter.

As shown on Fig. 5, Kalman filter converge faster than H_∞ filter. From the characteristics shown on this figure, H_∞ filter estimation error is more reliable due to it approximately near to the true value than the Kalman

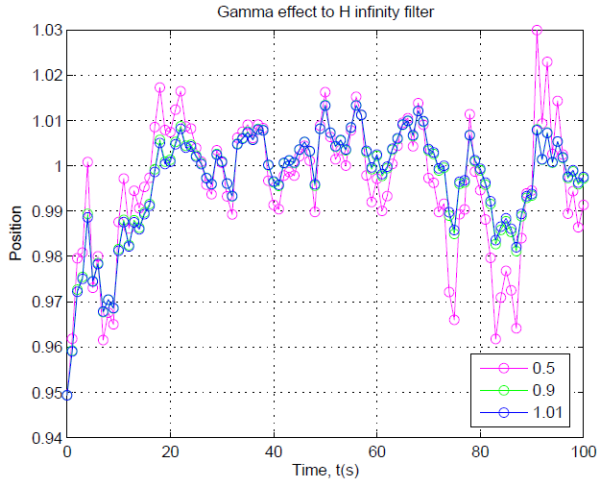


Fig. 3. H_∞ γ characteristics: Best γ values.

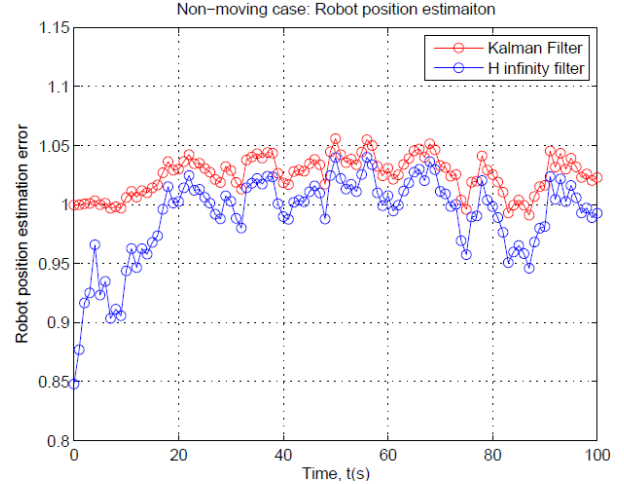


Fig. 5. H_∞ filter non-moving case: Robot position estimation.

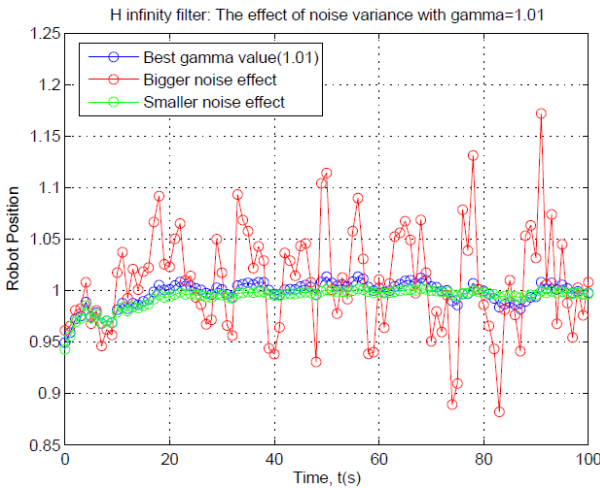


Fig. 4. H_∞ filter: Noise effect to the system.

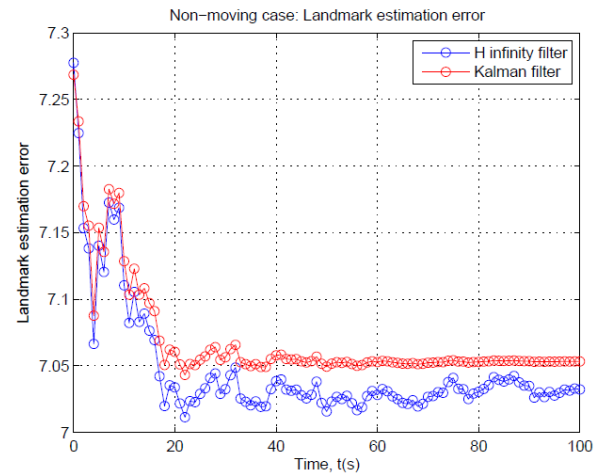


Fig. 6. H_∞ filter non-moving case: Landmark estimation with 7 as true value.

filter estimation for true position estimation. Analysis from the average value of both filters resulting below consequences;

- Mean calculation for Kalman filter of robot location = 1.0669
- Mean calculation for H_∞ filter of robot location = 0.9833

Furthermore, the H_∞ filter oscillates around its true value and better than Kalman filter that is somehow still trying to approximate the true value.

As in Fig. 6, the estimation using H_∞ filter surpassed the estimation using Kalman filter for landmark estimation. The characteristics express that the use of H_∞ filter gives a promising results than Kalman filter especially in real and practical situations although that it oscillates bigger than the Kalman filter.

Analyzing the uncertainty, it is found that, the landmark uncertainty is decreasing as many more observations are made to the system. Do note that, in this paper, the relative location between robots and landmarks is the objective. At the beginning, H_∞ filter shows small deviation of landmark estimation uncertainty rather than Kalman filter. As time passed, even though it is seems

that Kalman filter shows a constant output at the end of the simulation, the real landmark estimation value is still not the true value, as stated above in terms of it average estimation.

Based on these two results of above case, this gives an induction and probability of better performance and estimation for a robot observing more and more landmarks while also encouraging outcome for a case where moving mobile robot taking relative observation from some landmarks.

The result for $t=10000s$ simulation time for $\gamma = 0.01$ and $\gamma = 0.001$. The estimation error fluctuates at approximately 1.05 which is a big error from its true value, i.e. 1.

As for looking into the correction of error for both filters, below figure shows the difference between these filters. From this figure, it is clear that Kalman filter tries to minimize the variance of estimation error while the H_∞ provide an uniformly small estimation error for the systems (the big variance between data in each step shows that the estimation error is being suppress under certain level).

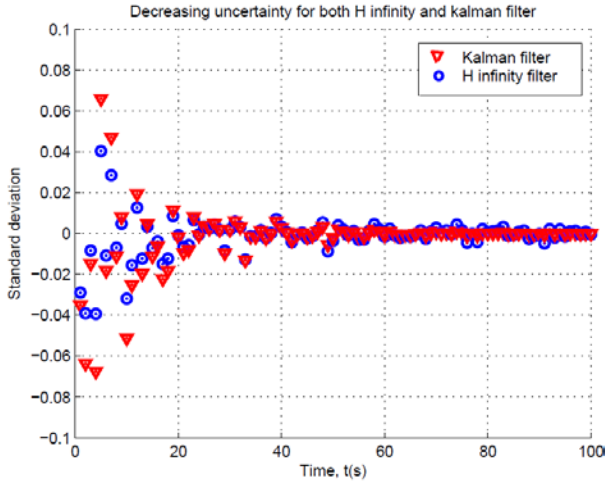


Fig. 7. Uncertainty decreasing: Landmark estimation.

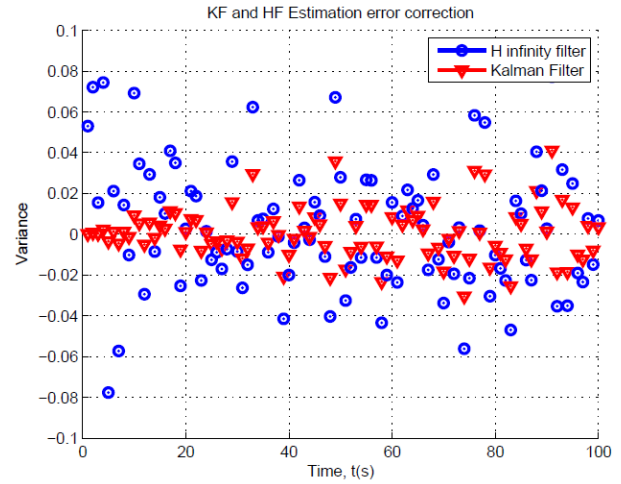


Fig. 9. Kalman filter and H_∞ filter error comparison.

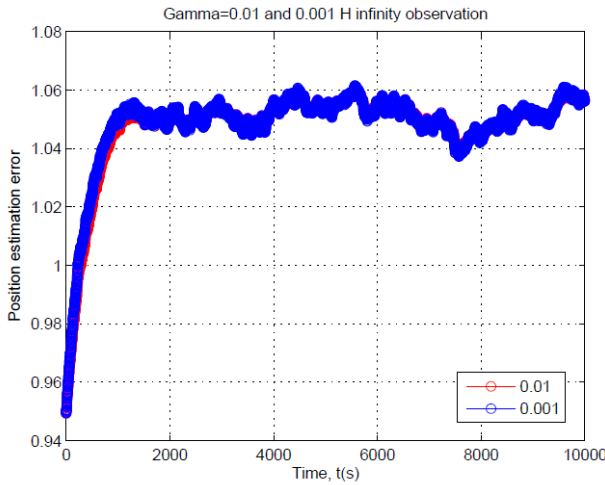


Fig. 8. γ characteristics of H_∞ filter for $\gamma = 0.01$ and $\gamma = 0.001$.

5. Conclusion

Above mentioned results determined the promising results using the H_∞ filter as an alternative way for estimation problem. This approach is still new and may need further improvement and development to achieve even more stable and encouraging results than being attained in this paper. Even though the development of H_∞ filter is widely diversely approach among researchers, it will be an interesting researches by researchers to extent its advantages for an enormous application widely over the world such as target tracking, system identification, localization, etc. Despite some of its inadequacy, it provides a good estimation rather than other Kalman filter algorithm, EM algorithm and other existed algorithm.

From this paper, it is clear that H_∞ filter are capable to predict and approximate linear and non-linear system that has wide coverage and variety of noise and proven to be useful for Simultaneous Localization and Mapping Problem (SLAM) that recently being explore and study.

However, one should note that, H_∞ filter are more sensitive at lower level of γ to design a proper system.

Acknowledgment

The authors would like to thank KPM and UMP for the support to the research under research grant RDU130106.

References

- [1] T Katayama, "Adaptive Kalman Filter", Asakura Shoten, 2000.
- [2] F.L Lewis, L.Xie, D.Popa, "Optimal and Robust Estimation", 2nd.Ed. CRC Press, 2008.
- [3] H.Ahmad, T. Namerikawa, "Robot Localization and Mapping Problem with Unknown Noise Characteristic", 2010 IEEE Multi-conference on Systems and Control, Yokohama, Japan, pp.1275-1280, 2010.
- [4] M.W.M.G Dissanayake, P.Newman, S.Clark, H.F Durrant-Whyte, M.Csorba, "A solution to the Simultaneous Localization and Map Building(SLAM)Problem", IEEE Transaction on Robotics and Automation, Vol. 17, No.3, June 2001.
- [5] S.Huang, G.Dissanayake,"Convergence and consistency analysis for Extended Kalman Filter Based SLAM", IEEE transaction on robotics, Vol.23, No.5, October 2007.
- [6] H.Ahmad, T.Namerikawa, " H_∞ Filter convergence and its application to SLAM ", ICROS-SICE International Joint Conference, pp.2875- 2880, 2009.
- [7] H.Ahmad, T.Namerikawa, Extended Kalman Filter based Mobile Robot Localization with Intermittent Measurement, System Science & Control Engineering: An Open Access Journal, Vol.1, pp. 113-126, 2013.

- [8] H.Ahmad, T.Namerikawa, "Intermittent Measurement in Robotic Localization and Mapping with FIM Statistical Bound", IEEJ Transaction on Electronics, Information and Systems, Section C, C, Vol.131, No.5, Sec. C, pp. 1223-1232, 2011.
- [9] H.Ahmad, T.Namerikawa, "Feasibility Study of Partial Observability in H^∞ filtering for Robot Localization and Mapping Problem", American Control Conference (ACC2010), pp. 3980-3985, 2010.
- [10] O.Yoshihiro, T.Namerikawa, "Simultaneous localization and mapping problem via the H filter with a known landmark", SICE Annual Conference (SICE), pp.1939 - 1944, 2013.
- [11] L.Cheng, H.Wu, C.Wu, Y.Zhang, "Indoor Mobile Localization in Wireless Sensor Network under Unknown NLOS Errors", International Journal of Distributed Sensor Networks, Paper ID 208904, Hindawi Publishing Corporation, 9 pages, 2013.

Gaharu Sensor: Classification Using Case Based Reasoning (CBR)

Muhamad Faruqi Zahari¹, Muhammad Sharfi Najib², Kamarul Hawari Ghazali³, Fathimah Abdul Halim⁴, Saiful Nizam Tajuddin⁵, Erny Haslina Abd Latib⁶

^{1, 2, 3, 4} Faculty of Electrical and Electronic Engineering, Universiti Malaysia Pahang, Pekan, 26600, Pahang, Malaysia
¹ (E-mail: mei13002@stdmail.ump.edu.my¹, sharfi@ump.edu.my², kamarul@ump.edu.my³, fathimah.halim@yahoo.com⁴)

^{5, 6} Faculty of Industrial Science and Technology, Universiti Malaysia Pahang, Gambang, 26300, Pahang, Malaysia
 (E-mail: saifulnizam@ump.edu.my⁵, ernyhaslina87@gmail.com⁶)

Abstract – Agriculture was an important industry, which has an economic impact of trading goods for others application such as perfume, aromatherapy and others. Agar wood one of high value products that give economic impact for several of the countries which price of agar wood to its certain grade. The grades were manipulated by traders to get higher price using lower grade. This paper proposed the intelligence classification technique using an Electronic Nose (E-nose) measurement. The sensor array in the E - nose are used for the inputs of the Case Based Reasoning (CBR) for intelligent classification. The experimental result shows that the technique accomplished to classify with high accuracy which is 96.3% nearly to 100% of accuracy.

Keywords - Agar wood, Gaharu, E-nose, Classification, CBR.

1. Introduction

Agricultural defined as encompassing crop, forest product and the process of the state's agricultural production. Therefore, agricultural can give economic impact to the state's because the agricultural industry purchases goods and services from other industries and hires local labor [1]. One of high value products in agricultural industry was agar wood or gaharu which is used as a traditional aromatic, incense smoke and perfume in many forms such as burning wood chip, make an essential oil for perfumes and others [2]. In the eight century, agar wood also used as medical product that's been recorded in Sahih Muslim and Ayurvedic medical text the Susruta Samhita. In addition, over the past about 30 years, the demand for agar wood has been risen [3], [4].

Agar wood oil quality grading does not have common grading standard to distinguish its quality such as high grade, commercial grade, low grade, Grade A+, Grade A, Grade B and others. The oil quality of grade A+ was 100% of purity and grade A was 95 % to 99%, while the purity of grade B lower than purity of grade A [5]. The common characteristic that can be recognized for grade A was Dark, Dense, Concentrated and Heavy while other characteristic as in Table 1 [6], [7]. This characteristic can be manipulated by traders and they can change the

characteristic of other grade or other wood in order to get the higher price to sell because the better the grade the price was higher [8]–[10].

Table 1 Grades and prices of agar wood at local levels, 1985-2007

		Terengganu 1985	Terengganu 1999- 2000	Hulu Perak 2002-2007	Central Pahang August 2007
Grade	Characteristics	Price (RM/kg)	Price (RM/kg)	Price (RM/kg)	Price (RM/kg)
A	Dark, dense, concentrated and heavy	1,000	3,200-4,000	3,000-7,000	10,000
B	Purple dark, less dense, small holes	250	1,800-2,500	1,500-4,000	5,000-7,000
C1	Yellow dark stripes	150	400-800	500-1,500	2,000
C2	Dark yellow	-	40-80	50-200	150
D	Gaharu remains	-	8-30	4-50	-

In order to detect the quality of agar wood, there are several methods for detection such as Gas Chromatography- Mass Spectrometry (GC-MS), Solid Phase Micro-extraction (SPME) in the chemical field and electronic nose (E-nose) for gaharu quality detection in electronic field. GC-MS is an instrument that can separate and analyzed samples based on chemical compound usually used for agar wood essential oil while SPME is a solvent-less extraction technique, based on adsorption which usually for analyze samples and for burning chip of agar wood [12], [16], [17]. An E-nose is able to detect odors for a variety of applications such as cherry essential oil, liquor, perfumes and others [18], [19]. There are several methods that can imply to classify the quality of gaharu essential oil such as an Artificial Neural Network (ANN), Principal Component Analysis (PCA), k-Nearest Neighbor (k-NN) and also Case Based Reasoning (CBR) [20], [21]. CBR is mean by using stored case to solve the new case. There are several steps for classifying using CBR which is retrieve, reuse, revise and retain [22]. Retrieve is the most crucial step in CBR which is to recall a previous case that stored in CBR. Then, it will retrieve the best similar cases to compare with new case. The best of similarity cases will reuse in order to revise the case and retained it when it was solved [23].

Therefore, this study recommends the classification technique by a combination of the E - nose and CBR for gaharu sensor based on pure and mixed gaharu with other essential oil. The E - nose was used to detect the odor profile of samples. While, CBR classifies the odor based on profile from the E-nose.

2. Experimental Section

The essential oil was extracted using hydro distillation process which is using alcohol in order to extract the essential oil from the plant which cannot undergo the steam distillation process. Then, the essential oil will analyze by GC-MS which is most frequently used technique to classify the compound in essential oil [24]. While, for incense smoke or burning chip using SPME method to get chemical compound analysis, which is to classify to chips A, B and C.

The essential oil has been processed using hydro distillation to get pure gaharu essential oil. Then, it will mix with other essential oil such as lemon or lavender to make it into three samples of essential oil, which is pure gaharu, gaharu mix with lemon and gaharu mix with lavender.

The system acquisition of data as shown in Figure 1. The E - nose will take the repeated reading data of the sample which determined by GC-MS. The data from the E-nose, which consist of an array of sensor in order to get the pattern of the each sample. The data will analyze and CBR will do the classifying of the sample. Then, the similarity is used for accuracy percentage of CBR as follow in Eq. (1) where x is the highest similarity percentages as follows;

$$Accuracy_Percentage = \frac{\sum x}{3} 100 \quad (1)$$



Fig. 1: Data Acquisition System

3. Result and Discussion

The E-nose data which normalized to obtain standard value from 0 to 1. The data have been processed into the graph plot in order to obtain a pattern for each sample as profile odor of gaharu. Figure 2, Figure 3 and Figure 4 show a normalized sample measurement data for pure gaharu essential oil and mixed gaharu essential oil. The data of measurement collected from an array of sensor which is to obtain pattern profile to differentiate the quality of gaharu. The three figures above have conclude that there are slight differences between those figures by its features profile. Its show that, this oil can be manipulated by traders which the human nose cannot detect the differences between those samples.

In addition, these features were improved by using boxplot. The purpose of using boxplot is to summarized and visualized the difference between those samples of gaharu essential oil.

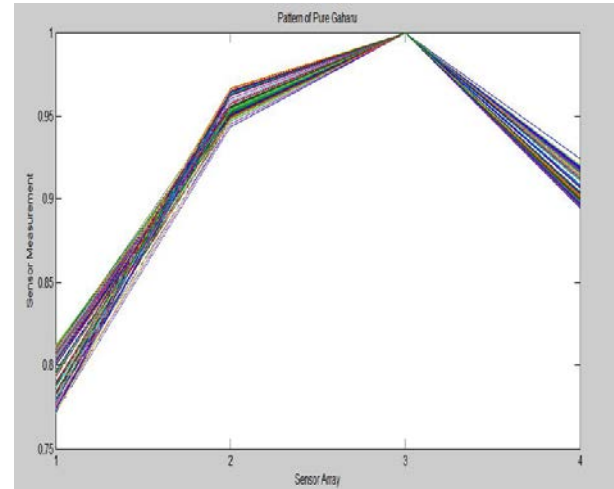


Fig. 2: Normalized data for Pure gaharu

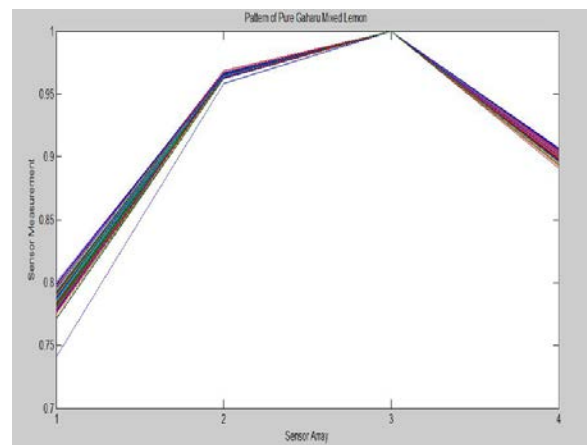


Fig. 3: Normalized data for gaharu mixed lemon

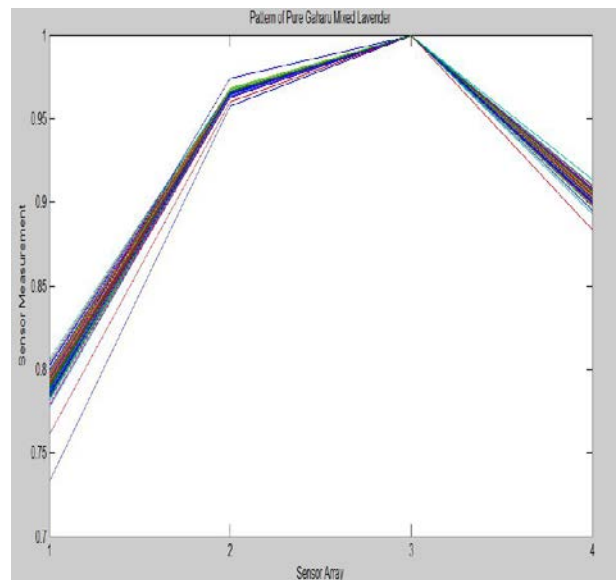


Fig. 4: Normalized data for gaharu mixed Lavender

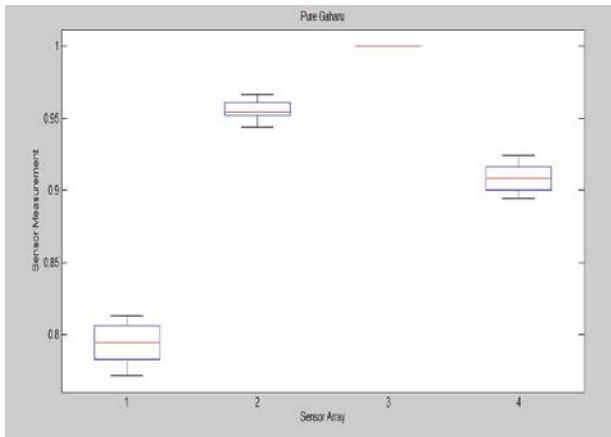


Fig. 6: Box plot for pure gaharu

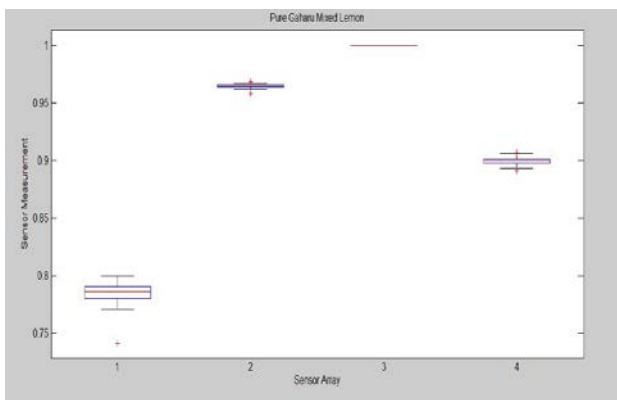


Fig. 7: Box plot for pure gaharu mixed lemon

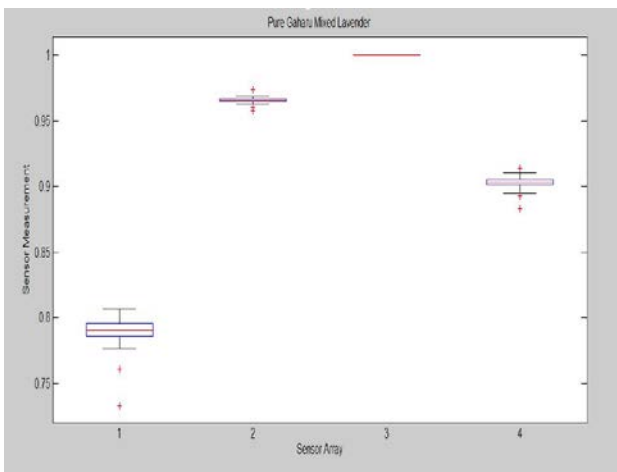


Fig. 8: Box plot for pure gaharu mixed lavender

The simple boxplot displays five statistics, which is minimum, first quartile, median value, third quartile, and maximum value. As we known, these statistics were calculated for a single continuous variable, but the simple boxplot takes it a step beyond. The simple boxplot displays the several categories of a discrete variable by separating the continuous variable of five statistics as mentioned.

Based on the Figure 5, Figure6 and Figure 7, it visualized that difference between those samples. The red center line which is median values was in the box of lower and upper quartiles which known as Inter-quartiles range.

While, the maximum and minimum values of each sensor as a line in boxplot which known as a whisker. Those figures consist a red line at sensor 3 which have the same value of five statistic of each sample. Figure6 and Figure 7, the four boxplots have nearly identical values. While Figure 5 shows the boxplot are different compare to mixed gaharu samples, it is concluded that the boxplot of the four sensors is slightly different.

The pattern of boxplot and the normalized sample graph shows that there are differences of pattern between those samples. Then, the significant data of mean were selected to training for classifier which is CBR. Each samples have 10 cases to get classify. Since the classifier has 20 cases maximum range, the 10 cases of each sample are trained for 2 samples for each classifier training and testing samples. The training and testing will find the percentage of similarity and at the end of the classifier will show the accuracy percentage of classifying between those samples. The accuracy percentage which has recorded as Table 2 below.

Table 2 Accuracy Percentage of CBR

No.	Classifying Cases	Accuracy Percentage
1	Pure gaharu and Pure mixed Lemon	96.3%
2	Pure gaharu and Pure mixed Lavender	96.3%

The classifier accuracy percentage success rate for both sample data test is 96.3 %. The data were classified by using similarity percentage of 20 samples case for testing and training samples.

4. Conclusion

This study of the application of CBR in classifying the purity of gaharu was accomplished through the accuracy percentage of CBR. The purity of gaharu and mixed gaharu with other essential oil classify based on features and statistical value which is by graph plot and boxplot features.

The result shows the classification nearly approaches 100% of accuracy which is 96.3%. In addition, this study can be further refined for better classification using CBR.

Acknowledgement

The authors would like to thank all staff and student involved, Faculty of Electrical and Electronics Engineering, Faculty of Industrial Science and Technology, UMP and excellent fund from UMP Research Grant coded RDU130370.

References

- [1] R. A. Lopez, D. Joglekar, C. Zhu, P. Gunther, and F. Carstensen, "Economic Impacts of Connecticut's Agricultural Industry," 2010.
- [2] M. Antonopoulou, J. Compton, L. S. Perry, and R. Al-Mubarak, "The Trade and Use of Agarwood (Oudh) In The United Arab Emirates," 2010.
- [3] A. Barden, N. Awang Anak, T. Mulliken, and M. Song, "Heart of the matter: agarwood use and trade and cites implementation for *Aquilaria Malaccensis*."
- [4] T. W. Lim and N. Awang Anak, "Wood for the Trees : A Review of the (Gaharu) Trade In," 2010.
- [5] P. Chetpattananondh, "Overview of the agarwood oil industry," in IFEAT International Conference, 2012, no. November, pp. 131–138.
- [6] I. R. Sitepu, E. Santoso, and M. Turjaman, "Identification of Eaglewood (Gaharu) Tree Species Susceptibility," 2011.
- [7] R. Mohamed, M. T. Wong, and R. Halis, "Microscopic Observation of 'Gaharu' Wood from *Aquilaria malaccensis*," *PERTANIKA Journals*, vol. 36, no. 1, pp. 43–50, 2013.
- [8] H. F. Lim, M. P. Mamat, and Y. S. Chang, "Production, Use and Trade of Gaharu in Peninsular Malaysia," in International Economic Conference on Trade & Industry, 2007, no. December, pp. 1–10.
- [9] G. A. Persoon, "Agarwood : the life of a wounded tree," Autumn, 2007.
- [10] M. F. Mamat, M. R. Yacob, H. F. Lim, and A. Rdam, "Costs and Benefits Analysis of *Aquilaria* Species on Plantation for Agarwood Production in Malaysia," *Int. J. Bus. Soc. Sci.*, vol. 1, no. 2, pp. 162–174, 2010.
- [11] N. Ismail, N. Azah, M. Jamil, F. Rahiman, S. Nizam, and M. N. Taib, "Analysis of High Quality Agarwood Oil Chemical Compounds By Means Of Spme / Gc-Ms and Z-Score Technique," *Malaysian J. Anal. Sci.*, vol. 17, no. 3, pp. 403–413, 2013.
- [12] S. Sokima, "Comparison Between Chemical Compounds in Gaharu Smoke (Burning) And Gaharu Oil (Hidrodistillation)," *Universiti Malaysia Pahang*, 2008.
- [13] W. Hidayat, A. Y. M. Shakaff, M. N. Ahmad, and A. H. Adom, "Classification of agarwood oil using an electronic nose." *Sensors (Basel)*, vol. 10, no. 5, pp. 4675–85, Jan. 2010.
- [14] N. Ismail, M. Hezri, and F. Rahiman, "Classification of the Quality of Agarwood Oils from Malaysia using Z- S core T echnique," in IEEE 3rd International Conference on System Engineering and Technology, 2013, pp. 19–20.
- [15] Y. Liu, H. Chen, Y. Yang, Z. Zhang, J. Wei, H. Meng, W. Chen, J. Feng, B. Gan, X. Chen, Z. Gao, J. Huang, B. Chen, and H. Chen, "Whole-tree agarwood-inducing technique: an efficient novel technique for producing high-quality agarwood in cultivated *Aquilaria sinensis* trees.," *Molecules*, vol. 18, no. 3, pp. 3086–106, Jan. 2013.
- [16] X. L. Zhang, Y. Y. Liu, J. H. Wei, Y. Yang, Z. Zhang, J. Q. Huang, H. Q. Chen, and Y. J. Liu, "Production of high-quality agarwood in *Aquilaria sinensis* trees via whole-tree agarwood-induction technology," *Chinese Chem. Lett.*, vol. 23, no. 6, pp. 727–730, Jun. 2012.
- [17] M. H. H. M. F. Azlina, C. M. Hasfalina, Z. A. Zurina, and J. Hishamuddin, "Optimization and Kinetic Study of Gaharu Oil Extraction," *World Acad. Sci. Eng. Technol.*, vol. 7, pp. 1920–1923, 2013.
- [18] M. S. Najib, N. A. M. Ali, M. N. M. Arip, M. A. Jalil, and M. N. Taib, "Classification of Agarwood using ANN," *Int. J. Electr. Electron. Syst. Res.*, vol. 5, no. June, pp. 20–34, 2012.
- [19] M. S. Najib, M. N. Taib, N. A. M. Ali, M. N. M. Arip, and A. M. Jalil, "Classification of Agarwood grades using ANN," *Int. Conf. Electr. Control Comput. Eng.* 2011, pp. 367–372, 2011.
- [20] N. Ismail, M. Hezri, and F. Rahiman, "The Grading of Agarwood Oil Quality using k- Nearest Neighbor (k-NN)," in IEEE Conference on Systems, Process & Control (ICSPC2013), 2013, no. December, pp. 13–15.
- [21] N. Ismail, N. Azah, M. Ali, M. Jamil, M. Hezri, F. Rahiman, and S. Nizam, "Differentiating Agarwood Oil Quality Using Artificial Neural Network," *Malaysian J. Anal. Sci.*, vol. 17, no. 3, pp. 490–498, 2013.
- [22] J. L. Kolodner, "An introduction to case-based reasoning," *Artif. Intell. Rev.*, vol. 6, no. 1, pp. 3–34, 1992.
- [23] D. H. Jonassen and J. Hernandez-serrano, "Case-Based Reasoning and Instructional Design : Using Stories to Support Problem Solving," *ETR&D*, vol. 50, no. 2, pp. 65–77, 2002.
- [24] A. C. Benedict, "Extraction of the Essential Oil of *Aquilaria Malaccensis* (Gaharu) Using Hydro-Distillation and Solvent Extraction Methods V Ashwin," *Universiti Malaysia Pahang*, 2009.

Gravitational Search Algorithm for Assembly Sequence Planning

Ismail Ibrahim¹, Zuwairie Ibrahim², Hamzah Ahmad³, Mohd Falfazli Mat Jusof⁴, Zulkifli Md. Yusof⁵, Sophan Wahyudi Nawawi⁶ and Marizan Mubin⁷

^{1,2,3,4} Faculty of Electrical and Electronics Engineering, Universiti Malaysia Pahang, 26600, Pekan, Pahang, Malaysia
(E-mail: pee12001@stdmail.ump.edu.my, zuwairie@ump.edu.my, hamzah@ump.edu.my, falfazli@ump.edu.my)

⁵ Faculty of Manufacturing Engineering, Universiti Malaysia Pahang, 26600, Pekan, Pahang, Malaysia
(E-mail: zmdyusof@ump.edu.my)

⁶ Faculty of Electrical Engineering, Universiti Teknologi Malaysia, 81310, Skudai, Johor, Malaysia
(E-mail: sophan@fke.utm.my)

⁷ Faculty of Engineering, Universiti Malaya, 50603, Kuala Lumpur, Malaysia
(E-mail: marizan@um.edu.my)

Abstract - Assembly sequence planning (ASP) refers to the process of arrangement of a particular assembly sequence with regard to a product design. In assembly sequence planning, the relationships between components such as the geometry of compliant assemblies should be taken into account before a precedence diagram is eventually built and feasible assembly sequences can be generated. A better assembly sequence can contribute to reduce the cost and time of the manufacturing process, that is, among NP-hard problems. Thus, it is needed to find the optimal sequence from the feasible assembly sequences. In past few years, many optimization techniques have been used to solve the assembly sequence planning problem include Simulated Annealing (SA), Genetic Algorithm (GA), and binary Particle Swarm Optimization (BPSO). In this paper, an approach using Gravitational Search Algorithm (GSA) which is a heuristic optimization algorithm that incorporates the Newton's law of gravity and the law of motion into analytical studies of systems is proposed to solve the assembly sequence planning problem. The experimental results show that the proposed approach is more efficient in solving the assembly sequence planning problem, with less of total assembly time in comparison with the three other approaches.

Keywords – Assembly sequence planning. Meta-heuristics. Gravitational search algorithm. Precedence matrix.

1. Introduction

Assembly sequence planning, which is an important part of assembly process planning, plays an essential role in the manufacturing industry. The focus of ASP is to determine the order of assembly of a product in the assembly line to shorten the assembly time or save the assembly cost [1].

Assembly sequence planning consists of assembly, operations, existing assembly techniques and some details of relations between parts [2]. Some researchers have dedicated their work on some important issues related to concurrent engineering analyses on assembly sequence planning [3]. These issues are the representation of a

product to be assembled, the generation of assembly sequence plans and the determination of precedence constraints, the representation of resulting assembly sequence plans and the selection of the optimum assembly sequence planning.

Many works have intensely done on assembly sequence planning systems using meta-heuristics approaches [4-6]. The implementation of meta-heuristics in solving discrete optimization problems, particularly in the ASP problem lead to significant reduction of computational times, which by its nature sacrifices the guarantee of finding exact optimal solutions [7,8]. However, these approaches are permitted to obtain acceptable performance at acceptable costs in a large number of possible assembly sequences. In other words, these approaches able to find good solution on large-size problem instances.

In past few years, a stochastic population-based meta-heuristic called Gravitational Search Algorithm (GSA) has been developed [9]. GSA is inspired by the Newton's law of universal gravitation where all objects attract to each other with a force of gravitational attraction.

In this paper an assembly sequence planning problem is solved using a GSA-based approach. The objective is to generate the optimal assembly sequence to minimize production time. At the same time, production cost can be save.

2. Gravitational Search Algorithm

The computational of GSA requires a set of N agents, which are randomly positioned in the search space during the initialization. The position of agents, which are the candidate solutions to the problem are represented as:

$$X_i = (x_i(1), \dots, x_i(d), \dots, x_i(n)) \text{ for } i = 1, 2, 3, \dots, N \quad (1)$$

where $x_i(d)$ presents the position of i^{th} agent in the d^{th} dimension, and n is the space dimension.

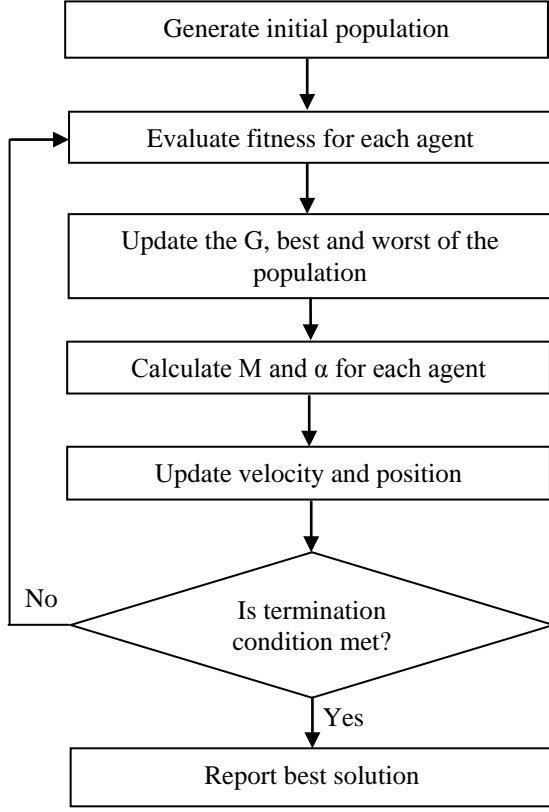


Fig. 1. General principle of GSA.

Figure 1 portrays the principle of GSA. Initially, all agents are assigned with velocity $v_i(t, d)$ that is equal to zero where t represents the iteration number. Next, the fitness of agent i at time t , $fit_i(t)$ for each agent is evaluated with respect to $x_i(t, d)$. The gravitational constant $G(t)$ is then updated using:

$$G(t) = G_0 e^{-\frac{\beta t}{T}} \quad (2)$$

where T is the number of maximum iteration, G_0 and β are constant values. The gravitational constant is a decreasing function of time where it is valued to G_0 at the beginning and it is exponentially decreased towards zero as the iteration increases to control the search accuracy. Next, $best(t)$ and $worst(t)$ are calculated. For minimization problem, the definition of $best(t)$ and $worst(t)$ are given as follows:

$$best(t) = \min_{j \in \{1, \dots, N\}} fit_j(t) \quad (3)$$

$$worst(t) = \max_{j \in \{1, \dots, N\}} fit_j(t) \quad (4)$$

For a maximization problem, the definition of $best(t)$ and $worst(t)$ are changed to:

$$best(t) = \max_{j \in \{1, \dots, N\}} fit_j(t) \quad (5)$$

$$worst(t) = \min_{j \in \{1, \dots, N\}} fit_j(t) \quad (6)$$

The gravitational and inertial mass are then updated as:

$$m_i(t) = \frac{fit_i(t) - worst(t)}{best(t) - worst(t)} \quad (7)$$

$$M_i(t) = \frac{m_i(t)}{\sum_{j=1}^N m_j(t)} \quad (8)$$

where $M_i(t)$ is the inertial mass of i^{th} agent. The acceleration, α , of mass i in time t in the d^{th} dimension is calculated as:

$$\alpha_i(t, d) = \frac{F_i(t, d)}{M_i(t)} \quad (9)$$

where the force acting $F_i(t, d)$ is calculated as:

$$F_i(t, d) = \sum_{j=1, j \neq i}^N rand_j F_{ij}(t, d) \quad (10)$$

$$F_{ij}(t, d) = G(t) \frac{M_i(t)}{R_{ij}(t) + \varepsilon} (x_j(t, d) - x_i(t, d)) \quad (11)$$

where ε is a small constant, $R_{ij}(t)$ is the Euclidean distance between agent i and j , and $rand_j$ is a random number uniformly distributed between 0 and 1. Then, the velocity and position of agent's are updated respectively as:

$$v_i(t+1, d) = rand_i \times v_i(t, d) + \alpha_i(t, d) \quad (12)$$

$$x_i(t+1, d) = x_i(t, d) + v_i(t+1, d) \quad (13)$$

where $rand_i$ is random number uniformly distributed between 0 and 1. The algorithm iterates until the stopping condition is met, either the maximum number of iteration is reached or a particular amount of error is obtained.

3. Mathematical Model

The main objective of assembly sequence planning is to generate feasible assembly sequences which takes less time to be assembled, thereby reduces assembly costs. The most important factor in reducing assembly time and costs are setup time, including transfer time, number of tool changes, and proper fixture selection.

In this study, assumptions for assembly sequence planning are as follows;

1. Setup time and the actual assembly time for each part and component are given.
2. Transfer time between workstations is included in set up time.
3. Downtime of machines and workstations is omitted.

3.1 Minimization of Assembly Time

The total assembly time is the combination of setup time and actual assembly time. It is assumed that regardless of the assembly sequence, the actual assembly time is constant. A proper tool and setup for each component to be assembled is required. These two items depend on the geometry of the component itself and the components assembled to that point. The setup time for a component can be predicted using the following function [5]:

$$Time_{Setup}(a) = p_{a0} + \sum_{b=1}^c p_{ab}q_{ab} \quad (14)$$

where (a) is the component to be assembled, p_{a0} is the setup time for product (a) being the first component, p_{ab} is the contribution to the setup time due to the presence of part (b) when entering part (a) , and $q_{ab} = 1$ if component (b) has already been assembled for $a = 1, \dots, c$. Otherwise, $q_{ab} = 0$ for $a = 1, \dots, c$ in which c is the number of components occurred in the assembly sequence planning.

The total assembly time is the summation of setup time and actual assembly time. Hence, the objective function for minimizing the assembly time is shown in the Eq. (15).

$$\text{Min } Time_{Assembly} = \sum_{a=1}^c (Time_{Setup}(a) + A_a) \quad (15)$$

where A_a is the assembly time for component a . The calculation of time is in time units.

3.1 Precedence Constraints

To obtain feasible assembly sequences, all assembly sequences produced must comply with all precedence constraints. One of the constraints of the assembly design is the precedence relationships between the components. In general, the determined input data required by the assembly process is readily extracted either from CAD or disassembly analysis.

A precedence matrix (PM) is used to show the relation using the precedence constraints between components in assembly. The relationship includes the nature of the connection (free to assembly components) and the relative assembly precedence between two components. Let say component a must be assembled after component b , which means $PM(p_a, p_b) = 1$. Otherwise $PM(p_a, p_b) = \emptyset$ where (p_a, p_b) is a pair of components that has a geometric information in which p_a must be assembled without

interfering with p_b . To decide which pair is feasible, precedence constraints for a product should be described using PM. Given ψ as the set of the components have been assembled before component a and the union of PM is a feasible assembly sequence FAS (p_a, p_b) with constraints. Therefore,

$$FAS(P_a, P_b) = \square PM(P_a, P_b), P_b \square \psi \quad (16)$$

The generation of feasible assembly sequences is explained in [6] for details.

4. Gravitational Search Algorithm (GSA) for Assembly Sequence Planning

In order to find an optimal solution, each agent representing feasible assembly sequence must be evaluated to obtain its fitness value. This evaluation of the fitness value is done after generating initial population and loading precedence matrix (PM), coefficient table and actual assembly time.

The PM and coefficient table can be referred in [5] for details. Figure 2 shows the precedence diagram of the case study. It is worth pointing out that the components of free to be assembled are the components that can be placed regardless of any part of a sequence. These three processes and are other processes of the proposed approach using GSA are provided as following:

1. Generate initial population of N agents randomly
2. Load precedence matrix, coefficient table and actual assembly time
3. For each agent i , do:
 - (a) Evaluate fitness;
 - (b) Update the G, best and worst of the population
 - (c) Evaluate mass;
 - (d) Evaluate force of mass;
 - (e) Evaluate acceleration of mass;
 - (f) Update velocity and position of mass;
 - (g) Evolve the updated assembly sequence of agent i with respect to the updated position of feasible assembly sequence
4. If termination condition is not met, Go To 2 Else Report best solution

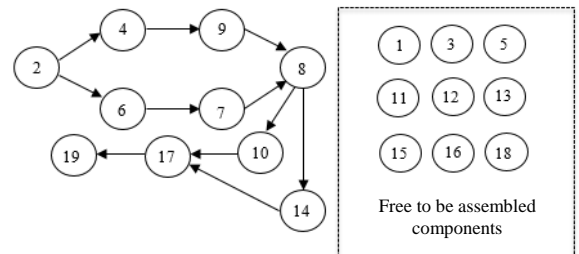


Fig. 2. The assembly precedence diagram of case study.

5. Experimental Results

To evaluate the proposed approach, we conducted a few sets of experiments on the similar case study to compare our approach with several approaches using SA [4], GA [5], and Binary PSO (BPSO) [6]. Due to the discrepancy of the experimental setting used in the above algorithms, the performance comparisons were arranged and operated in a peer-to-peer manner. It needs to be mentioned that in order to examine the generality of the proposed approach, we have used the same settings as that of the algorithms to be compared, though those settings were best-fitted to the individual work but not specifically suitable for ours.

In this study, MATLAB R2013a was used as a platform to solve the ASP problem. Personal computers with Intel® Core™ i5-2450M CPU 2.50 GHz was used to run experiments. The quality of results of the proposed GSA-based approach is measured based on the fitness values of the best solutions in minimizing the total assembly time. For instance, if the number of independent trials on the case study is 50, the quality of results is determined based on the fitness values of 50 solutions. To simplify the understanding of this work, fitness or objective value and solution is now called total assembly time and feasible assembly sequence, respectively.

5.1 Result of the proposed GSA-based approach against the SA-based approach

All the parameters of the proposed GSA-based approach against the SA-based approach are listed in Table 1. It is observed that the assembly sequence planning and optimization can be performed with both approaches. As seen in Table 2, the performance of the proposed GSA-based approach is better than the SA-based approach due to faster total assembly time recorded based on minimum value of all total assembly time.

5.2 Result of the proposed GSA-based approach against the GA-based approach

Parameters of these two approaches are demonstrated in Table 3. Similarly, these two approaches can be used to find assembly sequences. The performance of the proposed GSA-based approach and the GA-based approach is compared in Table 4. It is clearly indicated that the proposed GSA-based approach offers better performance than the SA-based approach in minimizing total assembly time.

5.3 Result of the proposed GSA-based approach against the BPSO-based approach

Parameters and the comparison between the proposed GSA-based approach and the BPSO-based approach are provided in Table 5 and Table 6 respectively. These two approaches successfully yield a comparative result in which the proposed GSA-based approach is better than the BPSO-based approach in minimizing total assembly time.

Table 1 The parameters for the proposed GSA-based approach and the SA-based approach in experiment.

Experimental parameters	GSA	SA
Iteration	500	500
Size of population	30	-
G_0	100	-
β	20	-
Initial temperature (°C)	-	100
Cooling rate	-	0.95
Number of run	50	-

Table 2 The best result and assembly sequence of the proposed GSA-based approach and the SA-based approach.

Approach based	Total assembly time	Assembly sequence
GSA	511.6	2-1-4-9-3-12-15-5-18-13-6-16-11-7-8-10-14-17-19
SA	528.7	2-1-4-9-3-12-13-16-5-15-18-6-11-7-8-10-14-17-19

Table 3 The parameters for the proposed GSA-based approach and the GA-based approach in experiment.

Experimental parameters	GSA	GA
Iteration	100	100
Size of population	100	100
G_0	100	-
β	20	-
Mutation rate	-	0.05
Crossover	-	0.50
Number of run	50	-

Table 4 The best result and assembly sequence of the proposed GSA-based approach and the GA-based approach.

Approach based	Total assembly time	Assembly sequence
GSA	512.0	2-15-1-4-3-12-13-11-9-16-5-18-6-7-8-10-14-17-19
GA	524.1	2-18-3-12-1-13-16-5-11-15-4-6-9-7-8-10-14-17-19

Table 5 The parameters for the proposed GSA-based approach and the BPSO-based approach in experiment.

Experimental parameters	GSA	BPSO
Iteration	500	500
Size of population	40	40
G_0	100	-
β	20	-
Inertia weight, ω	-	0.6
Learning factor, c_1 and c_2	-	1.42
Number of run	10	10

Table 6 The best result and assembly sequence of the proposed GSA-based approach and the BPSO-based approach.

Approach based	Total assembly time	Assembly sequence
GSA	514.0	1-3-2-4-12-9-13-5-15-18-16 -11-6-7-8-10-14-17-19
BPSO	514.4	16-2-13-4-1-15-11-9-6-5-18 -7-8-14-12-10-3-17-19

6. Conclusion

In this study gravitational search algorithm approach is proposed to generate and optimize assembly sequences. The precedence diagram and the precedence matrix are employed to denote the feasible order of components of the assembly. The work represents an assembly sequence as an agent designated by a character string and subsequently, the position of new agents are generated through measuring the velocity of each agent per iteration. Gravitational search algorithm stops when the termination criterion is reached. To evaluate the performance of the proposed approach, a case study of ASP consisting nineteen components is chosen, and the performance of the proposed approach using gravitational search algorithm is evaluated against three different approaches that uses simulated annealing, genetic algorithm, and binary particle swarm optimization respectively. Experimental results obtained showed that the proposed approach using gravitational search algorithm can effectively generate feasible assembly sequences with minimum production time. In future we may examine the performance of this approach on other case studies of assembly sequence planning that having many sub-assemblies constraints.

Acknowledgement

Authors want to acknowledge the support given by Ministry of Education Malaysia through the projects Fundamental Research Grant Scheme VOT 4F331 and UM-UMRG Scheme (CG031-2013) granted by Universiti Teknologi Malaysia and Universiti Malaya respectively.

References

- [1] H. G. Lv and C. Lu, "An Assembly Sequence Planning Approach with a Discrete Particle Swarm Optimization Algorithm," *The International Journal of Advanced Manufacturing Technology*, Vol. 50, pp. 761–770, 2010.
- [2] W. Garrod and L. J. Everett, "A.S.A.P.: Automated Sequential Assembly Planner," *ASME International Computers in Engineering Conference*, pp. 139–150, 1990.
- [3] L. Laperriere and A. El Marghy, "Assembly Sequence Planning for Simultaneous Engineering," *The International Journal of Advanced Manufacturing Technology*, Vol. 9, pp. 231–244, 1994.
- [4] S. Motavalli and A. Islam, "Multi-Criteria Assembly Sequencing," *Computational Industrial Engineering*, Vol. 32, pp. 743–751, 1997.
- [5] Y-K. Choi, D. M. Lee and Y. B. Cho, "An Approach to Multi-Criteria Assembly Sequence Planning using Genetic Algorithms," *The International Journal of Advanced Manufacturing Technology*, Vol. 42, pp. 180–188, 2008.
- [6] J. A. A. Mukred, Z. Ibrahim, I. Ibrahim, A. Adam, K. Wan, Z. Md. Yusof and N. Mokhtar, "A Binary Particle Swarm Optimization Approach to Optimize Assembly Sequence Planning," *Advanced Science Letter*, Vol. 13, pp. 732–738, 2012.
- [7] C. Blum and A. Roli, "Metaheuristics in Combinatorial Optimization: Overview and Conceptual Comparison," *ACM Computing Surveys*, Vol. 35, pp. 268–308, 2003.
- [8] E. G. Talbi, *Metaheuristics: From Design to Implementation*, John Wiley & Sons, New Jersey, 2009.
- [9] E. Rashedi and S. Saryazdi, "GSA: A Gravitational Search Algorithm," *Information Sciences*, Vol. 179, pp. 2232–2248, 2009.

An Approach to Reduce Computational Cost for Localization Problem

Nur Aqilah Othman and Hamzah Ahmad

Faculty of Electrical and Electronics Engineering, Universiti Malaysia Pahang, 26600 Pekan, Pahang, Malaysia

(E-mail: aqilah.hamzah@ump.edu.my)

Abstract – One of the biggest factors that contribute to the computational cost of extended Kalman filter-based SLAM is the covariance update. This is due to the multiplications of the covariance matrix with other parameters and the increment of its dimension, which is twice the number of landmarks. Therefore a study is conducted to find a possible technique to decrease the computational complexity of the covariance matrix without minimizing the accuracy of the state estimation. This paper presents a preliminary study on the matrix-diagonalization technique, which is applied to the covariance matrix in EKF-based SLAM to simplify the multiplication process. The behaviors of estimation and covariance are observed based on three case studies.

Keywords – covariance, diagonalization, extended Kalman filter, simultaneous localization and mapping.

1. Introduction

Simultaneous localization and mapping (SLAM) of a mobile robot is one of the navigation techniques which enable the robot to move autonomously in an unknown environment. SLAM does not require a priori map, but with the aid of exteroceptive and proprioceptive sensors on board, the mobile robot is able to incrementally build a feature map of the environment and use this map to localize its position. The position of mobile robot and landmarks are determined by means of estimation method such as the Kalman filter [1], the particle filter [2] or the H_∞ filter [3]. These methods provide estimations based on the measurement data that are recursively recorded by the sensors. SLAM has been applied in a wide range of mobile robot applications such as underwater, mining, space exploration and in home appliances [4-6].

Extended Kalman filter (EKF) has been widely used to solve the estimation problem in SLAM due to simplicity of the algorithm, its robustness and its ability to apply the algorithm online compared to other approaches such as particle filter. However, the whole covariance matrix in EKF-based SLAM needs to be updated each time a new landmark is detected. This process involves lots of mathematical operation, thus will increase the computational cost. Moreover the dimension of covariance matrix will increase to twice the number of landmark, as more landmarks are detected. The classical EKF-based SLAM algorithm is known to have a cost of

$O(m^2)$, in which m is a total landmark of the map. This limits the use of EKF in a large environment.

Therefore researchers have been trying to find the solution to minimize the computational cost by focusing on the simplification of the covariance structure. Guivant and Nebot [7] introduced a decorrelation algorithm to simplify the covariance matrix. The algorithm will decorrelate a subset of the states that is weakly correlated and cancel the weakly cross-correlation terms in the covariance matrix. A positive semi definite matrix is added to the covariance matrix to reduce both computational and storage costs in SLAM. However this technique has some drawbacks that lead to filter instability. For that reason the cross-correlation of the structure needs to be preserved [8, 9]. A Study has been conducted to improve the technique through diagonalization of only part of the state error covariance [10]. The technique is known as covariance inflation method, in which a pseudo-noise covariance is added to the covariance matrix to maintain the suboptimality of the filter, given that SLAM is considered as a partially observable system [11, 12]. Besides covariance inflation, Julier and Uhlmann introduced a covariance intersection method for SLAM, a fusion technique that combines two covariances when the correlations between them are unknown [13], and this technique has been implemented not only in SLAM, but also in other applications [14]. In this technique, the update process is carried out in two independent steps; updating the robot, then updating the landmark. However there exists a new parameter ω in the algorithm that needs to be chosen through an optimization process.

This preliminary study is conducted to find an alternative technique in diagonalizing the covariance matrix of EKF-based SLAM. As an initial approach, the matrix will be diagonalized using the technique of finding its eigenvalues and rebuilding a new diagonal-covariance from these values. The preliminary results of the effect on the estimation and covariance behavior are presented, which have been obtained through simulations.

This paper is structured as follows: the next section contains a brief explanation on the EKF-based SLAM models, diagonalization technique and the structure of covariance matrix. Section 3 explains the diagonalization process based on three case studies. The simulated results are presented and discussed in Section 4. Finally, the conclusion is drawn in Section 5.

2. Problem Formulation

Simultaneous Localization and Mapping process in a mobile robot is defined through discrete time dynamical system equation using process and observation model. Extended Kalman filter is used to estimate the position of the mobile robot and landmarks. In this section, the formulation of the SLAM process and estimation through extended Kalman filter are explained. Moreover, the technique of matrix diagonalization that will be implemented on the covariance matrix is discussed.

2.1 Model of Simultaneous Localization and Mapping (SLAM)

The process model in SLAM describes the kinematics and movements of a mobile robot. The mobile robot moves within the environment and measures its relative distance to the existing landmarks using sensors. The measurement process is represented using the observation model.

The process model of SLAM at time $k+1$ is described as a function of state vector X_k , control input u_k and process noise w_k evaluated at time k , as follows:

$$X_{k+1} = f(X_k, u_k, w_k, k) \quad (1)$$

The state vector of a 2D SLAM $X_k \in \mathbb{R}^{3+2m}$ is a joint state-vector of robot position X_r and position of landmark X_m

$$X_k = [X_r \quad X_m]^T \quad (2)$$

where position of mobile robot $X_r = [\theta_k \quad x_k^r \quad y_k^r]^T$ is represented in terms of the robot heading angle θ_k and the coordinates of the center of mobile robot with respect to global coordinate frame (x_k^r, y_k^r) . The landmarks are modeled as point landmarks and described by Cartesian coordinate (x_i, y_i) , $i = 1, 2, \dots, m$ where m refers to the number of landmarks in the environment.

The control input of the robot movement is designated by $u_k = [\gamma_k \quad \omega_k]^T$ where γ_k is the mobile robot angular acceleration and ω_k is its velocity with associated process noises, $\delta\gamma$ and $\delta\omega$. The process noise w_k is a zero-mean Gaussian noise of $\delta\gamma$ and $\delta\omega$ with covariance Q_k i.e. $w_k \sim N(0, Q_k)$. The mobile robot considered in this study is a two-wheel (uni-cycle) robot. Thus, the process model of this type of robot is defined as follows:

$$X_{r(k+1)} = \begin{bmatrix} \theta_{k+1} \\ x_{k+1}^r \\ y_{k+1}^r \end{bmatrix} = \begin{bmatrix} \theta_k + (\gamma_k + \delta\gamma)T \\ x_k^r + (\omega_k + \delta\omega)T \cos(\theta_k) \\ y_k^r + (\omega_k + \delta\omega)T \sin(\theta_k) \end{bmatrix} \quad (3)$$

where T is the sampling rate or time interval of one movement step.

In this study, landmarks are assumed to be stationary. Therefore process model for the landmarks at time $k+1$ is

$$X_{m(k+1)} = X_{m(k)} \quad (4)$$

The observation or measurement process performed by the mobile robot in SLAM is represented by an observation model. In mobile robot SLAM, the observation of i -th landmark possesses range and bearing readings, which indicate relative distance and relative angle of the mobile robot to any observed landmarks within the environment. It is assumed that the mobile robot is equipped with range and bearing sensors onboard and encoders at the wheels to measure its speed. Observation model of the mobile robot SLAM is defined as follows:

$$z_k = h(X_k, v_k, k) = \begin{bmatrix} r_i + v_r \\ \phi_i + v_\phi \end{bmatrix} = \begin{bmatrix} \sqrt{(x_i - x_k^r)^2 + (y_i - y_k^r)^2} + v_r \\ \tan^{-1}\left(\frac{y_i - y_k^r}{x_i - x_k^r}\right) - \theta_k + v_\phi \end{bmatrix} \quad (5)$$

where $v_k = [v_r \quad v_\phi]^T$ is the zero-mean Gaussian observation noise applied to range and bearing observations with covariance R_k i.e. $v_k \sim N(0, R_k)$. Process and observation models of mobile robot SLAM are illustrated in Fig. 1.

2.2 Simultaneous Localization and Mapping by means of EKF

The position of mobile robot and landmarks are estimated using extended Kalman filter (EKF). The state vector is predicted based on the system's previous information, which then is estimated based on the measurement data obtained from the sensors. EKF

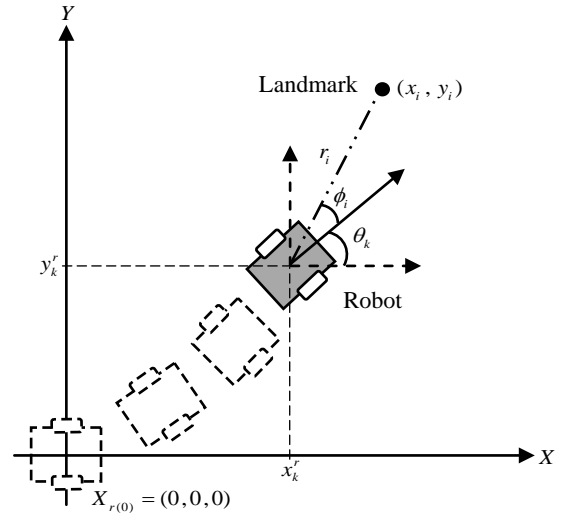


Fig. 1. The process and observation models of mobile robot SLAM.

provides the mean that indicates the updated state vector \hat{X}_k , and the covariance matrix of the estimation P_k that designates the estimation error. The prediction and estimation steps of EKF are described as follows:

A. Prediction (time update)

At time k the estimation of the state vector is

$$\hat{X}_k = [\hat{X}_r \quad \hat{X}_1 \quad \hat{X}_2 \quad \cdots \quad \hat{X}_m]^T \quad (6)$$

and covariance matrix of the estimation error is P_k . The process model (Eq. (1) – (4)) are linearized as a Taylor series expansion about \hat{X}_k and thus leads to the following predicted state vector \hat{X}_{k+1}^- and error covariance matrix P_{k+1}^-

$$\hat{X}_{k+1}^- = f(\hat{X}_k, u_k, 0, k) \quad (7)$$

$$P_{k+1}^- = \nabla F_x P_k \nabla F_x^T + \nabla F_w Q_k \nabla F_w^T \quad (8)$$

where ∇F_x is the Jacobian of f with respect to X_k and ∇F_w is the Jacobian with respect to w_k . These Jacobians are evaluated from Eq. (3) at \hat{X}_k and possess following equations.

$$\nabla F_x = \begin{bmatrix} 1 & 0 & 0 & 0 \\ -\omega T \sin \hat{\theta}_k & 1 & 0 & 0 \\ \omega T \cos \hat{\theta}_k & 0 & 1 & 0 \\ 0 & 0 & 0 & I_m \end{bmatrix}, \quad \nabla F_w = \begin{bmatrix} \nabla f_{y\omega} \\ 0_m \end{bmatrix} \quad (9)$$

I_m and 0_m are the identity and null matrix respectively, with appropriate dimension, depending on the number of observed landmarks, while T is the sampling rate. Note that ∇F_w indicates that there is no process noise for the landmarks as they were assumed to be stationary at all times.

B. Update (measurement update)

The state vector and error covariance matrix equations in the update process are formed by linearizing the observation model (5) through Taylor series expansion about \hat{X}_{k+1}^- . With the availability of measurement data z_{k+1} , the mobile robot then updates its current position relative to the position of observed landmarks through

$$\hat{X}_{k+1}^+ = \hat{X}_{k+1}^- + K_{k+1} (z_{k+1} - h(\hat{X}_{k+1}^-, k)) \quad (10)$$

with the updated error covariance matrix

$$P_{k+1}^+ = P_{k+1}^- - K_{k+1} (\nabla H_i P_{k+1}^- \nabla H_i^T + R_k) K_{k+1}^T \quad (11)$$

where $n = 3 + 2m$, the dimension of state vector. K_{k+1} is a Kalman gain and has the following definition.

$$K_{k+1} = P_{k+1}^- \nabla H_i^T (\nabla H_i P_{k+1}^- \nabla H_i^T + R_k)^{-1} \quad (12)$$

∇H_i is the Jacobian of function h in (5) with respect to X_k evaluated at \hat{X}_{k+1}^- and has the following characteristics [15]

$$\nabla H_i = \begin{bmatrix} 0 & -\frac{dx}{r} & -\frac{dy}{r} & \frac{dx}{r} & \frac{dy}{r} \\ -1 & \frac{dy}{r^2} & -\frac{dx}{r^2} & -\frac{dy}{r^2} & \frac{dx}{r^2} \end{bmatrix} \quad (13)$$

with

$$dx = \hat{x}_i^- - \hat{x}_{k+1}^{r-}, \quad dy = \hat{y}_i^- - \hat{y}_{k+1}^{r-}, \quad r = \sqrt{dx^2 + dy^2} \quad (14)$$

2.3 Diagonalization of Matrix

For a square matrix, the matrix might be diagonalized by finding its eigenvalues. Let A be a $n \times n$ matrix. Suppose there exists a number λ and a column matrix B with dimension of $n \times 1$ such that

$$AB = \lambda B \quad (15)$$

in which λ is said to be an eigenvalue of A with the corresponding eigenvector B . In general, for each $n \times n$ matrix, there will be normally n number of eigenvalues, in which the eigenvalues might be real, complex or combination of both numbers.

Definition 1: Let A be a $n \times n$ square matrix and D is a diagonal matrix in which its diagonal elements are the eigenvalues of A , such as follows:

$$D = \begin{bmatrix} \lambda_1 & 0 & 0 & 0 \\ 0 & \lambda_2 & 0 & 0 \\ 0 & 0 & \ddots & 0 \\ 0 & 0 & 0 & \lambda_n \end{bmatrix} \quad (16)$$

Therefore, there exists the following relationship between matrix A and matrix D :

$$\det(A) = \det(D) \quad (17)$$

$$\text{norm}(A) = \text{norm}(D)$$

2.4 Structure of Error Covariance Matrix

The covariance matrix of a state estimation in SLAM is a combination matrix of mobile robot and landmark position covariance matrixes and correlation between mobile robot and landmarks. Correlations between mobile robot position and landmarks estimation arise when the measurements are incorporated and thus, the state error covariance becomes dense. The state error covariance P_k is defined generally as

$$P_k = \begin{bmatrix} P_{rr} & P_{rm} \\ P_{rm}^T & P_{mm} \end{bmatrix} \quad (18)$$

with

- P_{rr} : Covariance matrix of the robot position.
- P_{mm} : Covariance matrix of the landmark position.

P_{rm} : Cross-covariance matrix of the robot and landmark position or cross-correlation.

The dimension of state error covariance in SLAM is $(3+2m) \times (3+2m)$. The size of covariance matrix will grow as the robot continuously observed new landmarks in the environment. State error covariance for SLAM is fully represented in the following equation:

$$\begin{bmatrix} P_{\theta\theta} & P_{\theta x} & P_{\theta y} & P_{\theta m_{1,x}} & P_{\theta m_{1,y}} & \dots & P_{\theta m_{n,x}} & P_{\theta m_{n,y}} \\ P_{x\theta} & P_{xx} & P_{xy} & P_{xm_{1,x}} & P_{xm_{1,y}} & \dots & P_{xm_{n,x}} & P_{xm_{n,y}} \\ P_{y\theta} & P_{yx} & P_{yy} & P_{ym_{1,x}} & P_{ym_{1,y}} & \dots & P_{ym_{n,x}} & P_{ym_{n,y}} \\ P_{m_{1,x}\theta} & P_{m_{1,x}x} & P_{m_{1,x}y} & P_{m_{1,x}m_{1,x}} & P_{m_{1,x}m_{1,y}} & \dots & P_{m_{1,x}m_{n,x}} & P_{m_{1,x}m_{n,y}} \\ P_{m_{1,y}\theta} & P_{m_{1,y}x} & P_{m_{1,y}y} & P_{m_{1,y}m_{1,x}} & P_{m_{1,y}m_{1,y}} & \dots & P_{m_{1,y}m_{n,x}} & P_{m_{1,y}m_{n,y}} \\ \vdots & \vdots & \vdots & \vdots & \vdots & \dots & \vdots & \vdots \\ \vdots & \vdots & \vdots & \vdots & \vdots & \dots & \vdots & \vdots \\ P_{m_{n,x}\theta} & P_{m_{n,x}x} & P_{m_{n,x}y} & P_{m_{n,x}m_{1,x}} & P_{m_{n,x}m_{1,y}} & \dots & P_{m_{n,x}m_{n,x}} & P_{m_{n,x}m_{n,y}} \\ P_{m_{n,y}\theta} & P_{m_{n,y}x} & P_{m_{n,y}y} & P_{m_{n,y}m_{1,x}} & P_{m_{n,y}m_{1,y}} & \dots & P_{m_{n,y}m_{n,x}} & P_{m_{n,y}m_{n,y}} \end{bmatrix} \quad (19)$$

Proposition 1: The determinant of the error covariance matrix is a measure of the volume of the uncertainty ellipsoid associated with the state estimate, which indicates the total uncertainty of that particular state estimation [1].

Therefore by referring to *Proposition 1* and the behaviour of diagonal matrix indicates by Eq. (17), it is believed that the diagonalization through the eigenvalues can be one of alternative technique to minimize the computational cost of EKF-based SLAM.

3. Diagonalization of Covariance Matrix in EKF-based SLAM

This pilot study attempts to investigate the effect of diagonalization of covariance matrix on the estimation performance and the covariance behavior through simulation analysis. The objective is to simplify the multiplication steps in the covariance calculation, in order to minimize the computational complexity as well as computational cost. Multiplication of a matrix with another diagonal matrix is much easier and faster since only diagonal elements are incorporated. The analysis is conducted base on three case studies:

- 1) Predicted covariance for both (robot and landmark) is diagonalized.

Algorithm 1: Diagonalization of predicted covariance matrix

```
Diagonalize_predicted_all ( $\hat{X}_k, P_k, u_k, z_k$ )
compute predicted state  $\hat{X}_{k+1}^-$ 
compute predicted covariance  $P_{k+1}^-$ 
find eigenvalues  $\lambda_n = eig(P_{k+1}^-)$ 
build diagonal matrix  $P_{(D),k+1}^- = diag(\lambda_n)$ 
compute predicted measurement  $h(\hat{X}_{k+1}^-, k)$ 
compute estimated state  $\hat{X}_{k+1}^+$ 
compute Kalman gain  $K_{k+1}$ 
compute estimated covariance  $P_{k+1}^+$ 
return  $\hat{X}_{k+1}^+, P_{k+1}^+$ 
```

- 2) Estimated covariance for both (robot and landmark) is diagonalized.
- 3) Only estimated covariance of landmark is diagonalized.

3.1 Full Diagonalization of Covariance Matrix

Equation (19) is fully diagonalized by finding the eigenvalues for the whole covariance values. Then the eigenvalues are collected and new diagonal covariance matrix is build using these values. Algorithm 1 and Algorithm 2 describe the diagonalization steps of the first and second case studies. Therefore the new diagonal covariance matrix has the following structure:

$$P_{(D),k+1} = \begin{bmatrix} \lambda_1 & 0 & 0 & 0 & 0 \\ 0 & \lambda_2 & 0 & 0 & 0 \\ 0 & 0 & \lambda_3 & 0 & 0 \\ 0 & 0 & 0 & \ddots & 0 \\ 0 & 0 & 0 & 0 & \lambda_n \end{bmatrix} \quad (20)$$

By using this new covariance matrix, multiplication process in Eq. (8) and Eq. (11) will be simplified and therefore reduce the computational cost.

3.2 Partial Diagonalization of Covariance Matrix

In SLAM, it is important for the mobile robot to have the knowledge of its current position. Initially the mobile robot needs to locate itself before sensing the landmark in the environment. Thus, it is important to retain the covariance of mobile robot P_{rr} as precise as possible. Under third case study, only the covariance of landmark P_{mm} is diagonalized through Algorithm 3. Hence the estimated covariance matrix for the third case study has the structure as indicates in Eq. (21).

4. Simulation Results and Discussions

The simulation analyses of the proposed case studies are conducted and the behavior of the estimation and covariance matrix are analyzed in this section.

Figure 2 shows the estimation of the mobile robot's position and landmarks' position under normal condition,

Algorithm 2: Diagonalization of estimated covariance matrix

```
Diagonalize_estimated_all ( $\hat{X}_k, P_k, u_k, z_k$ )
compute predicted state  $\hat{X}_{k+1}^-$ 
compute predicted covariance  $P_{k+1}^-$ 
compute predicted measurement  $h(\hat{X}_{k+1}^-, k)$ 
compute estimated state  $\hat{X}_{k+1}^+$ 
compute Kalman gain  $K_{k+1}$ 
compute estimated covariance  $P_{k+1}^+$ 
find eigenvalues  $\lambda_n = eig(P_{k+1}^+)$ 
build diagonal matrix  $P_{(D),k+1}^+ = diag(\lambda_n)$ 
return  $\hat{X}_{k+1}^+, P_{(D),k+1}^+$ 
```

Algorithm 3: Diagonalization of estimated covariance matrix of the landmark position

```

Diagonalize_estimated_landmark ( $\hat{X}_k, P_k, u_k, z_k$ )
  compute predicted state  $\hat{X}_{k+1}^-$ 
  compute predicted covariance  $P_{k+1}^-$ 
  compute predicted measurement  $h(\hat{X}_{k+1}^-, k)$ 
  compute estimated state  $\hat{X}_{k+1}^+$ 
  compute Kalman gain  $K_{k+1}$ 
  compute estimated covariance  $P_{k+1}^+$ 
  find eigenvalues of  $P_{(mm),k+1}^+$ 
   $\lambda_n = \text{eig}(P_{k+1}^+(4:\text{end}, 4:\text{end}))$ 
  build diagonal matrix  $P_{(mm,D),k+1}^+ = \text{diag}(\lambda_n)$ 
  build new diagonal matrix
   $P_{(D),k+1}^+ = \begin{bmatrix} P_{k+1}^+(1:3, 1:3) & P_{k+1}^+(1:3, 4:\text{end}) \\ P_{k+1}^+(4:\text{end}, 1:3) & P_{(mm,D),k+1}^+ \end{bmatrix}$ 
  return  $\hat{X}_{k+1}^+, P_{(D),k+1}^+$ 

```

(i.e. using normal covariance matrix). The mobile robot moves for $k = 1000$ s and continuously observes the landmarks for every cycle of movement. The covariance-ellipses indicate the uncertainties of the estimation. The smaller the ellipse, the better the estimation.

Using the same simulation parameters, simulations for the three case studies are conducted. Figure 3 depicts the estimation and covariance behavior of the first case study, while the result from the second case study can be seen in Fig. 4. As we can see from both figures, the estimation of mobile robot and landmark position is possible when the whole covariance is diagonalized through the technique defined in previous section. However the estimation has some degree of errors, which however is consider as acceptable. Nonetheless, the covariance behaves abnormally in these cases, in which the covariance decrease drastically and too small compared to the true covariance as depicted in Fig. 2. This scenario describes an optimistic estimation [15]. Moreover, Table 1 shows the comparison of processing time for all conditions. It clearly shows that the times taken to complete the SLAM process for the first and second case study are comparable

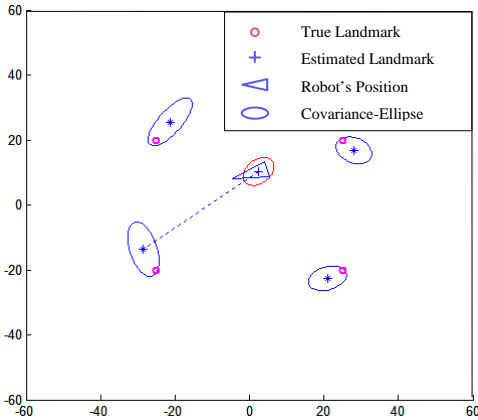


Fig. 2. Position estimation and covariance under normal condition.

$$P_{(D),k+1} = \begin{bmatrix} P_{\theta\theta} & P_{\theta x} & P_{\theta y} & & & \\ P_{x\theta} & P_{xx} & P_{xy} & & P_{rm} & \\ P_{y\theta} & P_{yx} & P_{yy} & & & \\ & & & \lambda_1 & 0 & 0 & 0 & 0 \\ & & & 0 & \lambda_2 & 0 & 0 & 0 \\ & P_{rm}^T & & 0 & 0 & \lambda_3 & 0 & 0 \\ & & & 0 & 0 & 0 & \ddots & 0 \\ & & & 0 & 0 & 0 & 0 & \lambda_n \end{bmatrix} \quad (21)$$

Table 1 Processing time for all cases.

Covariance type	Simulation time [s]	Total processing time [s]
Normal	1000	103.570
Case 1	1000	104.382
Case 2	1000	102.844
Case 3	300	34.779

to that of the normal condition. Even though there are additional steps taken in diagonalizing the covariance matrix, the time taken for the whole process to be completed is faster. This can be proven by the time taken for the second case, which is shows lower than that of the normal condition. From the results, it can be suggested that the technique may be applied to the EKF-based SLAM, but it requires some modification with regards to the approach, for example, the robot covariance and the covariance of the landmark should be managed separately.

Figure 5 shows the result of the third case study, in which only the covariance of landmark is being diagonalized. It clearly shows that the mobile robot is unable to detect the landmarks and also unable to localize itself. As a result, mobile robot has been lost within the environment. Note that the scale of the environment has been enlarged and the landmarks are the same landmarks as in other case studies. Besides, the simulation is conducted only for 300s since the estimation is unsuccessful. Through the thorough analysis on the covariance values, it has been observed that the diagonal elements of the covariance under this condition are not able to fulfill the requirement of positive semi definite behavior. This misleading result is believed to occur due to the structure of the new covariance, Eq. (21) in which only the covariance of the landmarks is being diagonalized, whereas the cross-correlation terms are being ignored. The cross-correlation terms should be included in the diagonalization process since these terms are important in ensuring the best estimation performance [16, 17]. Therefore a new strategy needs to be proposed to fully diagonalize the covariance matrix by incorporating the cross-correlation terms.

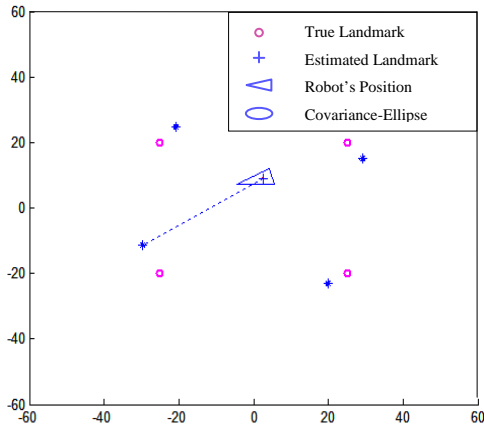


Fig. 3. State estimation and covariance for case one.

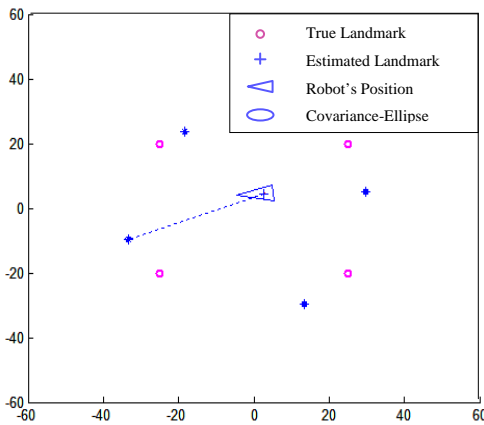


Fig. 4. Estimation of the state and covariance behavior of case two.

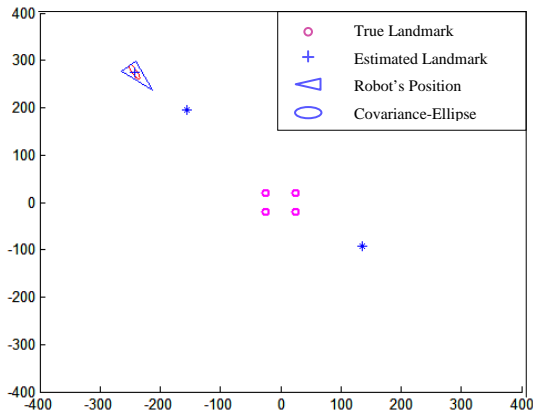


Fig. 5. Erroneous state and covariance estimation of case three.

5. Conclusion

This paper presents the analysis of EKF-based SLAM performance under the conditions of a diagonalized covariance. The covariance matrix needs to be simplified to reduce the computational complexity and thus reduce computational cost. Diagonalization method through eigenvalues could be one of the alternatives to achieve this goal. The simulation results have proven that this technique could be implemented, however more

modification on the algorithm should be done to ensure the estimation and covariance behavior are correct. Besides, the cross-correlation terms should be taken into account since it is important for the estimation accuracy. As for the future study, we are trying to analyze the behavior of each elements of covariance matrix in order to define the specific pattern for the development of an algorithm for a successful diagonal covariance matrix.

References

- [1] M.W.M.G. Dissanayake, P. Newman, S. Clark, H.F. Durrant-Whyte, and M. Csorba, "A Solution to the Simultaneous Localization and Map Building (SLAM) Problem", *IEEE Transactions on Robotics and Automation*, Vol. 17, No. 3, pp. 229-241, 2001.
- [2] M. Montemerlo, S. Thrun, D. Koller, and B. Wegbreit, "FastSLAM: A Factored Solution to the Simultaneous Localization and Mapping Problem", in *Proceedings of the In Proceedings of the AAAI National Conference on Artificial Intelligence*, pp. 593-598, 2002.
- [3] H. Ahmad and T. Namerikawa, "Robotic Mapping and Localization Considering Unknown Noise Statistics", *Journal of System Design and Dynamics*, Vol. 5, No. 1, pp. 70-82, 2011.
- [4] S. Lee, S. Lee, and S. Baek, "Vision-Based Kidnap Recovery with SLAM for Home Cleaning Robots", *Journal of Intelligent & Robotic Systems*, Vol. 67, No. 1, pp. 7-24, 2012.
- [5] H. Wang, G. Fu, J. Li, Z. Yan, and X. Bian, "An Adaptive UKF Based SLAM Method for Unmanned Underwater Vehicle", *Mathematical Problems in Engineering*, 12 Pages, 2013.
- [6] R. Zlot and M. Bosse, "Efficient Large-Scale 3D Mobile Mapping and Surface Reconstruction of an Underground Mine", in *Proceedings of the Field and Service Robotics*, pp. 479-493, January 2014.
- [7] J.E. Guivant and E.M. Nebot, "Solving Computational and Memory Requirements of Feature-Based Simultaneous Localization and Mapping Algorithms", *IEEE Transactions on Robotics and Automation*, Vol. 19, No. 4, pp. 749-755, 2003.
- [8] S.J. Julier, "The Stability of Covariance Inflation Methods for SLAM", in *Proceedings of the IEEE/RSJ International Conference on Intelligent Robots and Systems*, pp. 2749-2754, October 2003.
- [9] J.A. Cetto, T.A.V. Calleja, and A. Sanfeliu, *Stochastic State Estimation for Simultaneous Localization and Map Building in Mobile Robotics*, in *Cutting Edge Robotics*, Pro Literatur Verlag (InTech), 2005.
- [10] T. Vidal-Calleja, J. Andrade-Cetto, and A. Sanfeliu, "Conditions for Suboptimal Filter Stability in SLAM", in *Proceedings of the 2004 IEEE/RSJ International Conference on Intelligent Robots and Systems*, pp. 27-32, September 2004.
- [11] J. Andrade-Cetto and A. Sanfeliu, "The Effects of Partial Observability in SLAM", in *Proceedings of*

- the 2004 IEEE International Conference on Robotics and Automation, pp. 397-402, April 2004.
- [12] H. Ahmad, N.A. Othman, S. Razali, and M.R. Mohamed, "Analyzing the Mobile Robot Localization Performance in Partially Observable Conditions", in Proceedings of the 2014 IEEE Symposium on Industrial Electronics and Applications, pp. 210-215, September 2014.
- [13] S.J. Julier and J.K. Uhlmann, "Using Covariance Intersection for SLAM", Robotics and Autonomous Systems, Vol. 55, No. 1, pp. 3-20, 2007.
- [14] Y. Jiang and J. Xiao, "Target Tracking Based on a Multi-Sensor Covariance Intersection Fusion Kalman Filter", Engineering Review, Vol. 34, No. 1, pp. 47-54, 2014.
- [15] S. Huang and G. Dissanayake, "Convergence and Consistency Analysis for Extended Kalman Filter Based SLAM", IEEE Transactions on Robotics, Vol. 23, No. 5, pp. 1036-1049, 2007.
- [16] J.A. Castellanos, J.D. Tardos, and G. Schmidt, "Building a Global Map of the Environment of a Mobile Robot: The Importance of Correlations", in Proceedings of the IEEE International Conference on Robotics and Automation, pp. 1053-1059, April 1997.
- [17] H. Ahmad, N.A. Othman, and S. Razali, "The Importance of Cross-Correlation and its Effect to Mobile Robot Localization", in Proceedings of the 2013 2nd International Conference on Electrical, Control and Computer Engineering, pp. 257-262, August 2013.

Comparison of Manually-Designed and Automatically-Evolved Hybrid Articulated-Wheeled Robot

S. H. Lim and J. Teo

Evolutionary Computing Laboratory, Faculty of Computing and Informatics, Universiti Malaysia Sabah, Kota Kinabalu, 88450, Malaysia.

(E-mail: ¹eohnuhs@outlook.com, ²jtwtteo@ums.edu.my)

Abstract – Hybrid platform which combines wheeled and legged locomotion has excellent maneuverability on flat ground and uneven terrain. However, the extremely complexity in the kinematic and controller designing of a hybrid mobile robot has always been the biggest challenge for the researchers. The use of artificial evolution for the automatic generation and synthesis of controllers and/or morphologies for robots is one of the more recent methods in developing robots. This paper presents the comparison of a manually designed six articulated-wheeled robot (SAWR) and an optimized SAWR. The optimized SAWR is obtained from the optimal Pareto-set solutions of a multi-objective evolution process. Comparison shows that the optimized SAWR is outstanding of a manually designed SAWR in terms of the size and also the performance.

Keywords – Hybrid mobile robots, Evolutionary robotics, Multi-objective evolution, Optimized hybrid robot.

1. Introduction

In pace with the development and advancement of science and technology, the field of robotics is also growing rapidly. Autonomous robots have been frequently utilized in factory operations and also for assisting human in daily activities. Besides that, robots are often being used to replace rescue personnel in urban search and rescue operation where the task environments are tremendously complex and hazardous. However, designing a robot is generally considered to be demanding, because the designer not only has to predict the interaction between the robot and its environment, but also has to deal with the ensuing problem [1].

Typical locomotion of mobile robots can be categorized into two categories which are leg and wheel/track locomotion. Legged robots have higher flexibility in adapting to unstructured environment which make it to perform better in traversing over rough terrain. However, in terms of load/weight ratio, energy efficiency and speed, wheeled robots are always more powerful than legged robots [2][3]. Additionally, wheeled robots have simpler controller and kinematic design comparing with legged robots. The limitations of wheeled robots are wheeled robots generally having problem in traversing over unstructured terrain i.e. with steps, obstacles, and discontinuous contact surface.

Here raises the idea of hybrid mobile robot where the advantages of both wheeled and legged robots can be exploited. Hybrid mobile robot integrates both leg and wheel locomotion into a single platform. Therefore, hybrid mobile robots can move with faster speed and yet have better maneuverability on unstructured terrain. Various successful hybrid mobile robots platform had been developed; for example, Sojourner and Rocky 7 Rover by NASA [4][5], bounding gait robot PAW by McGill University [6][7], Shrimp by Swiss Federal Institute of Technology Lausanne [8], Wheeleg by University of Catania [9], and etc.

EAs are stochastic optimization techniques based on the principles of natural evolution [10]. The definition of EAs can be usually found in the literature expressed in a technical language that uses terms such as genes, chromosomes, population, etc. The standpoint of EAs is essentially practical where it uses ideas from natural evolution in order to solve a certain problem.

Evolutionary Robotics (ER) refers to the field of automatic generation of controllers and/or morphologies of robots using artificial EAs. ER is inspired by the Darwinian principle of selective reproduction of the fittest, captured by EAs. IN ER, robots are considered as autonomous artificial organisms that develop their own control system and body configuration in close interaction with the environment without human intervention. Recently, ER has been showing a successful example in designing robots [11 - 13]. By implementing EAs in designing a robot, an optimized controller and/or morphologies can be obtained where at times, these evolved solutions might be beyond the designers' design capability [14].

In this paper, the comparison of a manually designed and an evolved six articulated-wheeled robot (SAWR) is presented.

2. SAWR Morphology and Controller Design

2.1 Morphology Design

The SAWR has six one degree-of-freedom (DOF) legs while each leg is attached with an active wheel. The SAWR traverses with wheel locomotion in order to achieve faster travelling speed. On the other hand, the SAWR is capable to perform climbing motion with the

support of one DOF leg in order to overcome obstacles and steps.

There are totally twelve actuators integrated into the SAWR where six for the legs and the other six for the wheels. Besides that, there are three ultrasonic rangefinders integrated where two at the front and one at the rare bottom of the SAWR which can be seen in Fig 1.

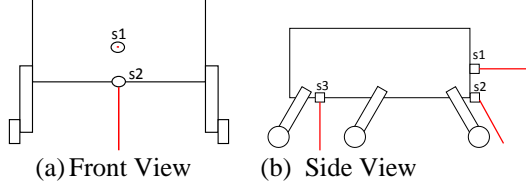


Fig. 1. Sensors placement on the SAWR. Sensors are represented by s1, s2 and s3 with the red lines are representing the direction of the sensors.

2.2 Controller Design

With three ultrasonic rangefinders and six active wheels, each attached on one DOF legs, the SAWR can perform a sequence of reconfiguration motions to climb over obstacles or steps.

The reconfiguration method of climbing upward and downward is originated from J.L. Lu et. al [15]. They had proposed a series of reconfiguration of a six legged-wheeled robot for ridges and channels negotiation. We integrate the proposed reconfiguration method into SAWR while enhancing the reconfiguration method to sensor-based. SAWR can perform climbing motion autonomously by referring to the changes of values from the ultrasonic rangefinders. The reconfiguration methods for climbing upward and downward of SAWR are shown in Fig. 2 and Fig. 3 accordingly.

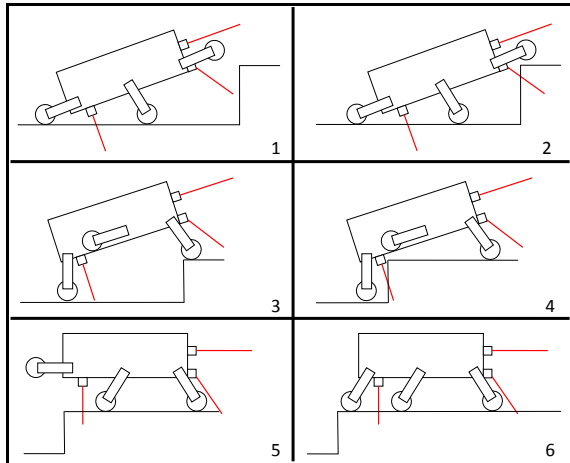


Fig. 2. Reconfiguration methods for climbing upward.

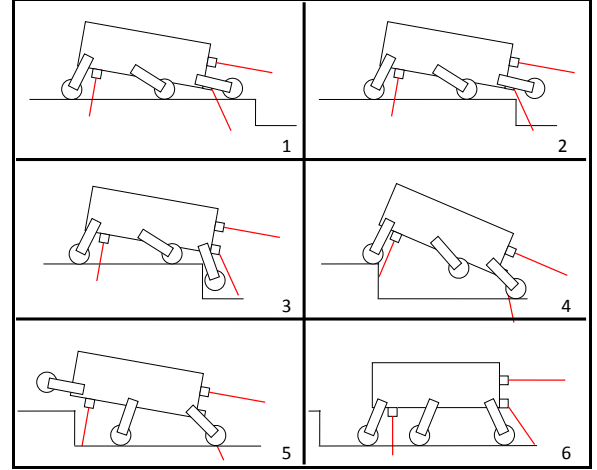


Fig. 3. Reconfiguration methods for climbing downward.

3. Simulation and Evolution Method

3.1 Multi-Objective Evolutionary Algorithm

In this paper, multi-objective evolutionary algorithm (MOEA) is employed to design and optimize a Pareto set SAWR. The first objective in this MOEA is to minimize the size of the SAWR morphology while the second objective is to optimize the performance of the climbing capability of the SAWR where both of the objectives are conflicting against each other.

$$\text{Size fitness} = b + l + r \quad (1)$$

b = robot body size;
 l = robot leg length;
 r = robot wheel radius.

$$\text{Performance fitness} = d^2 + c/mc + t/st \quad (2)$$

d = travelled distance from goal;
 c = number of collision;
 mc = maximum number of collision possible to occur in the simulation;
 t = time on reaching goal;
 st = simulation time.

There are two fitness functions in the MOEA which are shown in equation 1 and 2. The first fitness function is the size fitness function and the second fitness function is the performance fitness function. Both of the fitness functions are designed as in the smallest is the value, the better is the score. The size fitness function is built up with the summation of three parameters which are the body size of the robot, length of the robot legs and radius of the robot wheels. These are the three evolving and optimizing objects during the evolution process. While for the second fitness function, the fitness score of the performance of the robot during the simulation will be evaluated. The evaluated score is based on the degree of

perfection of the climbing motion and also the time consumption in reaching goal.

During the evolution process, non-dominated solutions/SAWRs which have either a better score of the size fitness or performance fitness will be saved into archive. Parent will be chosen randomly from the archive to generate new offspring by undergoing mutation. Mutation is carried out with the addition of a random Gaussian unit with the parents evolving objects parameter which are the radius of wheels, length of legs, and size of the robot body. The mutation processes are shown in equation 3, 4 and 5.

$$OR = PR + G \quad (3)$$

$$OL = PL + G \quad (4)$$

$$OB = PB + G \quad (5)$$

- G = Random Gaussian unit;
- PR = Parent's wheel radius;
- PL = Parent's Leg length;
- PB = Parent's body size;
- OR = Offspring wheel radius;
- OL = Offspring Leg length;
- OB = Offspring body size.

3.2 Simulation Setup

The evolution process takes place during the simulation in Webots. Webots is a development environment used to model, program and simulate mobile robots. With the high fidelity physical-based robot simulation, Webots have been widely used by researchers internationally, for example [16 - 19].

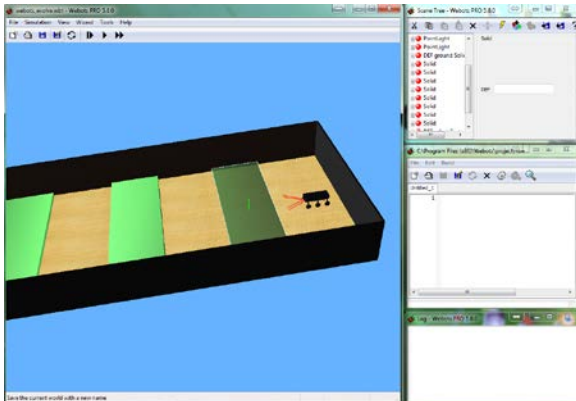


Fig. 4. Webots main window, scene tree, text editor and log window.

In the experiment, the task environment is designed as in fig. 5. There are total three obstacles in the environment which is to be climbed over by the SAWR. The first obstacle is a step with height 50mm, second obstacle is a step with height 70mm and the third obstacle

is a stair-like step with height 50mm for each steps. The robot will start moving forward from the right to left with climbing over all the obstacles in order to reach the goal destination.

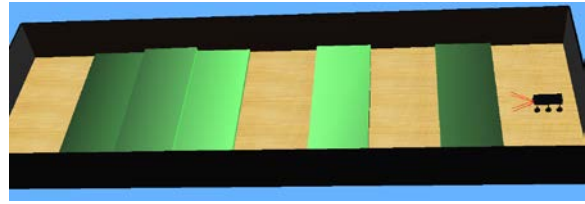


Fig. 5. Task environment setup for the evolution simulation.

The simulation time for each SAWR to reach the goal destination is 60 seconds. The maximum number of generation for this experiment is 500 where each generation has a population of 1 individual.

4. Results and Discussion

Before the simulation, a SAWR has been manually designed for testing with the climbing reconfiguration method. The hand design SAWR is shown in fig. 6 and its size fitness score and performance fitness score is shown in table 1.

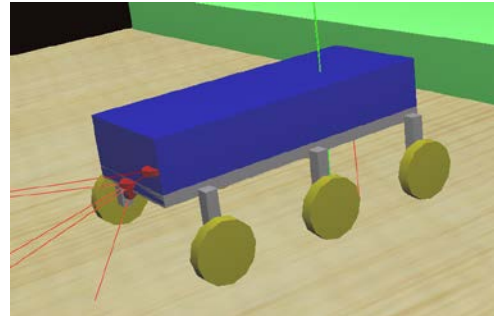


Fig. 6. The manually designed SAWR in Webots.

Table 1. Detailed information of size fitness and performance fitness of the manually designed SAWR.

Object	SAWR(manually designed)
Size Fitness	0.325
Wheel Radius (mm)	25
Leg Length (mm)	50
Body Size (mm)	250
Performance Fitness	0.661
Distance from Goal	0
Number of Collision	0
Time on Goal (seconds)	39.68

The manually designed SAWR has the size fitness score of 0.325 where the radius of wheels are 25mm, the length of legs are 50mm and the size of the body is 250mm. The performance fitness score of the manually designed SAWR is 0.661 where the manually designed SAWR manage to overcome all the obstacles without any collision and reach the goal destination. The time taken by the manually designed SAWR in reaching the goal destination is 39.68 seconds.

From the multi-objective evolution simulation, a Pareto-set of optimal solutions is obtained. The Pareto-set of optimal solutions are shown in fig. 7. The optimal Pareto-set solutions are SAWRs from smaller morphology with poor performance to bigger morphology with better performance which is represented by solution 1 to solution 5.

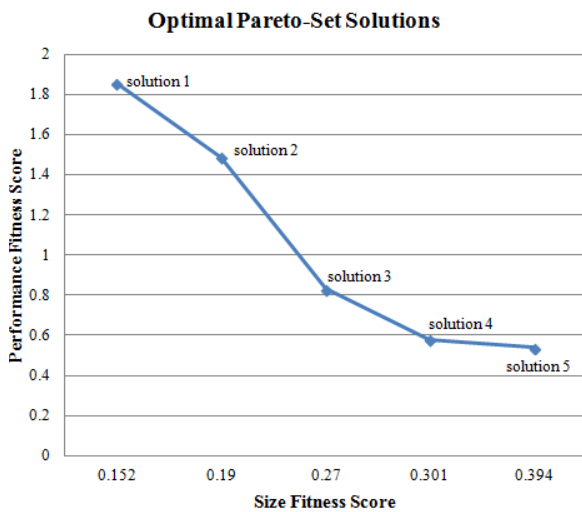


Fig. 7. Pareto-set of optimal solutions from the multi-objective evolution process.

One of the evolved solutions, solution 4 is outstanding in both size fitness and performance fitness if compared to the manually designed SAWR. The comparison of the evolved solution and the manually designed SAWR is shown in table 2.

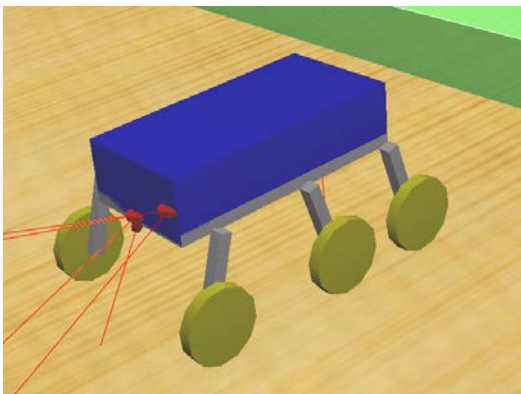


Fig. 8. SAWR (solution 4) obtained from the evolution process.

Table 2. Comparison of the manually designed SAWR and the evolved solution, solution 4.

Object	SAWR (manually designed)	Evolved solution (solution 4)
Size Fitness	0.325	0.301
Wheel Radius (mm)	25	30
Leg Length (mm)	50	69
Body Size (mm)	250	202
Performance Fitness	0.661	0.577
Distance from Goal	0	0
Number of Collision	0	0
Time on Goal (seconds)	39.68	34.62

From table 2, the evolved solution, solution 4 is smaller in size and yet has better performance fitness than the manually designed SAWR. Solution 4 has wheel radius of 30mm, leg length of 69mm and body size of 202mm as shown in fig. 8. Besides that, solution 4 is able to reach the goal destination with shorter time than the manually designed SAWR. The time taken for solution 4 in reaching the goal destination is 34.62 seconds while for the manually designed SAWR; the time taken is 39.68 seconds.

5. Conclusion and Future Work

The utilization of evolution approach in designing and optimizing the morphology of a SAWR is showing a success. Results show that the SAWR from the optimal Pareto-set solutions overpower a manually designed SAWR. The evolved SAWR is smaller than the manually designed SAWR and yet it is able to reach the goal destination in a shorter time. Besides that, the Pareto-set of optimal solutions provide user a choice of solutions for trade-off between the two objectives.

In current stage, only three parameters are involved in the evolution process which are the radius of wheels, length of legs and size of body. More parameters can be taken into consideration e.g. the placement of sensors and legs which can further improve the evolved solutions. Besides that, a co-evolution for both of the controller and morphology is intended to be investigated as a more comprehensive evolution process.

Acknowledgement

This work was funded under ScienceFund project SCF0085-ICT-2012 granted by the Ministry of Science, Technology and Innovation, Malaysia.

References

- [1] W. P. Lee, "An Evolutionary System for Automatic Robot Design", IEEE International Conference on Systems, Man, and Cybernetics, Vol 4, pp. 3477-3482, 1998.
- [2] J. Bojan, H. Martin, K. Michael, M. Erik, "Design of a Hybrid Wheeled-Legged Robot-Wheehy", IEEE, 2010.
- [3] C. H. Ong, H. M. Shamsudin, Amin, "A Biologically Inspired Hybrid Three Legged Mobile Robot", IEEE, 2002.
- [4] R. Volpe, J. Balaram, T. Ohm, R. Ivlev, "Rocky 7: A Next Generation Mars Rover Prototype", Advanced Robotics, 11, pp. 341-358, 1997.
- [5] S. Hayati, R. Volpe, P. Backes, J. Balaram, R. Welch, R. Ivlev, G. Tharp, S. Peters, T. Ohm, R. Petras, S. Laubach, "The Rocky 7 Rover: A Mars Sciencecraft Prototype", Proceedings of the 1997 IEEE International Conference on Robotics and Automation, New Mexico, USA, pp. 2458-2464, 1997.
- [6] J. A. Smith, I. Sharf, M. Trentini, "Bounding Gait in a Hybrid Wheeled-Leg Robot", Proceedings of the 2006 IEEE/RSJ International Conference on Intelligent Robots and Systems, Beijing, China, pp. 5750-5755, 2006.
- [7] J. A. Smith, I. Sharf, M. Trentini, "PAW: a Hybrid Wheeled-Leg Robot", Proceedings of the 2006 IEEE International Conference on Robotics and Automation, Orlando, Florida, pp. 4043-4048, 2006.
- [8] R. Siegwart, P. Lamon, T. Estier, M. Lauria, R. Piguet, "Innovative Design For Wheeled Locomotion in Rough Terrain", Robotics and Autonomous Systems, Vol 40, pp. 151-162, 2002.
- [9] M. Lacagnina, G. Muscato, R. Sinatra, "Kinematics, Dynamics and Control of a Hybrid Robot Wheeleg", Robotics and Autonomous Systems, Vol 45, pp. 161-180, 2003.
- [10] A. Enrique, C. Carlos, Evolutionary Algorithms, 2004.
- [11] L. Wang, K. C. Tan, C. M. Chew, "Evolutionary Robotics: From Algorithms to Implementations", World Scientific Publishing, 2006.
- [12] S. Nolfi, D. Floreano, "Evolutionary Robotics", MIT Press, 2000.
- [13] H. Iba, Frontiers in Evolutionary Robotics, I-Tech Education and Publishing, 2008.
- [14] S. H. Lim, J. Teo, "An Evolution Approach to Optimize the Morphology of a Six Legged-Wheeled Hybrid Mobile Robot", Proceedings of International Conference on Computational Science and Technology, 2014.
- [15] J. L. Lu, C. G. Bu, "Study on the Mobile Robot Reconfiguration Control Methods", International Conference on Automation and Logistics, pp. 2045-2049, 2009.
- [16] K. O. Chin, J. Teo, "Evolution and Analysis of Self-synthesized Minimalist Neural Controllers for Collective Robotics Using Pareto Multi-objective Optimization", IEEE Congress on Evolutionary Computation, 2010.
- [17] Y. Guo, S. Zhang, A. Ritter, H. Man, "A Case Study on a Capsule Robot in the Gastrointestinal Tract to Teach Robot Programming and Navigation", IEEE Transactions on Education, 2014.
- [18] A. Okan, A. H. Levent, "A Visual Compass for Robot Soccer", Signal Processing and Communication Applications Conference, 2014.
- [19] S. H. A. Mohammad, M. A. Jeffril, N. Shariff, "Mobile Robot Obstacle Avoidance by Using Fuzzy Logic Technique", IEEE International Conference on System Engineering and Technology, 2013.

Multiple Non-Identical Four DC Motor Synchronous Speed Control: Initial Hardware and Control Scheme

M.F.Abas¹, K.Balasubramaniam and N.Md.Saad

Robotics and Unmanned Systems (RUS) Group, Faculty of Electric and Electronics Engineering, Universiti Malaysia Pahang, Pekan, 26600, Pahang, Malaysia
(E-mail: mfadhil@ump.edu.my¹)

Abstract – This paper highlights the initial research in controlling speed of multiple DC motors synchronously. One of the motors tested for speed control are non-identical thus the dynamics of the motor is different. The modelling of the motor, drivers and output sensors is explained with dynamics clearly described. The control scheme used is PI control and the result showed. Although the research is in its prime, the result shows promising result.

Keywords – Multiple Motor, Synchronous Speed Control, Non-identical Motor, PID.

1. Introduction

Multiple motor drives are used numerously in unmanned system application such as Unmanned Aerial Vehicle (UAV), Unmanned Ground Vehicle (UGV) and Unmanned Underwater Vehicle (UUV). In this application synchronizing all motors is essential for navigation.

In the field, if a UGV was immobilize where by one of the motors was damaged, the user can changed the motors. If a correct motor were not available, the changed motor will not have a correct response. Thus, the overall control will not perform as designed. A solution for optimize and automatically synchronizing all motor need to be found even if all motors is not identical.

This paper explained about the initial development towards optimize and automatically synchronizing non-identical motors. The initial setup is that the reference signal is given by higher order controller and the motor should follow with all motors exhibiting the same control characteristics such as rise time and settling time.

2. Literature

Paper form D.Z.Zhao et. al. have developed a control scheme to synchronize four motor using cross-coupled sliding mode control [1]. In the paper, the motor is presumed identical and only caters for disturbance affected by one of the motors. That motors is than synchronous with the other motors. The result shows good stabilizing of the sliding mode control compared to PI control. Speed error for coupling control also shows good result compared to decoupling control.

Houcine Zeroug et. al. in their paper [2], shows a possible way to control two dc motor using a master and slave technique. It is presumed that the two dc motor have the same characteristic since the paper did not explicitly mention 'different/non-identical motors'. The speed variation and load variation is accessed with good tracking result of the slave based on the master.

The usage of DSP in multiple motor speed controllers is also used in paper from K. Boudjit [3]. He uses a master-slave technique which is almost similar to paper from [2]. He uses PID based controller with more in depth equation formulation. The speed variation and load variation is accessed with good tracking result of the slave based on the master.

Paper [4] by P.R.Moore et.al, describes a method for establishing the coupling between decoupled independent drives in multi-axis configuration via fuzzy logic [4]. The coupling is done on two identical servo motors which resulted in a good regulation of speed between the two motors.

Unfortunately, all the paper sited above and to the authors' knowledge, none of them have cater for multiple different motor control with different dynamics. This paper shows the initial development of a multiple non-identical four motors speed control scheme.

3. Hardware Development

The hardware was developed using four motor where three of them is identical. The specification for the motors can be seen in Table 1. Each motor comes with its own speed encoder which is then connected to a microcontroller. The microcontroller used is an Arduino UNO. Once the speed value has been acquired by the microcontroller, the microcontroller will generate the PWM value which is then inputted into the MD10C motor driver. The MD10C can drive a motor at a continuous current of 13A. The block diagram of the hardware can be seen in Fig. 1. The PC is only used for data acquisition. The fully developed hardware can be seen in Fig. 2 where all motors are fixed vertically on the wood board.

Table 1 Motor table.

Motor	1, 2 & 3	4
Type	PD3046	IG42E
Gear Ratio	19:1	24:1
Rated Torque (N.m)	0.17	0.98
Rated Speed (rpm)	320	248

4. Control Scheme

4.1 Control Scheme

The control scheme for the whole system can be seen in Fig. 3. A desired rotational speed, ω_d which is generated by the virtual leader is compared to the output of the speed sensor, ω_s . The resultant is then fed into the PID controller which output a PWM signal to the motor driver. The motor driver converts the PWM signal to voltage output to control the speed of the DC Motor. The resultant is the actual rotational speed, ω_a .

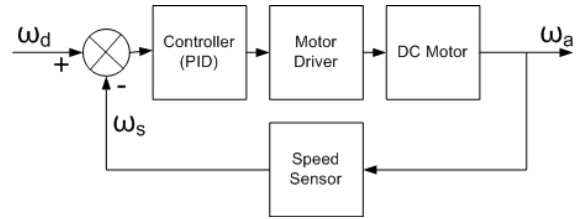


Fig. 3. Control block diagram.

4.2 Motor, Motor Driver and Speed Sensor Model

The dc motor with gear can be model as in Fig. 4. The subtraction resultant of terminal voltage, V_a and back emf voltage, E_a is fed into the electrical part of the system. The electrical part of the system is considered as a first order system which consists of the element motor inductance, L_A and motor resistance R_A . The output of the electrical model is then multiplied with the motor torque constant, K_T and then added to torque disturbance, T_1 . Here T_1 is negligible since the motor is in free run with only the shaft as its load.

The summing resultant is input into the mechanical part of the system which is also considered as a single order system with load inertia, J and friction, B_M . The output is multiplied with the EMF constant, K_E to produce E_a . The output is also fed into the gear system to produce the angular speed output from the motor.

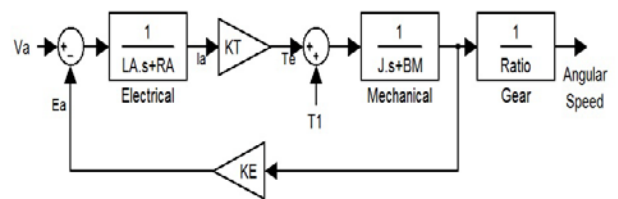


Fig. 4. DC Motor Model [5].

Fig. 1. Hardware block diagram.

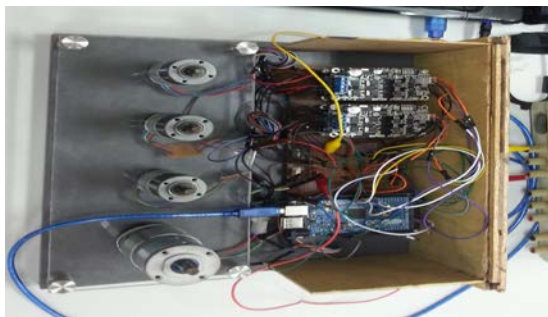


Fig. 2. Fully assembled hardware

The constant K_T , K_E , J , B_M and R_A are calculated via the datasheet given by the manufacturer. L_A is measured using the inductance meter. All constant for all motors can be seen in Table 2.

Table 2 Motor Parameters.

Motor	1, 2 & 3	4
K_T (Nm/A)	0.0147	0.149
K_E (V/rad/s)	0.0151	0.0158
R_A (Ω)	2.85	0.47
B_M (Nm/rad/s)	0.0022	0.0134
L_A (mH)	1.12	0.40
J (N/m ²)	9.3582E-7	1.0770E-6
Gear Ratio	19:1	24:1

Motor driver MD10C was used to drive all four motors. It is presumed that the motor driver has a very small lag time compared to the control timing loop. Thus, the model of the driver based on the datasheet can be seen in Fig. 5.

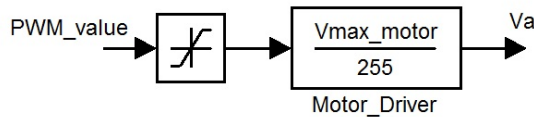


Fig. 5. DC Motor Driver Model.

The motors used are equipped with individual speed sensor. For motor 1, 2 and 3, 14 pulse/rev sensor output is used where for motor 4, 6 pulse/rev sensor output is used.

4.3 Controller

The initial control of the motors was developed based on virtual master to slave PID speed control. The PID control block diagram can be seen in Fig.6. The PID is manually tuned so that the close loop system is a damped system. This will eliminate any harsh speed changes. The PID values can be seen in Table 3. For future development, these PID will be auto tuned.

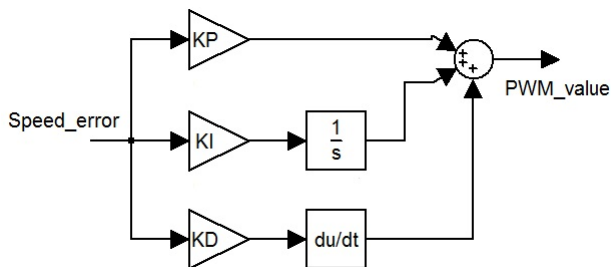


Fig. 6. Proportional, Integral and Derivative Controller

Table 3 PID Values

Motor	1, 2 & 3	4
K_p	20	21
K_i	10	12
K_d	0	0

5. Result and Discussion

The PID tuning is done manually and configured to make the system a damped system to eliminate jerking in the system. The partial PID tuning result can be seen in Fig. 7. Here $K_d=0$. Referring to Fig. 7, when K_p & K_i is set to 10 & 10 respectively, the system reach the goal (Speed = 100% @ 200 rpm) at about $t=1.8s$. After reaching the goal, the system fluctuates at $\pm 4\%$ of the goal. This can also be said when the system K_p % K_i is set to 15 & 10. When the system K_p & K_i is set to 15, the system reach the goal at $t=1.1s$ which is 0.6s faster than the previous set values. The system fluctuates at $\pm 4\%$ after reaching the goal which is the same as previous result. When K_p & K_i is set to 20 & 10 respectively. This value gives a smaller fluctuation of $\pm 4\%$ of the goal.

Since the system uses a PWM with a quantization value of 255 (8 bit), the system fluctuation value did not stay under $\pm 2\%$. The system may be able to fluctuate in $\pm 2\%$ value if the quantization value is set to 65535 (16bit).

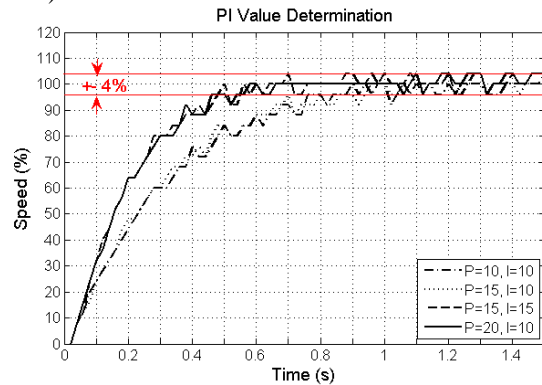


Fig. 7. Single motor PID tuning.

The system with the value of K_p , K_i & K_d set to 20, 10 & 0 respectively, is tested with variable speed as can be seen in Fig 8. It is found that at a lower speed the system fluctuate more than $\pm 4\%$ as depicted in Fig. 7. At a speed of 40 rpm, the system fluctuates $\pm 10\%$ which is twice as higher than exhibit in Fig.7. As the reference speed is increase to set to 80 rpm, the fluctuation of the system reduced to $\pm 6\%$. Increasing the reference speed even more, the system fluctuation is reduced to $\pm 5\%$ which is nearing the fluctuation depicted in Fig. 7. This suggest that the system speed will fluctuate even more if the reference speed in reduced below 40rpm. This problem can to be remedied if the speed sensor is increase in accuracy.

Acknowledgement

Alhamdulillah. The authors would like to thank Universiti Malaysia Pahang for giving monitory fund under RDU1303115, "Design & Control Flood Drone for Search and Rescue". We would like to also thank FKEE, UMP for partially funding for the project under FYP".

References

- [1] D.Z.Zhao, C.W.Li and J.Ren, "Speed synchronization of multiple induction motors with adjacent cross-coupling control", IET Control Theory and Application, Vol. 4, Iss. 1, pp. 119-128, 2010.
- [2] Houcine Zeroug, Kamel Boudjit, H. Kachroud and H. Sahraoui, "Speed Synchronization Control of Multiple DC Motors Using DSP", Proceedings of the 4th European DSP in Education and Research Conference,
- [3] K. Boudjit, "Real-Time Digital Control Using DSP of a Multiple Motors System", Journal of Electrical Systems, Special Issues N° 01, pp. 30-35, 2009.
- [4] P.R. Moore and C.M. Chen, "Fuzzy Logic Coupling and Synchronized Control of Multiple Independent Servo-Drivers", Control Eng. Practice, Vol 3, No 12, pp. 1697-1708, Elsevier Science, 1995.
- [5] Luca Zaccarian, "DC motors: dynamic Model and control techniques", Teaching material, http://control.disp.uniroma2.it/zack/LabRob/DCmotor_s.pdf, Accessed on 6th January 2013.

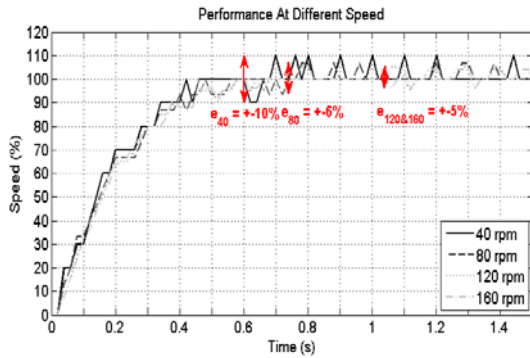


Fig. 8. Motor Performance at Different Speed with $K_p=20$, $K_i=10$ and $K_d=0$ for Motor 1,2 &3.

4 motors were tested with the pre-set K_p , K_i & K_d value depicted in Table 1. The reference speed was set to 150 rpm. Referring to Fig. 9, the first three identical motor performed almost identically with a rise time, $T_r=0.43s$. Motor 4 which is not identical to motor 1-3, lags about 0.18s. Although there is a lag, it is small for a single step input. For multiple step input, the lag will accumulate.

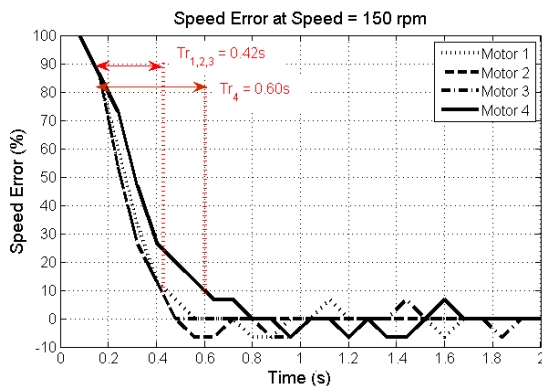


Fig. 9. Speed error for all motors with K_p , K_i and K_d described in Table 3.

6. Conclusion and Future Works

A non-identical four DC speed motor control has multiple uses in robotics. One example is the synchronization motors in UGV if a particular motor for servicing cannot be bought / found. This paper has shown an initial research and development of synchronizing multiple DC motors. Although this research is still in its infancy, the initial result has shown promising result.

Currently, the research is going towards MFC with PSO optimization. In terms of hardware, a 16 bit PWM is implemented.

CFD Analysis for Rigid Moving Body at the High Tidal Environment of Sea-bed

Md. Moktadir Alam¹, and Addie Irawan²

^{1,2} Robotics and Unmanned Systems (RUS) Group, Faculty of Electrical and Electronics Engineering, Universiti Malaysia Pahang, Pekan, 26600, Malaysia

(E-mail: moktadir.alam@hotmail.com¹, addieirawan@ump.edu.my²)

Abstract - In this paper, the basic hydrodynamic theories have been used to find the hydrodynamic factors for the underwater moving rectangular body as considered the shape of underwater walking robot. The added-mass, wave drag and lift coefficients are determined using a frequency-domain, simple-source based boundary integral method. In this paper, the hydrodynamics added mass and drag forces will be determined theoretically using Buckingham π theorem. Through numerical calculation the Reynolds number is measured in order to understand the type of water flow over the structure. The relative velocity vectors, Reynolds number, drag and lift forces for each state of motion is obtained in both static water condition and in ocean current condition. Results are obtained for a range of wave frequencies and depths of the underwater robotic body submerged all for a fixed water depth of 50-100 m. With the wave exciting force and moment determined using the Navier-Stokes theory. The computational study is to determine body-shape effects on the incident and radiated wave forces and subsequently the motion response. This study and results further implemented to modern adaptive drag force model-based controller in horizontal flow disturbance control for underwater multilegged or wheeled robot.

Keywords - CFD, Neiver-Strokes, Hydrodynamics, Reynolds Numbers.

1. Introduction

In the recent years, the applications of autonomous underwater vehicles (AUVs) have been expanding and now include fields such as marine research, technical investigations, deep-sea development and undersea projects. Depending on the underwater robotic body size and shape the AUV's can be divided into two categories and the shape is determined by the requirements of the robot's operation and task. For an instance, a streamlined shape AUV is able to reduce water resistance and is

preferable if the vehicle must move at high speeds. Whereas, if underwater detection or operation tasks are the primary roles of an underwater robot, a non-streamlined shape is often used. Deep-sea research requires high water-pressure resistance, while monitoring and observation tasks require small, flexible and stable robots[1].

A dynamics model is necessary in the design of guidance, navigation and control (GNC) systems of an underwater robotic system. The need for performance improvements in GNC has motivated deeper investigation into hydrodynamics modeling and the identification of the robot dynamics. However, the identification of hydrodynamics parameters is very difficult and challenging as reported[2]. It is complicated to tune an exact and comprehensive dynamics model for an underwater walking robot due to the hydrodynamics parameters. In particular, the hovering and tight maneuvering motions of an underwater vehicle is difficult to characterize hydro-dynamically as the hydrodynamic drag and lift forces relates the interaction between the robotic object and the fluid surrounding which is very robust and changes based on the system dynamics as well as the environmental situations[3, 4]. Researchers have adapted various numerical approaches such as Lagrange method based Morison equation, DATCOM method, Roskam method, kinetic energy theorem based on fluid mechanics theory to model the appropriate hydrodynamic profile[5] for underwater robotics. Currently, there are many Computational Fluid Dynamics (CFD) software packages like ANSYS, FLUENT, OPENFLOW to study AUVs reaction to hydrodynamic forces and flow simulations[6, 7].

In this paper, the hydrodynamic drag and lift forces will be determined numerically using the continuity equation for unsteady motion of a viscous compressible fluid having variable physical properties and then verified with

the CFD tool. Because of waves, wind and ocean currents the submerged system will experience a significant impact on its dynamics. Waves are stimulated by several aspects such as wind, surge, storm waves and Stokes drift. In order to form a statistical explanation of wave, derived from an estimated wave - a linear propagating wave theory can be derived, which is based on potential theory and Bernoulli's equations[8]. However, sea current is due to horizontal and vertical flow of ocean water produced by tides, neighboring wind, Stokes drift of central ocean exchange, storm flows and strong density variations in the upper level of ocean which is a mutual action of exterior heat exchange and salinity alterations.[9] A hydrodynamic load is induced on the underwater system due to tidal current which is caused by wave consequence and movement of the adjacent elements of water spectrum.

2. Hydrodynamic Factors to be considered for submerged robotic body Operation

There are many significant factors that are to be considered in order to model proper hydrodynamic profile for legged underwater walking autonomous system when the robotic body is submerged[10]. In this case we considered The Ekman layer of sea bed which is the layer where there is a force balance between pressure gradient force, Coriolis force and turbulent drag. The length, height and width of the underwater moving body are considered as 2.2 m, 1.8 m and 2.8 respectively.

2.1 Added Mass

Due to kinetic energy exchange between the system and the surrounding water, the added mass origins hydrodynamic force. While the system moving with absolutely positive acceleration with respect to the adjacent fluid, in such case to stimulate movement of the system, the inertial forces of the nearby particles of water need to be remunerated. Whereas, for the situation of a absolutely negative acceleration with respect to the surrounding fluid, the flowing water particles will restore their kinetic energy to the system. Therefore, the added mass for an immersed system is much higher than the normal or dry mass.

From studies it has been found that the added mass depends on the fluid characteristics, the system orientation, and the body frame route of the acceleration and are applied logically at the centre of gravity of the adjacent flowing water.

2.2 Hydrodynamic Damping

When a robotic system is submerged in viscous fluid, it goes through a force because of the relative velocity of fluid and system itself. This force can be alienated between the 'drag force' which is a component along the velocity direction and the 'lift force' which is perpendicular of the drag force, as illustrated in Fig. 1

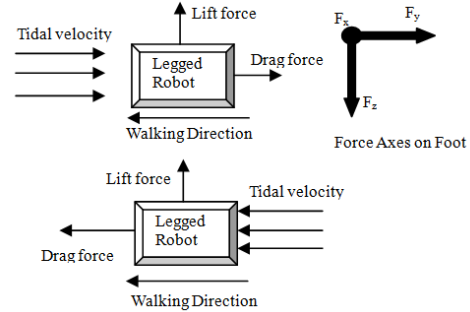


Fig 1: Lift and drag force according to relative velocity of underwater environment

From dimensional analysis and by using the Buckingham π theorem, the drag force acting on a submerged object is:

$$F_d = \frac{1}{2} d_w C_d A_{cs} v_r |v_r| \quad (1)$$

And, the lift force can be calculated as follow:

$$F_l = \frac{1}{2} d_w C_l A_{cs} v_r |v_r| \quad (2)$$

Where, F_d is the drag force, F_l is the lift force, according to International Association for the Properties of Water and Steam (IAPWS) at 20° C temperature ocean water density $d_w=1024.8103 \text{ kg/m}^3$, A_{cs} is the cross sectional area perpendicular to the direction of the flow, V_r is relative velocity of the object relative to the water, C_d and C_l are respectively denoted as the drag and lift coefficients.

From [11], the drag coefficient for a submerged object is a function of Reynolds Number. The Reynolds Number for non-dimensional flow can be expressed as follows:

$$R_e = \frac{d_w V L}{\mu_w} \quad (3)$$

Where, V is the velocity of flow, L is the characteristic length, and dynamic viscosity for ocean water, $\mu_w=0.001077 \text{ Pa.s}$ [12].

The Reynolds number is defined as the ratio of inertial forces to viscous forces and consequently quantifies the relative importance of these two types of forces for given flow conditions. Reynolds numbers frequently arise when performing scaling of fluid dynamics problems, and as such can be used to determine dynamic similitude between two different cases of fluid flow. They are also used to

characterize different flow regimes within a similar fluid, such as laminar or turbulent flow: laminar flow occurs at low Reynolds numbers, where viscous forces are dominant, and is characterized by smooth, constant fluid motion; turbulent flow occurs at high Reynolds numbers and is dominated by inertial forces, which tend to produce chaotic eddies, vortices and other flow instabilities.

3. Simulation and Results

The Reynolds number (Re) is a dimensionless quantity that is used to help predict similar flow patterns in different fluid flow situations. From the basic theories of fluid mechanics, flow with the same Reynolds number (in domains with the same shape) will be similar[11]. As Re increases, the equation becomes inviscid. Reynolds number is obtained from the value of mean ocean water velocity as depicted in the Fig. 2 which indicates that the flow is turbulent.

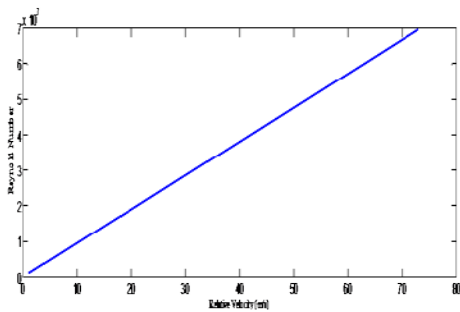


Fig 2: Reynolds number with Relative Velocity

With Eulerian and Lagrangian coordinates, the flow is to describe using quantities as a function of a spatial location x and time t , e.g. the flow velocity $u(x, t)$. The incompressible Navier-Stokes equations in a rectangular domain with prescribed velocities along the boundary, the solution method is finite differencing on a staggered grid with implicit diffusion and a Chorine projection method for the pressure. Visualization is done as in Fig. 3 by a colormap-isoline plot for pressure and normalized quiver and streamline plot for the velocity field at relative velocity of 10 ms⁻¹ applying Newton's second law to fluid motion, together with the assumption that the stress in the fluid is the sum of a diffusing viscous term (proportional to the gradient of velocity) and a pressure term—hence describing viscous flow.

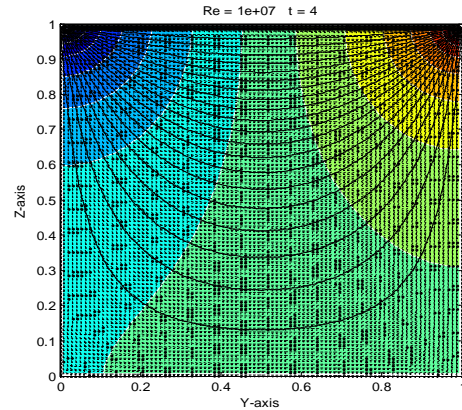


Fig 3: Flow dimension over the submerged body at seabed environment

For simulation, we also use the Flowsquare software as a CFD tools and validate the data for various relative velocities as in Fig. 4

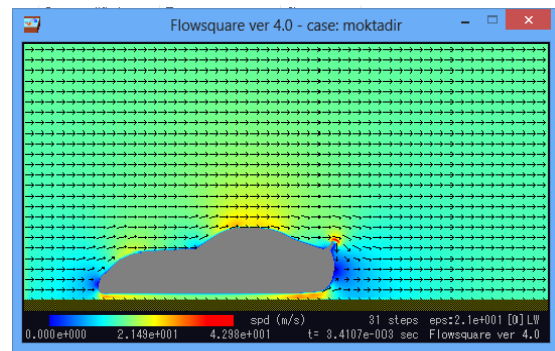


Fig 4: Fluid flow effect on submerged body using Flowsquare

4. Conclusions

In this study, we assume that the flow starts from a reference configuration and is mapped into its deformed configuration. Mathematically it can be described as a map as in Fig 3, called flow map, from the reference coordinate to the Eulerian coordinate. The solution of the Navier–Stokes equations leads to a velocity field or flow field, which is a description of the velocity of the fluid at a given point in space and time. Once the velocity field is solved for, other quantities of interest, such as flow rate or drag force can be determined. In our case, we consider the underwater robotic body shape as rectangle to analyze the hydrodynamic effect on the body. In the future work, the real robotic body shape will be considered to analyze and measure the perfect hydrodynamic effects on underwater walking robot. The study results further can be implemented to model and control multilegged or wheeled robot efficiently and stably at seabed.

Acknowledgement

This research is supported and funded by the Ministry of Education (MOE), Malaysia under the Research Acculturation Collaboration Effort (RACE) in collaboration with Underwater Robot Research Group (URRG), Universiti Sains Malaysia (USM) and partly supported by Graduate Research Scheme (GRS) of Universiti Malaysia Pahang (UMP).

References

- [1] C. Yue, S. Guo, and L. Shi, "Hydrodynamic analysis of the spherical underwater robot SUR-II " *International Journal of Advanced Robotic Systems* 2013.
- [2] E. YH, L. WS, L. E., S. GGL, and C. Chin. Estimation of the Hydrodynamics Coefficients of an ROV using Free Decay Pendulum Motion [Online].
- [3] K. M.Tan , T.-F. Lu, and A. Anvar, "Drag coefficient estimation model to simulate dynamic control of autonomous underwater vehicle (AUV) motion," in *20th International Congress on Modelling and Simulation*, Adelaide,Australia, 2013
- [4] G. Xu, X. Shen, and K. Yu, "Modeling and hydrodynamic performance for a deep ocean manipulator based on numerical approach " *Journal of Computers*, vol. 8, pp. 1192-1199, 2013.
- [5] D. A. Jones, D. B. Clarke, I. B. Brayshaw, J. L. Barillon, and B. Anderson, "The Calculation of Hydrodynamic Coefficients for Underwater Vehicles," D. P. S. Laboratory, Ed., ed. Australia, 2002.
- [6] M. Listak, D. Pugal, and M. Kruusmaa, "CFD simulations and real world measurements of drag of biologically inspired underwater robot," presented at the US/EU-Baltic International Symposium, Tallinn, 2008.
- [7] Y. Chunfeng, G. Shuxiang, and L. Maoxun, "ANSYS FLUENT-based modeling and hydrodynamic analysis for a spherical underwater robot," in *IEEE International Conference on Mechatronics and Automation (ICMA)*, Takamatsu, 2013, pp. 1577-1581.
- [8] L. Lionel, "Underwater Robots Part II: Existing Solutions and Open Issues," in *Mobile Robots Towards New Applications*, ed.
- [9] R. M. Wu and D. J. Lee, "Hydrodynamic drag force exerted on a moving floe and its implication to free-settling tests," *Water Research*, vol. 32, pp. 760-768, 3/1/ 1998.
- [10] L. L. Whitcomb, "Underwater robotics: out of the research laboratory and into the field " in *Proceedings of the 2000 IEEE International Conference on Robotics & Automation*, San Francisco, 2000
- [11] Munson, Young, and Okiishi, "Fundamentals of Fluid Mechanics," *Wiley Higher Education*.
- [12] ITTC, "Fresh Water and Seawater Properties," presented at the International Towing Tank Conference, 2011.

Combination of Transverse-Trot Gait Pattern for Quadruped Walking Robot

Yee Yin Tan¹ and Addie Irawan²

Robotics & Unmanned Research (RUS) group, Faculty Electrical & Electronics Engineering, Universiti Malaysia Pahang, Pekan, Pahang, 26600, Malaysia
(E-mail: addieirawan@ump.edu.my¹, yeeyin1228@gmail.com²)

Abstract—This paper presents a combination of transverse and trot walking pattern technique for hexa-quad robot after transformation to optimize the multi-legged robot operation and walking performances. Due to the limitation on the stability of hexapod robot, the combination of hexa-quad walking sequence is proposed to stabilize the quadruped configuration and walking modes. Quadruped robot configuration is stand within dynamically and statically stable criteria if compare to the hexapod robot that has only statically stable criteria. Thus, it is very crucial to have a stable walking sequence technique during walking and operation session. Therefore walking sequence technique to perform for hexa-quad transformation is proposed based on robot's Center of mass (CoM) and defined support polygon on positioning the leg in transformation process. A real-time based model of hexapod robot control architecture with proposed walking sequence is designed and validated using separated 3 dimensional (3D) simulators. The analysis of robot stepping foot motion is done to verify the desire designed walking sequences and the Body Mass Coordinate (BMC) is analyzed for way point of robot walking.

Keywords - Hexa-Quad robot, Centre of Mass, support polygon, robot.

1. Introduction

Recently, many researches had shown an increase interest in multi-legged robot. Many applications is endangered for human to be involved. Thus, legged robots have wide range of applications and used in many tasks that cannot accomplish by wheeled robots [1]. Quadruped robots have high adaptability and flexibility. It not only can walk on flat terrain and also move in unstructured terrain [2]. There are two parts of stability studies for quadruped robots which are statically stable and dynamically stable. The stability of the robot will ensures that whatever speed the robot can reach. Locomotion is one of the basic function to control the stability of the robot [3]. The legs of the robot is the main strategy to accomplish the locomotion [4].

Based on the study of reconfiguration of hexa-quad transformation, the walking pattern of the robot is crucial since the walking locomotion is the fundamental problem to be solved for all walking robot during their operation.

The development of walking pattern is a challenging task because it needs to consider the degree of freedom (DOF) and the Centre of mass (CoM) within the support polygon pattern of the robot which control the stability of the robot. [5]. According to Uchida H. *et. al* research studied that using mine detection to realize the stability walking of the six-legged robot by considering the attitude control method with the hydraulic actuator. This proposed technique involved the thigh driving torque of every supporting legs and the outputs are the height of the robot's body and the pitching and rolling angle. On the other hands, Tsujita K. *et. al* has overcome the timing problem between varies gait pattern which involve transverse, rotary, pace, bounce and trot gait pattern for quadruped robot. In this studies considered the analysis on the suitable gait pattern for the quadruped robot by proposed the adaptive control [4]. A considerable amount of studies has published about the robot leg failure strategies and the solution to solve the legs failure problem. Yang J.M. *et. al* studies used the term fault tolerant for their alternative gait pattern which proposed the periodic quadruped and hexapod gait that to considered the analysis of the joint failure of the gait pattern so that to control the stability of the robot. [6]. More recently, Yang J.M. do proposed a scheme to overcome the problem on the leg failure by retaining the fault tolerant of the gait pattern. Each joint of the robot's legs joint should lock individually associated to the damage motor so that the locked joint legs could be used for the support rather than moving. Apart from that, Tsujita K. *et. al* discussed the control of motion of quadruped robots with emphasis the dynamics gait of robot's transition control. This paper make a study on investigate the relationship between the locomotion speed which involved transverse and trot locomotion speed and the stability of the locomotion. The studies make analysis on the roll and pitch angle. The stability of the robot locomotion is examined that the roll and pitch angle are concentrate at a fitness point that proven that the locomotion is considered stable. Other effort has been done by proposed the gait regulation technique to increase the robustness in multi-legged robot walking pattern. For a single duty of a developing gait pattern, need just ignore the kinematic mapping and the consideration of keep more legs contact with the surface. Due to the limitation recirculation speed, the trot and tripod gait pattern can perform signification faster than other[7]. According to the lift and release probabilistic events [8] for each leg of

legged robot, tripod pattern for hexapod robot is less and producing faster movement.

Quadruped robot is considered in between dynamic and static stability which needs a combination of suitable walking pattern. Therefore, in this paper, the combination of transverse and trot walking pattern has been proposed for the quadruped robot. The combination of the transverse and trot walking pattern is depending on the foot motion and end-effector movement of the robot legs so that the CoM is within the support polygon pattern.

2. Walking Pattern and Shoulder-Based Coordination System

Shoulder-based coordination system (SCS) was established implemented in the previous progresses for hexapod configuration such reported in [9, 10] but not for quadruped configuration. For the quadruped robot, the combination of transverse and trot walking patterns [4] are proposed for the quadruped walking algorithm. The sequences of the legs for quadruped are presented in finite state machine (FSM) as shown in Fig. 1 on quadruped combination of transverse-trot walking pattern is used to perform walking with minimum area of support polygon in quadruped robot stability.

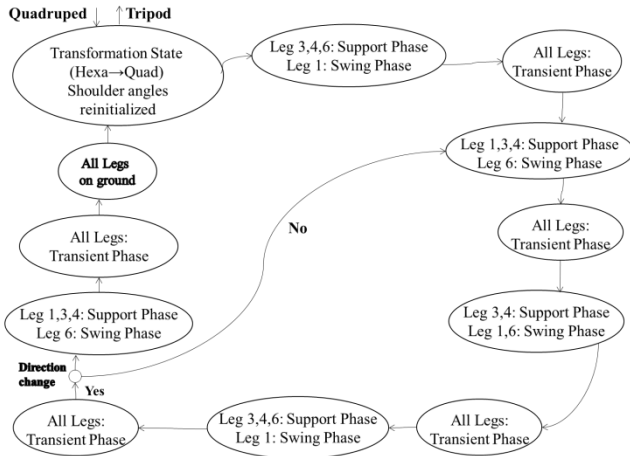


Fig. 1: FSM for quadruped transverse-trot walking pattern

The Quadruped Walking Sequence (QWS), which are the relationship between motions of the legs, are designed. There are two gait patterns that combine to form a statically and dynamically stable walking pattern for this quadruped robot. For this proposed walking pattern that maximum legs contact with the ground is two legs at a time which is the combination of transverse and trot gait pattern during locomotion.

For the transformation walking pattern, the combination of transverse and trot gait patterns are proposed for the quadruped walking algorithm. The sequence of the swing legs are represented by the white circles and the black circles represent stay legs which shown in Fig. 2.

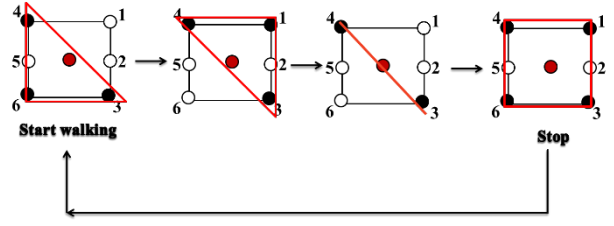


Fig. 2: Proposed Combination of Transverse and Trot QWS

After transformation, the walking gait patterns proposed is depending on the support polygon and the CoM of the robot. At different transient has different support polygon and CoM. The shape of support polygon depends on the stay legs and the CoM will not always at the center. It depends on the movement and the support on the ground. Therefore it will slightly near to the support stay legs This method walking patterns is proposed so that the walking velocity of the robot will not slow and maintaining the stability of the robot. The Fig. 1 shows the FSM of the foot motion of the quadruped robot following the sequence of legs lifting and placing.

In Fig. 1, from the hexapod to quadruped, the 1st sequence is 1st leg swing phase followed by 6th leg swing phase. The sequence followed by the 3rd and 4th legs together as swing phase. For the next sequence, it followed the 1st sequence as 1st leg in swing phase. The transient phase is added for each sequence so that to prevent the legs hitting each other. The system will reset when the walking direction changed. As shown in Fig. 1, in transformation state, θ_a is changed and used on both x and y position of leg on the next sequences. x and y for each n -leg are part of moving frame and kinematics element for each link on each leg as shown in Fig. 3. Both positions including vertical leg position (z) is determined differently in each support and swing phase by using Eq.2 and Eq.3 respectively. Both Eq.2 and Eq.3 were created to realize the motion shape as shown in Fig. 3. This motion shape is important for the force control implementation on each robot foot for walking on irregular terrain. As shown in Fig. 4, (1) leg standing up, (2) swing phase (first step), (3) support phase, and (4) swing phase (next step).

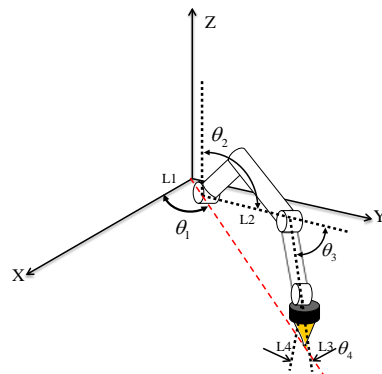


Fig. 3. SCS trajectory kinematics motion for a 4-DOF leg of hexapod robot model

(Support Phase – Step and push on the ground) $0 \leq t \leq \frac{T_c}{2}$

$$\begin{aligned} x_{s_n}(t) &= x_{0_n} + \frac{S_o}{4} \left(\frac{2t}{T_c} - \frac{1}{2\pi} \sin\left(\frac{4\pi t}{T_c}\right) \right) \cos \theta_{a_n} \\ y_{s_n}(t) &= y_{0_n} + \frac{S_o}{4} \left(\frac{2t}{T_c} - \frac{1}{2\pi} \sin\left(\frac{4\pi t}{T_c}\right) \right) \sin \theta_{a_n} \\ z_{s_n}(t) &= z_{0_n} \end{aligned} \quad (1)$$

(Swing Phase) $0 \leq t \leq \frac{T_c}{2}$

$$\begin{aligned} x_{s_n}(t) &= x_{0_n} + \frac{S_o}{2} \left(1 - \cos\left(\frac{2\pi}{T_c} t\right) \right) \cos \theta_{a_n} \\ y_{s_n}(t) &= y_{0_n} + \frac{S_o}{2} \left(1 - \cos\left(\frac{2\pi}{T_c} t\right) \right) \sin \theta_{a_n} \\ z_{s_n}(t) &= z_{0_n} + H_0 \sin\left(\frac{2\pi}{T_c} t\right) \end{aligned} \quad (2)$$

where

- T_c = walking cycle time (s),
- t = update time (real-time) (s),
- t_{ex} = additional period for applying extra force (s),
- S_0 = distance of foot placement for one cycle (m), and
- H_0 = height of leg lift from the initial position (m).

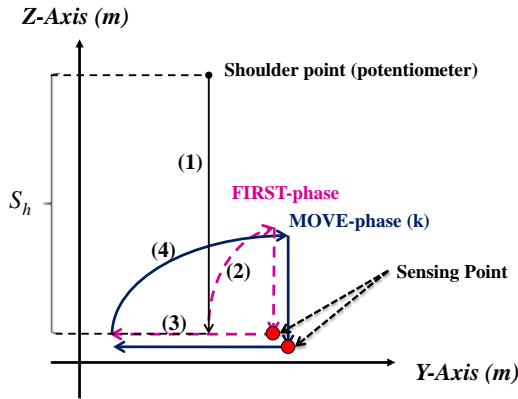


Fig. 4. A leg motion shape used in proposed model Hexa-Quad robot.

3. Simulation and Result

The walking algorithm for the proposed QWS is simulated in the state flow. The supporting legs and the swing legs are separated in the state flow. The input is given to the swings legs so that it can swing and move forward and placed back to the ground. The shoulder angle for every direction has different of the shoulder angle.

Fig. 5 shows the results after the design walking sequence in the simulator. The QWS is shows in the 3D simulator follow the sequence successively. Fig. 4 (a) is

the proposed QWS with the stop mode followed by the proposed QWS of 1st leg swing leg as in Fig. 4 (b). The proposed walking technique at 6th swing leg and Fig. 4 (d) is the third sequence of 3rd and 4th leg swing leg. The stepping foot motion of the transformation robot is analyze by studied from the graph. The beginning of each leg will have a trapezium shape. These show the robot at initial at sit down position. The trapezium represented the robot at stand up position. The triangle shape represented which legs is at swing position which away from the ground when its walk at the flat terrain as shown in Fig. 6 (a), (b), (c), (d).

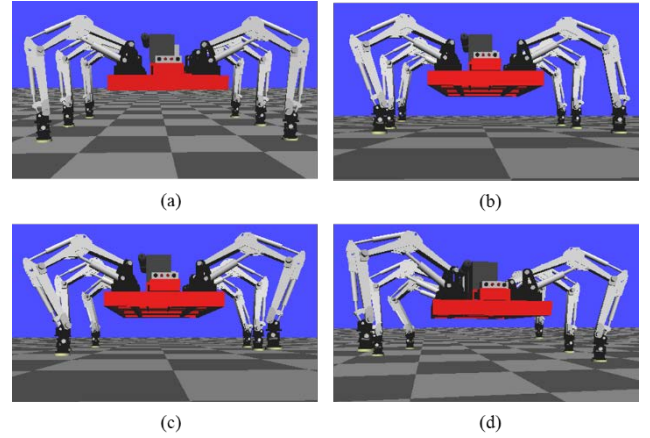


Fig. 5: The Proposed QWS in 3D Simulator (a) robot at stop mode, (b) 1st Leg swing phase, (c) 6th Leg swing phase, (d) 3rd and 4th Leg swing phase

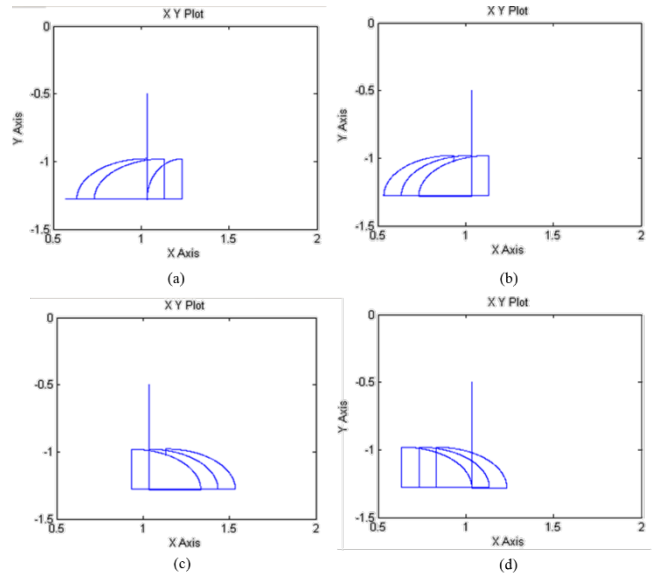


Fig 6: Stepping Foot Motion of Proposed QWS (a) Leg 1, (b) Leg 3, (c) Leg 4, (d) Leg 6

For the end-effector Movement point, the leg motion shape is plotted for y and z axis of each leg motion. From this analysis, the stability can be observed from the graph. Each leg show the different leg motion shape. The leg motion shape depends on each leg motion either in swing phase or in support phase as in Fig. 6 (a), (b), (c), (d).

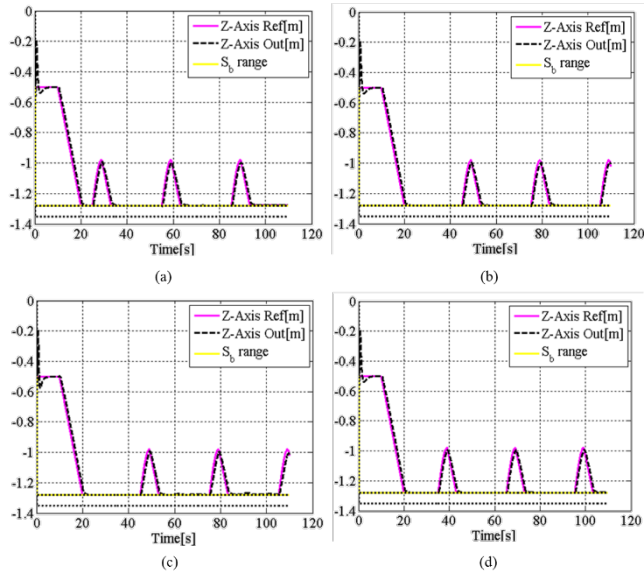


Fig 7: End-effector Movement Point of Proposed QWS (a) Leg 1, (b) Leg3, (c) Leg4, (d) Leg 6

During the support phase, the leg is at drag so that the robot can be move forward. The swing legs will step astride to forward direction. During the leg drag, the shape is showed at horizontal while the move phase is showed as half hemisphere as in the Fig. 7(a), (b), (c), (d). Quadruped mode walking is verified by simulating the performance of robot CoB with shown in Fig. 8. The CoB represented the body way point of the quadruped robot. Straight line of the BMC shows that it is detecting in only a direction not omnidirectional.

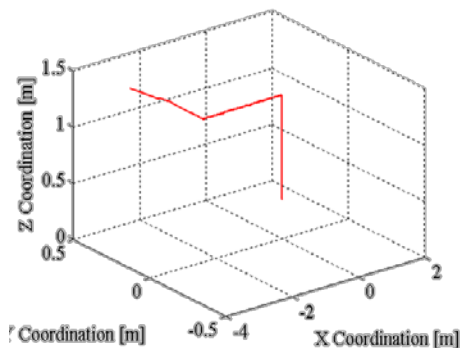


Fig 8: Body Mass Coordinate of Proposed QWS Way Point

4. Conclusion

In the conclusion, the concepts support polygon pattern and the CoM in the consideration of transformation technique which the robot disable the two legs from the others that to configure in the quadruped configuration. The algorithm of reposition transformation technique hexapod robot to quadruped is design by investigate quadruped walking gait design with considering the stability of the robot depends on the CoM and support polygon of the leg position in transformation process. A real-time based model of hexapod robot walking algorithm is designed in the core control architecture with proposed hexapod-to-quadruped transformation and validated using separated 3 dimensional (3D) simulators.

Acknowledgement

I would like to thank the Research and Innovation Centre, University Malaysia Pahang on funding support on this research project. A very appreciate thanks to my supervisor, Dr. Addie Irawan Hashim regarding his support and guide on this research project.

References

- [1] T.-S. Shih, C.-S. Tsai, and I. Her, "Comparison of Alternative Gaits for Multiped Robots with Severed Legs," *International Journal of Advanced Robotics System*, vol. 9, 03 August 2012.
- [2] R. B. Cai, Y. Z. Chen, W. Q. Hou, J. Wang, and H. X. Ma, "Trotting Gait of a Quadruped Robot Based on the Time-Pose Control Method," *International Journal of Advanced Robotics System*, vol. 10, 21 June 2013.
- [3] T. Katsuyoshi, K. Manubu, and T. Kazuo. (2004, A Study on Optimal Gait Pattern of a Quadruped Locomotion Robot.
- [4] K. Tsujita, K. Tsuchiya, and A. Onat, "Adaptive gait pattern control of a quadruped locomotion robot," presented at the IEEE/RSJ International Conference on Intelligent Robots and Systems, 2001, Maui, USA, 2001.
- [5] D. Belter and P. Skrzypczynski, "A Biologically Inspired Approach to Feasible Gait Learning for a Hexapod Robot," *Int. J. Appl. Math. Comput. Sci.*, vol. 20, 2010.
- [6] J. M. Yang, Y. K. Park, and J. G. Kim, *Mobile Robots Moving Intelligence*, ARS/pIV ed. Germany, 2006.
- [7] G. C. Haynes, "Gait Regulation Control Techniques for Robust Legged Locomotion," Doctor of Philosophy in Robotics, The Robotics Institute, Carnegie Mellon University, Pittsburgh, Pennsylvania, 2008.
- [8] R. Siegwart, I.R.Nourbakhsh *Introduction to autonomous mobile robots*: MIT Press, 2004.

- [9] A. Irawan and K. Nonami, "Compliant Walking Control for Hydraulic Driven Hexapod Robot on Rough Terrain," *Journal of Robotics and Mechatronics*, vol. 23, pp. 149-162, 2011.
- [10] A. Irawan and K. Nonami, "Force Threshold-Based Omni-directional Movement for Hexapod Robot Walking on Uneven Terrain," in *2012 Forth International Conference on Computational Intelligence, Modelling and Simulation (CIMSIM)*, Kuantan, Pahang, Malaysia, 2012.

Combining Tree-based Genetic Programming with Pareto Multi-Objective Optimization for Evolving Modular Robots

Wei Shun Chee¹ and Jason Teo²

^{1,2} Faculty of Computing and Informatics, Universiti Malaysia Sabah, Kota Kinabalu, 88400, Malaysia
(E-mail: wschee88@gmail.com)

Abstract - This paper explores the use of hybridized Genetic Programming and self-adaptive Differential Evolution algorithm to automatically design and co-evolve both the controller and morphology of heterogeneous modular robots. In this work, the Genetic Programming tree-based structure had been uniquely designed such that it can be used for both the modular robot's morphology and controller representation. This enable the ANN controller become flexible in design where the controller will be automatically optimized correspond to the change in the modular robot morphology. Consequently, the overall body structure and ANN controller of the robot are able to be co-evolved simultaneously during the artificial evolutionary process. In additional, the Pareto multi-objective optimization is also being implemented in conjunction with the evolutionary algorithm with the aim to maximize the modular robot forward moving behaviour while minimizing its complexity. Two experiments are conducted in this work in order to evolve the forward moving behaviour for two different types of modular robots which are the multi-branching modular robot and snake-like modular robot. The Pareto-optimal front solutions are also being obtained and identify throughout the artificial evolutionary process by using the multi-objective optimization. The results from the simulation show the promise of this work and illustrate the importance of co-evolving both the robots' bodies as well as their controllers.

Keywords - genetic programming; tree-based structure; modular robot; multi-objective optimization; Pareto-optimal front.

1. Introduction

In recent years, modular robots have become increasingly popular in robotic design as it is highly versatile and able to perform different movements. The modular robot is compact in size allowing it to move through thin holes and gaps where humans are incapable to reach. Furthermore, such robots are able to climb through obstacles taller than its body height. Since modular robots are formed by combinations of different modules, it makes the modular robot redundant in design. In other words, the modular robot can continue locomotion even when particular a module is malfunctioning. Because of all these unique features,

modular robots carry the potential of meeting the needs for robotic mobility in unknown and challenging environments. However, a modular robot is difficult to be designed and modelled as it possesses large numbers of degrees of freedom. Furthermore, the open-ended synthesis problem arises where humans do not know the optimum control strategy, robot structure, number of segments and segment length that the modular robot should be designed in order to have optimum performance [1]. Due to the lack of relevant information regarding on how the robot's morphology and controller relates to its behaviour, the modular robot is always be designed by joining the same modular unit with predefined segment length and number of segments decide by the designer [2,3]. After the morphology of the modular robot has been designed, only then its moving behaviours are manually being modelled by humans through mimicking the movement inspired from living creature [5,6]. Unfortunately, the modular robot designed using this approach might not necessary possesses the optimum morphology and controller for the optimum moving behaviour. As a result, with the intention to overcome these problems, an evolutionary algorithm which hybridizes both Genetic Programming (GP) and Differential Evolution (DE) is implemented in this work to automatically design and optimize both the morphology and controller of modular robot simultaneously.

Moreover, in most of the design using this method, it will only involve with a single objective function to accomplish the given task. Unfortunately, in most real-world situations and optimization problems, they are naturally involving multiple objectives where different objectives are equally important and may produce conflicting scenarios among them [7]. The same phenomena occurred in the field of modular robot design. This is because in many cases, the modular robot has been designed with the best performance or versatility might not feasible to be applied in the real world application due to its complexity or being constrained under certain condition such as the power consumption, space, manufacturing limitation and cost involved. As a result, in this work, multi-objective evolutionary optimization is being incorporated with the evolutionary algorithm to maximize the moving behaviour of the modular robot while minimizing on its complexity. By using this approach, heterogeneous modular robot with different number of segments and moving behaviour can

be found in one simulation run based on the Pareto-optimal front obtained.

From previous researched on co-evolving the morphology and controller of the robot, promising result are being shown by using different co-evolutionary approaches [8-11]. It was also found out that, better results are able to be obtained by hybridizing different evolutionary approaches in co-evolving and optimize the controllers and robot bodies compare to the classic evolutionary method [12,13]. There are also researches conducted using multi-objective optimization to optimize the control parameters and morphology of the robot [14,15]. However, to the best of our knowledge, there have not been any studies conducted yet in evolving the modular robot using evolutionary algorithm.

Distinct from previous researches, in this work, the Genetic Programming tree-based structure had been uniquely designed such it was used for direct representation of the morphology and controller of the modular robot. This enables the controller's neural network architecture become flexible in design which in turn allows the overall body structure and ANN controller of the robot to be co-evolved simultaneously throughout the artificial evolutionary process.

2. GP Tree-based Structure

2.1 Morphology Representation

In this work, a unique tree-based structure is implemented for the modular robot's morphology representation. Each structure unit of the GP tree is representing a segment of the modular robot. Besides that, the physical properties of the modular robot segment such as the segment numbering, segment length, number of branches attached, and position to be attached are encoded in it. An example of the tree-based structure and its corresponding morphology representation of the modular robot are shown in Fig. 1.

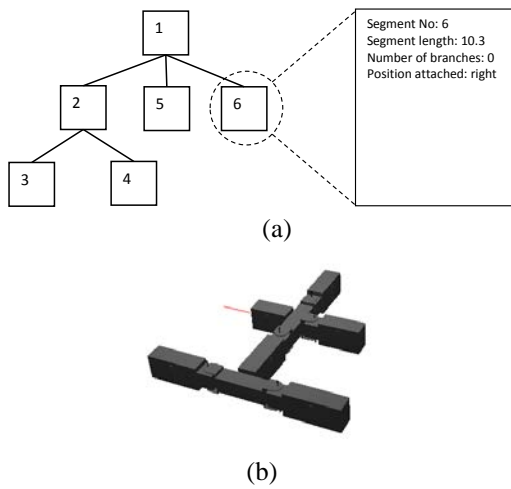


Fig. 1. (a) Example of three-base structure generated with segment specification encoded inside. (b) Modular robot morphology representation based on the tree-based structure.

The multi-branching modular robot is being designed such that all the segments are connected to each other jointed by 2 motors, one rotating at the x-axis while the second motor rotates at the z-axis. On the other hand, the snake-like modular robot can also be represented using the GP tree-based structure by restricted the number of branching segments to 1. An example of the snake-like modular robot created is shown in Fig. 2.



Fig. 2. Snake-like modular robot created and represented using GP tree-based structure.

2.2 Chromosome and ANN Representation

In this work, a three layer feed-forward artificial neural network is implemented as the neural controller for the modular robot. The input neurons for the ANN of the multi-branching modular robot are the touch sensors attached on every segment and the current position's angle of all motors. On the other hand, the output neurons for the multi-branching modular robot are the control signal that fed to every motor to control the subsequent angle to move to.

For the snake-like modular robot, the input neurons for the ANN are the touch sensors attached on every segment and an infrared sensor mounted at the first segment. Meanwhile, there are total of three output neurons exist in the output layer of the ANN which present as the amplitude, frequency and phase shift for the sinusoidal function.

In this work, the control strategy which used to control the overall movement of the modular robot are different between the multi-branching modular robot and snake-like modular robot. For the multi-branching modular robot, there are two motors to be controlled in each joint. The angle of every motor is being controlled based on the equation shown below,

$$\theta_i = 3.14 \times \sin(-1.57t + (i + 1) \times O_i) \quad (1)$$

Where,

θ = position angle

i = motor

t = time

O = output

In order for the snake-like modular robot to perform the forward moving behaviour, a sinusoidal function is being generated and used as the overall movement for the robot to propagate forward. The angle of every motor of the snake-like modular robot is being controlled based on the equation shown below.

$$\theta_i = O_1 \times \sin(-O_2 \times t + i \times O_3) \quad (2)$$

In this work, the rule of thumb which stated, the number of hidden neurons should be 2/3 the size of the input layer plus the size of output layer is being implemented to determine the number of hidden neuron to be used. For the purpose of calculating the number of hidden neurons to be used, the number of segment is made to become dependent variable. Based on the calculation, total of 3 hidden neurons will be represented by each structure unit for the multi-branching modular robot and 2 hidden neurons will be represented by each structure unit for the snake-like modular robot. However, it is noted that when there is change in number of segment during the artificial evolutionary process, the number of input and hidden neurons as well as the total number of ANN weights will be changed. In another words, the chromosome length of the modular robot is variable correspond to the change in number of segments. This means that, the normal fix length genotype string is not able to be implied in this work.

In order to make the ANN flexible in design, the tree-based structure that used for snake-like modular robot's morphology representation illustrated earlier is also being used to represent the ANN structure. This is done by encoding the ANN weights within structure unit of the tree-based structure. As a result, the whole tree-based structure can be connected together forming the chromosome of modular robot designed.

3. Evolutionary Algorithm

3.1 Genetic Programming

In this work, GP is used to perform the crossover operation on the tree-based structure representation between two evolve individuals in order to interchange both the morphology and genotype between the modular robots with the aim to produce better offspring and diverse population. As the physical properties and the chromosome of the modular robot are directly represented by the tree-based structure, both the morphology and control system of the modular robot are able to be co-evolved simultaneously through the crossover operations of the GP process. Before the crossover operation is being carried out, a random number will be generated by the system. Such random number is then being compared with the morphology crossover rate assigned for the particular individual. In order for the GP crossover process to be performed, the random number must be smaller than the morphology crossover rate.

In the crossover process, two individuals are randomly chosen and recombined to form two new offspring. The crossover process is accomplished by changing the pointer which points to the crossover sub-branches of the first parent to the crossover sub-branches of the second parent. As a result, all the information encoded within the crossover sub-branches are brought over and the modular robot morphology is being interchanged as well. After the sub-branches have been crossover, the segment numbering encoded within the unit structure is resorted in sequence. Besides that, the position to be attached before

the crossover operation is performed remains unchanged to avoid structure overlapping. The new offspring created are then tested in the simulated environment to evaluate their performance. If there is improvement on the offspring behaviour, it is used to replace the parent and becomes available for the next generation of the artificial evolutionary process, otherwise the parent is kept and the evolutionary process is repeated.

3.2 Self-adaptive Differential Evolution

In this work, the self-adaptive Differential Evolution algorithm is used for the mutation operation to modify the morphology properties and the artificial neural network's controller's weights of the modular robot. In this work, the Differential Evolution algorithm is implemented as the mutation operator in the system, while the self-adaptive mechanism is used to automatically adjust the weighting factor (F) and crossover probability (CR) control parameter throughout the DE process. These self-adapting control parameters F and CR are encoded in the genotype of every modular robot individual to determine whether DE crossover is to be performed on the vector and how the vector should be adjusted during the DE mutation operation. These control parameters are continuously being evolved and modified automatically throughout the artificial evolutionary process by using the self-adaptive control mechanism proposed by Brest et al. [16]. In this work, the mutation differential operation is being performed based on the equation shown below,

$$U_{r1,i,j} = \begin{cases} v_{r1,i,j} = x_{r1,i,j} + F(x_{r2,i,j} + (x_{r3,i,j} - x_{r4,i,j})), & \text{if } rand \leq CR \text{ or } j = j_{rand} \\ x_{r1,i,j} & , \text{otherwise} \end{cases} \quad (3)$$

Where,

U = trial vector

x = target vector

v = mutant vector

i = parameter

j = structure unit

j_{rand} = random selected structure unit

After the trial vector is being recombined forming the new chromosome, the performance of new created individual is compared with the donor individual and the one with a better fitness is selected and is made available for the next generation. In the case where the individuals involved in the DE process are differ in the total number of segments attached, the DE operation is only allowed to perform on a target vector until the maximum number of segment is reached in any individual chosen. If there are remaining segments which have not been accessed during the DE process, the remaining weights are modified using the equation given below,

$$U_{r1,i,j} = \begin{cases} v_{r1,i,j} = x_{r1,i,j} + F(N_{rand}) & , \text{if } rand \leq CR \text{ or } j = j_{rand} \\ x_{r1,i,j} & , \text{otherwise} \end{cases} \quad (4)$$

Where,

N_{rand} = random number generated ranging from -1 to 1

4. Multi-objective Optimization

In this research, the multi-objective evolutionary algorithm is implemented to maximize the moving behaviour of the evolved snake-like modular robot while minimizing its complexity. In this work, the complexity of the modular robot is depicted by the total number of segments possess by the modular robot. This is because, with higher number of segments, the input and output device will be increased which indirectly increase the ANN network size as well. This will make the network architecture become more complex and heavy processing load are required for the control system to perform all the calculation. Moreover, by having higher number of segment, more physical body parts, sensors and motor are needed for the construction of the modular robot which will greatly increase the complexity of the modular robot morphology and involved with high manufacturing cost and time in constructing the modular robot. From all the statements, it shows that the complexity of the modular robot can actually be minimized by minimizing the number of segments.

In order for the multi-objective optimization to be performed in the artificial evolutionary process, the system is being designed such that it will automatically compare and store the performance score of each individual according to the total number of segments. The individual information will be stored into the archive under two conditions: (a) if the fitness scores of the current evolved individual is higher than the previous stored individual with the same number of segments (b) if the individual with the particular total number of segments does not exist in the archive yet throughout the evolutionary process. Based on the archive created, it allows the system to identify the non-dominant solution and obtain the Pareto-optimal front solutions.

In this work, the artificial evolutionary process is being conducted in the standard way where the parent solution will be replaced by the children with the better performance score for every generation run. The system will automatically update the information in the archive according to the condition stated previously after each generation run. After the whole artificial evolutionary process had been carried out, only then the multi-objective optimization is being conducted on the individuals stored in the archive in order to obtain the Pareto-optimal front solutions.

5. Simulation

In this research, the artificial evolutionary process was carried out in virtual simulated environment using the Webots physics engine simulation software. The goal to be achieved by every evolved individual in the simulation is to progressively optimize on the morphology and controller such that it can move forward for the longest distance in straight line.

There are two experiments conducted in this work to evolve for the multi-branching modular robot and snake-like modular robot. All experiments are conducted with 10 runs, each run consists of 100 generation. For each

experiment run, a different initial population seeds of 10 randomly created individuals will be used.

For every individual run, a settling time of 1 second is provided for the robot to settle down in the simulation environment. Following by that, for every time step in the simulation, the performance score is compute based on the fitness function modelled shown in equation below,

$$Fitness\ score = \cos\theta \times \sum_{t=0}^{runtime} (x\ axis\ coordinate - origin\ x\ axis\ coordinate) \quad (5)$$

Where,

θ = angle deviate from origin

The angle deviated from origin is calculated based on the following equation,

$$\theta = \text{atan}\left(\frac{z\ axis\ coordinate - origin\ z\ axis\ coordinate}{x\ axis\ coordinate - origin\ x\ axis\ coordinate}\right) \quad (6)$$

In this work, the multi-branching modular robot is being limit to have maximum of 10 branching segments to be evolved in the simulation, while there is no constraint on the number of total segments to be evolved for the snake-like modular robot. This is because from preliminary test, it was found out that multi-branching modular robot with more than 10 branching segments are not feasible to be applied for locomotion as self-collision and overlapping might frequently occurred during the simulation.

6. Results

After all the experiments run is conducted on the multi-branching modular robot and snake-like modular robot, the fitness score of the overall best individual had been evolved though artificial evolutionary process for every experiment run is shown in Table 1.

Table 1 Overall best individual evolved with different total number segments among all experiment run.

Seg.	Fitness Score	
	Multi-branching	Snake-like
2	684.811	1.286
3	596.512	155.280
4	446.865	270.658
5	584.547	275.862
6	274.518	289.093
7	270.597	250.404
8	269.715	367.508
9	267.890	352.156
10	451.858	474.110
11		399.951
12		315.721
13		546.971
14		427.311
15		478.410
16		611.983
17		423.762
18		463.787
19		298.311
20		288.941

From Table 1, it shows that heterogeneous modular robots with different segment number are able to be evolved throughout the artificial evolutionary process by using co-evolutionary algorithm and multi-objective optimization technique illustrated in this work. Surprisingly, based on the results obtained, it was realized that the multi-branching modular robot evolved with less number of segments end up to be the better individual to perform the forward moving behaviour. The performance score of the multi-branching modular robot gradually decreased when the segment number increased. However, the multi-branching modular robot has a sudden increase in performance score when it is constructed with 10 segments. From the results obtained, it shows that the multi-objective optimization is not viable to be implemented in the case of co-evolutionary process for the multi-branching modular robot. This is because the Pareto-front solutions are converging to a point where the multi-branching modular robot with 2 segments turn up to be the dominating solution which it has dominated all other solutions in both objectives.

By analysing the results obtained for the snake-like modular robot, it was realised that the snake-like modular robot evolved through the artificial evolutionary process is able to perform better by having higher number of segments. However, when the total number of segments of the snake-like modular robot increased until a certain extent, the fitness score will start to decrease eventually. This reveals that, although the snake-like modular robot is likely to perform better by having higher number of segments, it will cause adverse effect on the moving behaviour if excess number of segment is being used. Furthermore, it can also be observed that, even though the snake-like modular robot evolved with less segments number is having a lower performance score, it can still able to perform the forward moving behaviour if the morphology and controller are being optimized.

By comparing the overall best individual evolved between the multi-branching modular robot and the snake-like modular robot, it can be found out that the multi-branching modular robot can outperform the snake-like modular robot in the forward moving behaviour. The overall best individual had been evolved for multi-branching modular robot is having fitness score of 684.82 with 2 segments while the overall best individual evolved for snake-like modular robot is having fitness score of 611.98 with 16 segments.

Since there is only a dominating solution being identify for multi-branching modular robot, there is no Pareto-optimal front solutions able to be obtained in that case. On the other hand, the Pareto-optimal front solutions obtained for the snake-like modular robot are shown in Table 2. Furthermore, based on Table 2, a graph is being plotted to present the Pareto-optimal front obtained for the snake-like modular robot which shown in Fig. 3.

Table 2 Pareto-optimal front solutions obtained for snake-like modular robot.

Total Segment	Fitness Score
2	1.286
3	155.280
4	270.658
5	275.862
6	289.093
8	367.508
10	474.110
13	546.971
16	611.983

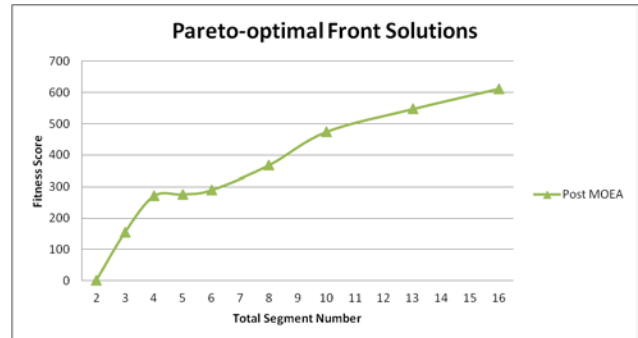


Fig. 3. Pareto-optimal front obtained for snake-like modular robot.

In order to analyse on the progression of the evolutionary process being carried out on the evolving snake-like modular robot population, the graph of the population fitness score for the 2nd experiment run for snake-like modular robot where the overall best individual had been evolved are being plotted and shown in Fig. 4.

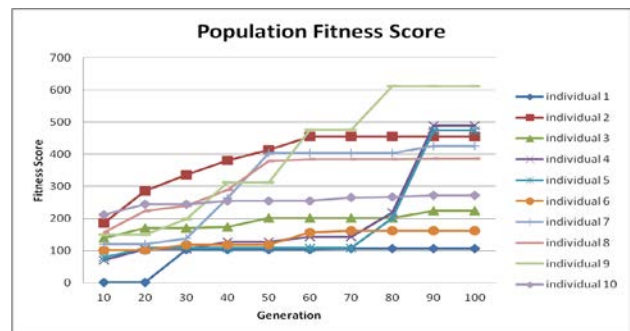


Fig. 4. Population fitness score for 2nd experiment run of the snake-like modular robot.

From Fig. 4, it shows that the forward moving behaviour of the snake-like modular robot is able to be improved from generation to generation. The same observation can be obtained in multi-branching modular robot. This indicates that the hybridized GP and self-adaptive DE co-evolutionary algorithm presented in this work is feasible to be implemented to co-evolve both the morphology and controller of the snake-like modular robot such that both the morphology and control system

is able to be optimized in order for the modular robot to acquire with forward moving behaviour.

The screenshots of the simulation run of multi-branching modular robots and snake-like modular robot are shown in Fig. 5.

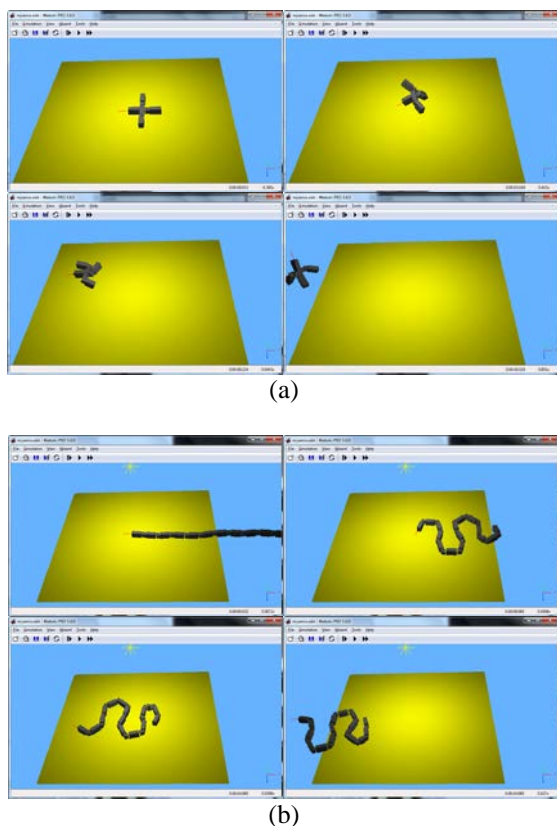


Fig. 5. Screenshot of simulation run of the evolved individuals for (a) multi-branching modular robot (b) snake-like modular robot.

It was found out that the multi-branching modular robot was evolved such that it has the capability to flip its body over to move forward. On the other hand, the snake-like modular robot can perform lateral undulation movement to propagate the whole body to move forward.

4. Conclusion

In summary, promising results are shown for the implementation of a hybridized GP and self-adaptive DE for automatically designing and co-evolving both the controller and morphology of modular robots. With the GP tree-based structure uniquely designed for the modular robot morphology and ANN representation, it allows the controller and body structure co-evolving process to be carried out simultaneously. Interesting findings were obtained in this work by analysing on the evolved behaviour and morphology of the modular robot. With the implementation of the multi-objective optimization, the Pareto-optimal front solutions are also successfully obtained by taking consideration of two objectives which are to maximize the moving behaviour of the modular robot and minimize its complexity.

References

- [1] H. Lipson, "Evolutionary Robotics and Open-Ended Design Automation," in *Biomimetics: Biologically Inspired Technologies*, Y. Bar-Cohen, Ed., Boca Raton, CRC Press, 2006, pp. 129-156.
- [2] A. Crespi, A. Badertscher, A. Guignard and A. J. Ijspeert, "AmphiBot I: an amphibious snake-like robot," *ISR Biomimetic Robotics*, vol. 50, no. 4, pp. 163-175, 2005.
- [3] J. K. Hopkins, B. W. Spranklin and S. K. Gupta, "A survey of snake-inspired robot designs," *Bionispiration and Biomimetics*, vol. 4, no. 2, 2009.
- [4] S. Hirose, *Biologically Inspired Robots: Snake-like locomotors and manipulators*, New York: Oxford University Press, 1993.
- [5] K. Lipkin, I. Brown, A. Peck, H. Choset, J. Rembisz, P. Gianfortoni and A. Naaktgeboren, "Differentiable and piecewise differentiable gaits for snake robots," *Intelligent Robots and Systems*, pp. 1864 - 1869, 2007.
- [6] K. Deb, *Multi-Objective Optimization using Evolutionary Algorithms*, England: John Wiley & Sons Ltd, 2004.
- [7] K. Sims, "Evolving 3D morphology and behavior by competition," *Artificial Life*, vol. 1, no. 4, pp. 353-372, 1994.
- [8] J. Teo and H. A. Abbass, "Neuro-Morpho Evolution: What will happen if our body is not symmetric?," *Australian Conference on Artificial Life*, pp. 261-275, 2003.
- [9] H. Lipson and J. B. Pollack, "Automatic design and manufacture of robotic lifeforms," *Nature*, vol. 406, pp. 974-978, 2000.
- [10] M. Gregor, J. Spalek and J. Capak, "Use of context blocks in genetic programming for evolution of robot morphology," *ELEKTRO*, pp. 286-291, 2012.
- [11] L. M. Howard and D. J. D'Angelo, "The GA-P: A genetic algorithm and genetic programming hybrid," *IEEE Expert*, vol. 10, no. 3, pp. 11-15, 1995.
- [12] W. P. Lee, J. Hallam and H. Lund, "A hybrid GP/GA approach for co-evolving controllers and robot bodies to achieve fitness-specified tasks," *Evolutionary Computation*, pp. 384 - 389, 1996.
- [13] H. Kim and H. Yamakawa, "Multi-objective optimization for number of joints and lengths of multi-jointed robot arm," *Innovative Engineering Systems*, pp. 196 - 200, 2012.
- [14] M. Oliveira, C. P. Santos, L. Costa, V. Matos and M. Ferreira, "Multi-objective parameter CPG optimization for gait generation of a quadruped robot considering behavioral diversity," *Intelligent Robots and Systems*, pp. 2286 - 2291, 2011.
- [15] J. Brest, S. Greiner, B. Boskovic, M. Mernik and V. Zumer, "Self-adapting control parameters in differential evolution: A comparative study on numerical benchmark problems," *IEEE Transactions on Evolutionary Computation*, vol. 10, no. 6, pp. 646 - 657, 2006.

A Study of Drift Force on Submerged Body in X4-AUV Development

Safwan Bin Mohd Rawi and Zainah Md Zain

Robotics and Unmanned System (RUS) Research Group, Faculty of Electrical & Electronic Engineering,
 Universiti Malaysia Pahang, Pekan, 26600 Pahang, Malaysia
 (E-mail: safwanrawi@gmail.com, zainah@ump.edu.my)

Abstract—Autonomous Underwater Vehicles (AUVs) are robots able to perform tasks without human intervention (remote operators). Research and development of this class of vehicles are growing, due to the excellent characteristics of the AUVs to operate in different situations. Therefore, this study aims to analyze the drift force over different geometric configurations of an AUV hull, in order to reduce the drag force on the body. It is important to design an AUV with minimizing the drag forces acting on the hull to make AUV cruising smoothly. We also simulate the drift force for our X4-AUV ellipsoidal shape to compare the results with other hull shape.

Keywords—Ellipsoid, AUV, Drift force, Slenderness ratio

1. Introduction

An Autonomous Underwater Vehicle, or AUV, is defined as a robot which travels underwater without physical communication with the land and without the necessity of the human operator. The AUVs are included in the group of Unmanned Underwater Vehicles, better known as UUVs (see Figure 1). During the last years, several AUVs have been developed and researches in the area are becoming more frequent, due to the extremely favorable characteristics that these robots have, like the ability to operate autonomously in hostile environments, such as unexplored areas, enemy water territories (in wartime), contaminated or deep water areas, etc. All these features make the use of AUVs very interesting for military, scientific and industrial sectors.

Most existing AUVs use batteries as an energy source for the propulsion system. The high value of drag force generated during the displacement of the robot increases the energy consumption of the system and therefore the AUV autonomy will be lowered, which is undesirable for any engineer.

In order to design any AUV, the major design aspects that need to be considered are identifying hull design, propulsion, submerging and electric power. The most basic characteristic about an AUV is its size and shape. The basic shape of the AUV is the very first step in its design and everything else must work around it. The shape of the AUV determines its application, efficiency and range.

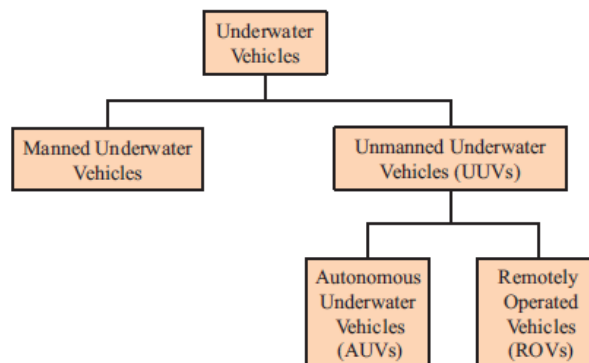


Fig. 1. Types of underwater vehicles

There have been a wide variety of AUVs in size and shape such as spherical hull shape, torpedo and non-torpedo shape, streamlined shape etc. as shown in Figure 2 – 8 [1][2][3]. It is important to design an AUV with minimizing the drag forces acting on the hull to make AUV cruising smoothly.

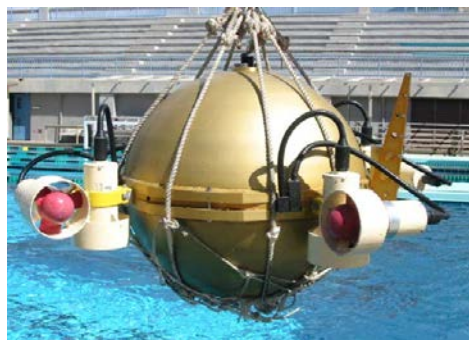


Fig. 2. ODIN spherical hull shape.

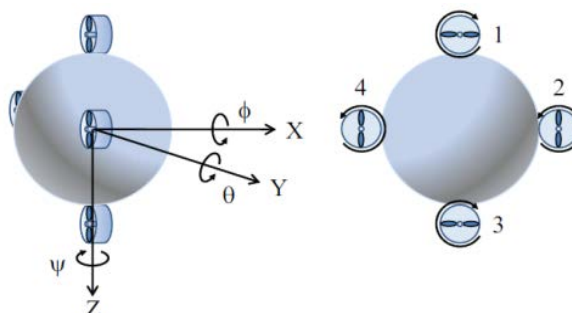


Fig. 3. X4-AUV with spherical hull shape.

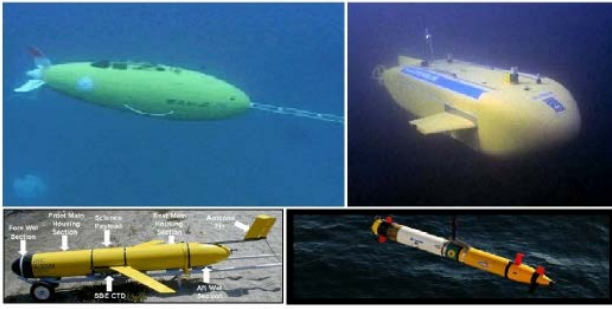


Fig.4. Torpedo shaped AUV.



Fig. 5. Non-torpedo shaped AUV.



Fig. 6. Caption AUV with laminar flow body.

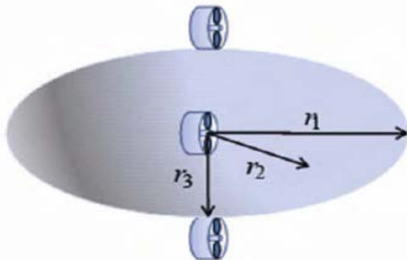


Fig. 7.X4-AUV with an ellipsoidal body that mostly closes to a streamlined shape

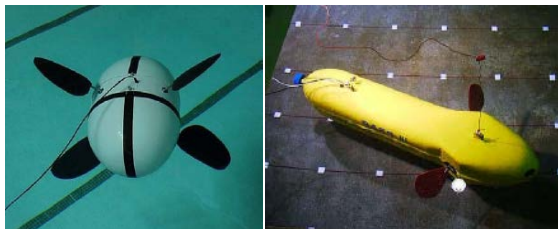


Fig. 8. Biomimetic robots Bass3 (left) and Pilot Fish (right)

2. Drift Force on Submerged Sphere

Spherical coordinates are used in the formulation of the drift forces of the sphere. The potential function is obtained in the spherical coordinates which is then differentiated to generate velocity components. The

velocity squared term is further simplified and an integrand is obtained in terms of hyperbolic and trigonometric functions of ka , θ and μ . The graphs for the dimensionless force are developed for different values of ka which can be used to calculate the second order drift forces for a rigid sphere [4].

Based on the derived drift force formula for a sphere in [4], we simulate the ODIN model where it was the first version of AUV that developed by using a sphere shape to get the drift force for this AUV by referring to the parameters in Table 1.

Table 1 ODIN parameters [7].

Parameter	Value & Description
r	0.3 m radius of the vehicle
m	125 kg mass of the vehicle
g	$9.8 \frac{m}{s^2}$ acceleration of gravity
I_x	$\frac{2}{5}mr^2 \text{kgm}^2$ moment of inertia for a sphere
z_g	0.05 m vertical location of the CG
ρ	$1000 \frac{kg}{m^3}$ density of water
K_p	0kgm^2 hydrodynamic added moment of inertia

The squared velocity results in the sphere submerged in water with different water depths have been calculated keeping the ratio of depth of submergence to the radius as constant parameter. The results showed (Figure 9) that as the water depth increases the mean drift force decreases. Also, drift force peaks for intermediate values of ka showing an almost similar trend as shown by hemisphere. The higher values of ka the force almost approaches to zero. Also, it is seen that as the sphere comes closer to the surface the drift force increases as can be seen from the plot.

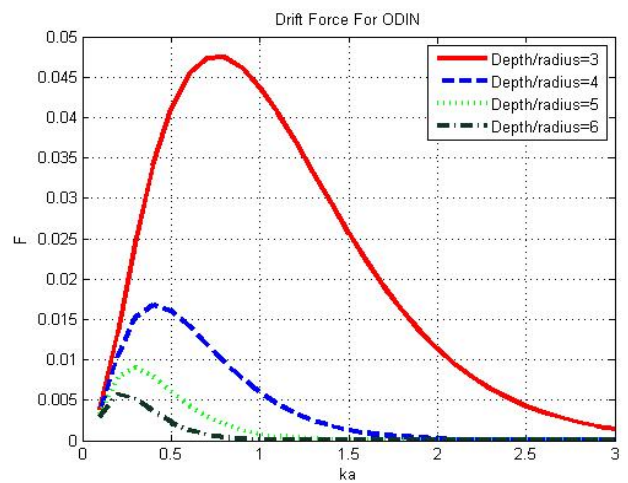


Fig. 9. Drift force for ODIN.

3. Drift Force on Submerged Ellipsoid

Ellipsoid shape has three major axes to be considered as shown in Fig. 10. Nowadays, most of the AUV body design is based on torpedo or ellipsoidal shape.

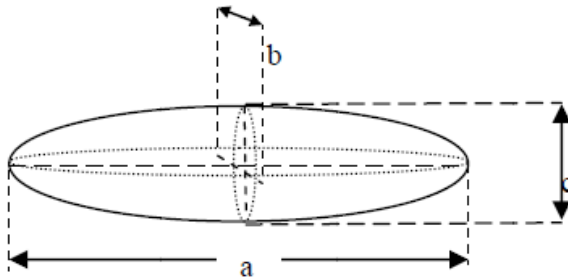


Fig. 10. Ellipsoid geometry

In order to prove and demonstrate the theory for the ellipsoid, an ellipsoid AUV model and its parameters as shown by Wang et al [5] will be implemented to the derived drift force formula for ellipsoid proposed in [4]. The formula implementations were derived based from the Wang et al AUV [5] length in the horizontal plane and longitudinal plane. The dimension value also considered where finally the ratio of value a, b, and c obtained. This ratio value can be applied to any types of ellipsoid body for obtaining the drift force. Based on Figure 11:

- **Horizontal plane:** 1458.54 cm^2 ($\pi ab/4$) used to obtain the minor axial length.
- **Longitudinal plane:** 9040 cm^2 ($\pi ac/4$) used for the vertical minor axial length.
- The maximum dimension=200, so assuming $a=200$ and by equating the areas, value of $b=92.7 \text{ cm}$ and $c=57.56 \text{ cm}$
- Ratio of $a : b : c = 1 : 0.4635 : 0.2878$. The maximum value of $a : b : c = 1 : 0.5 : 0.3$.

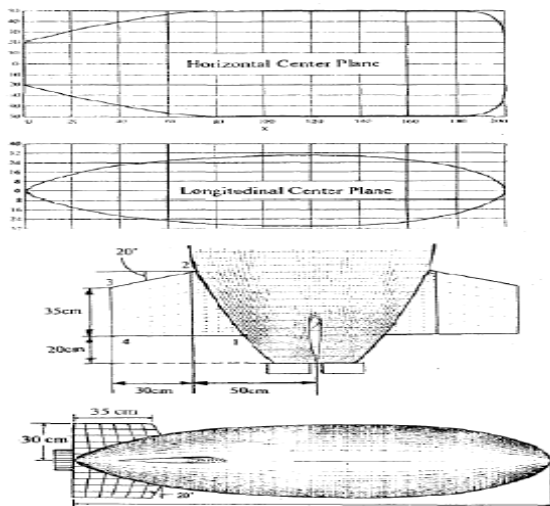


Fig. 11. AUV model as shown by Wang et al [5].

Based on the slenderness ratio given in [5], we simulate the model in [4] to calculate the drift force for our ellipsoidal X4-AUV as shown in Figure 12.

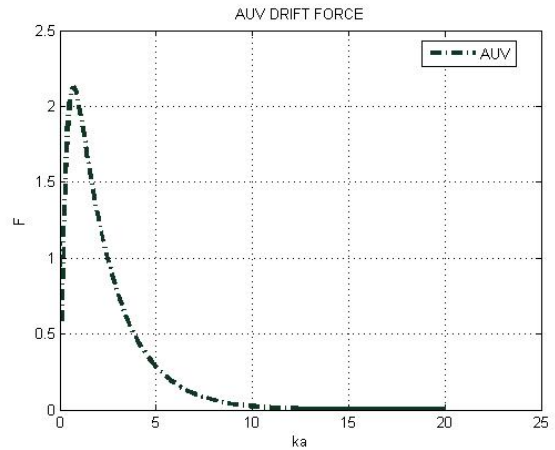


Fig. 12. X4-AUV ellipsoid version drift force ($a:b:c = 0.99:0.19:0.199$) using Wang Model

Then, to illustrate a real life example, an example of a fish's body (streamlined shape) is considered which is approximated as an ellipsoid. The drift forces acting over body of different fishes have been shown in the graph (Figure 14), which proves that slender body of a fish face very less load as compared to other structures. The fish's body has been assumed as an ellipsoid with the major axes $a=0.93L$, $b=0.195L$ and $c=0.112L$, where L is the overall length of the fish. This is a reasonable assumption for the dimension for dorsal = a , lateral = b , and head aspect = c , but less accurate with tail aspect of fish [4].

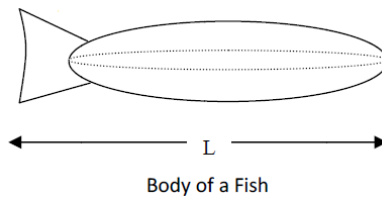


Fig. 13. Length of fish.

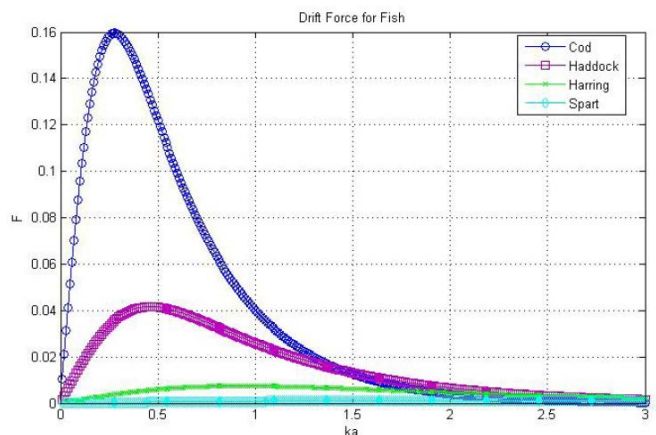


Fig. 14. Drift force for fish

The different fishes are considered for analyses with their respective overall lengths are given in Table 1 [4]. It can be concluded from the graph that the longest fish is

having a maximum force which is expected as the longest fish will have the maximum surface area for the same ratio of the axes.

Table 1 Geometrical approximation of different fishes

Fish	Length
Cod	120 cm
Haddock	60 cm
Herring	30 cm
Sprat	15 cm

The drift force on ellipsoidal X4-AUV using the slenderness ratio for ellipsoid based on fish characteristic is shown in Figure 15.

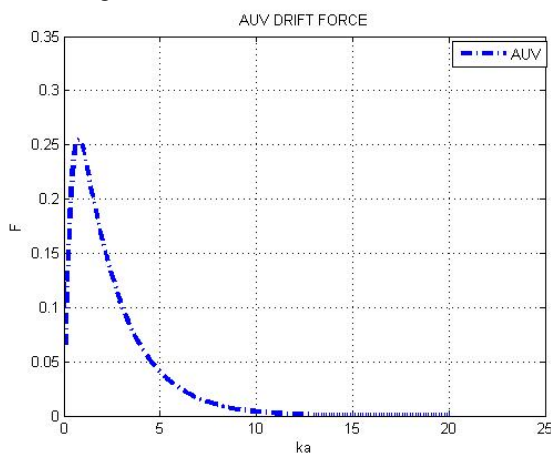


Fig. 15. X4-AUV ellipsoid version using fish behavior drift force ($a=0.93L$, $b=0.1995L$, and $c=0.112L$).

4. Discussion

An AUV with spherical hull shape design facing with the drag forces against a stream are relatively higher than other AUVs. It is proven that AUV with ellipsoidal body that mostly closes to a streamlined shape can reduce the drag force on the body. In order to provide the minimum drag to the maximum volume AUV, the AUV were tended to be designed with the guide of slenderness ratio where the value of length divided by the diameter. The best ratio for the AUV body development were in the range of 5 to 8, mimicking in some respects naval torpedoes and aircraft drop tanks to provide the maximum volume for minimum drag. In the ellipsoid approach, the best slenderness ratio that needs to be followed is 5 where this will improve the performances and the efficiency to the fullest [4]. Long and slender shapes are therefore better for frontal drag. The comparison of the slenderness ratio between models which discussed in this paper is shown in Table 2.

From Figure 12 and Figure 15, we can see that the simulation on X4-AUV with an ellipsoidal shape which follow slenderness mimic to the fish give the lower drag force compared to the slenderness ratio proposed by the

Wang where the calculation for the drift force based on the equivalent area method.

Table 2 Slenderness ratio of AUV models.

Model	Slenderness ratio (l/d)
ODIN (Sphere)	30cm/30cm=1
Wang et al AUV (Ellipse)	200cm/92.7cm=2.2 (major) 200cm/57.56cm=3.5 (minor)
X4-AUV (Ellipsoid)	100cm/20cm=5

Conclusion

Minimum drag is one of the important parameters of the AUV with respect to the shape and size. From this study, the streamlined shape of the AUV hull can reduce the drag force on the body. Therefore, it is important to know the best value for the slenderness ratio to enable the shape and size of the ellipsoid mimic to the biological fish which can give the minimum drag force.

Future works

Based on this study, we will design and develop an X4-AUV with an ellipsoidal shape by choosing the appropriate slenderness ratio to get the streamlined body that close to the slenderness ratio of biomimetic ellipsoid (fish).

Acknowledgement

This research is supported by Universiti Malaysia Pahang under UMP RDU 130380 research grant.

References

- [1] Z. M. Zain, "Control of an Underactuated X4-AUV with Four Thrusters", PhD Thesis, Okayama University, Japan, 2012.
- [2] SIE 3090 Guidance, Navigation and Control, Monday 10th March 2003.
- [3] F. E. Fish et al., "Conceptual Design for the Construction of a Biorobotic AUY Based on Biological Hydrodynamics", in Proc. of the 13th Int. Sym. of Unmanned UntetheredSubnwsrrible Technology, New Hampshire, 2003.
- [4] A. Gupta, "Steady Wave Drift Force on Basic Objects of Symmetry", Master Thesis, TexasA&M University, 2008.
- [5] J. P. Wang, F. C Chung, J. Guo J, "On the Prediction of Maneuverability of the Autonomous Underwater Vehicle, AUV-HM1. In: International Symposium on Underwater Technology, Tokyo, 1988: 185-190.

Backstepping Approach for Underactuated Systems

Nur Fadzillah Harun and Zainah Md. Zain

Robotics and Unmanned System (RUS) Research Group, Faculty of Electrical & Electronic Engineering,
Universiti Malaysia Pahang, Pekan, 26600 Pahang, Malaysia
(E-mail: nurfadz@gmail.com)

Abstract - Control of underactuated systems usually required nonlinear technique because it cannot be stabilize with usual smooth, time-invariant and state feedback controller. Thus, backstepping approach is considered for stabilize underactuated systems, which the system is stabilized according to Lyapunov stability theory. This paper reviews the backstepping control method toward underactuated system.

Keywords - Underactuated systems, Backstepping, nonlinear control.

1. Introduction

Underactuated systems refer to those systems with less number of control or inputs than numbers of degrees of freedom (DOFs). The "underactuation" property of underactuated systems is due to the following reasons; dynamics of the system, by design for reduction of the cost or some practical purposes, actuator failure, and imposed artificially to create complex low-order nonlinear systems for the purpose of gaining insight in control of high-order underactuated [1].

Underactuation arises out of the need to reduce cost and saving fuel by fewer actuators is used. The lighter and compact structure of system also gives an advantage in positioning and save space. It also increase the reliability of the system in case of failure; if one actuators fails, other actuator can still achieve the objective of the system [2].

Application of underactuated systems are plenteous in our life, for example in robotics and vehicles (e.g. Wheeled Mobile Robot (WMR), walking robots, the Acrobot, the Pendubot, Wheeled Inverted Pendulum (WIP), Unmanned Air Vehicle (UAV), Vertical Take-Off and Landing (VTOL), helicopters, Autonomous Underwater Vehicle (AUV) and surface vessel).

Controlling underactuated systems has been in active research because it concern fundamentally nonlinear control problems which requires novel ideas and technique. The dynamics of underactuated systems may contain feedforward nonlinearities, non-minimum phase zero dynamics, nonholonomic constraints, and other properties that place this systems in nonlinear control research [3]. Nonlinear control is the area of control theory which deals with systems that are nonlinear, time-variant or both and backstepping method is one of the nonlinear control techniques that can be used to control underactuated systems.

2. Control Problem for Underactuated Systems

Control inputs of underactuated systems are less than the number of the states to be controlled and arise often in nonholonomics systems with nonintegrable constrains. There are two types of nonholonomic constraints: one is the first-order classical nonholonomic constraints and the other is the second-order nonholonomic constraints. The first-order nonholonomic constraints are defined as constraints on the generalized coordinates and velocities. The second-order nonholonomic constraints are defined as those on the generalized coordinates, velocities, and accelerations [3]. Nonholonomic constraints arise in two kinds of situations: one is bodies in contact with each other which roll without slipping and the other is conservation of angular momentum in a multibody system [4]. The problem of stabilizing this systems is a big issue, as it has been proved by Brockett [5] that the nonholonomic control systems with restricted mobility cannot be stabilized to a desired configuration (equilibrium) using a smooth time-invariant state feedback law. Nonholonomic constraints arise in a number of ways and in various underactuated systems and applications such as WMR, Space robots, underwater vehicles and aerospace vehicles. Therefore, for underactuated nonholonomics system, nonlinear control method such as backstepping is used because the nonholonomic constrains are inherently nonlinear.

3. Backstepping Method

3.1 Backstepping

In the beginning of 1990s, a new approach called "backstepping" was developed by Krstic, Kokotovic and Kanellakopoulos [6] for stabilizing controls for a special class of nonlinear dynamical systems. Backstepping is a recursive Lyapunov-based scheme for the class of "strict-feedback" systems. In fact, when the controlled plant belongs to the class of systems transformable into the parametric strict-feedback form, this approach guarantees global or regional regulation and tracking properties. An important advantage of backstepping is that it has the flexibility to avoid cancellations of useful nonlinearities and achieve stabilization and tracking. Another advantage of the backstepping design method is that it provides a systematic procedure to design stabilizing controllers, following a step by step algorithm.

To give an idea about backstepping method, consider the following strict-feedback system:

$$\dot{x}_1 = x_1 + x_2 \quad (1)$$

$$\dot{x}_2 = u \quad (2)$$

where

x_1, x_2 are system states and u is control input

x_2 is considered as a virtual controller to x_1 in Eq.(1).

Eq. (1) rewrite as follows:

$$\dot{x}_1 = x_1 + v \quad (3)$$

Eq. (3) is a first order system with v as a control input.

Then, Lyapunov function is applied

$$V_1 = \frac{1}{2}x_1^2 \quad (4)$$

Accordingly \dot{V}_1 is

$$\dot{V}_1 = x_1\dot{x}_1 = x_1(x_1 + v)$$

Let $v = -2x_1$, then \dot{V} becomes,

$$\dot{V}_1 = -x_1^2 < 0 \forall x \neq 0$$

It means that x_1 decay exponentially asymptotically to the origin when ($x_2 = v = -2x_1$). This is a first step in the design procedure. The second is by defining the following output.

$$z_1 = x_2 - v = x_2 + 2x_1 \quad (5)$$

Now Eq. (1) is rewritten with replacing x_2 by the new state z_1 according to the transformation Eq. (5). Namely,

$$x_2 = z_1 - 2x_1 \quad (6)$$

Therefore Eq. (1) becomes:

$$\dot{x}_1 = -x_1 + z_1 \quad (7)$$

Differentiate z_1 in Eq. (5) with the transformation (Eq. (6)) to get,

$$\begin{aligned} \dot{z}_1 &= \dot{x}_2 + 2\dot{x}_1 = u + 2(x_1 + x_2) \\ &= u + 2(x_1 + z_1 - 2x_1) \\ &= u + 2z_1 - 2x_1 \end{aligned}$$

The next step is to write the total Lyapunov function as follows:

$$V = V_1 + \frac{1}{2}z_1^2 = \frac{1}{2}x_1^2 + \frac{1}{2}z_1^2 \quad (8)$$

Accordingly \dot{V} is,

$$\begin{aligned} \dot{V} &= x_1\dot{x}_1 + z_1\dot{z}_1 = x_1(-x_1 + z_1) + z_1(u + 2z_1 - 2x_1) \\ &= -x_1^2 + x_1z_1 + z_1(u + 2z_1 - 2x_1) \\ &= -x_1^2 + z_1(u + 2z_1 - x_1) \end{aligned}$$

If

$$u = -3z_1 + x_1 \quad (9)$$

Then \dot{V} becomes,

$$\dot{V} = -x_1^2 - z_1^2$$

\dot{V} is negative definite and thus z_1 and x_1 regulated to the origin $z_1 = x_1 = 0$ asymptotically.

Finally the control law which will regulate x_1 and x_2 to the origin asymptotically via the backstepping design method is:

$$u = -3(x_2 + 2x_1) + x_1 = -5x_1 - 3x_2 \quad (10)$$

The backstepping approach determines how to stabilize the x_2 subsystem using z_1 and then proceeds with determining how to make the next state z_2 drive z_1 to control and stabilize x_3 . Hence, the process "steps backward" from x out of the strict-feedback form system until the ultimate control u is designed.

3.2 Lyapunov Theory

Various types of stability may be discussed for the solutions of differential equations describing dynamical systems. The most important type is that concerning the stability of solutions near to a point of equilibrium and Lyapunov theory considered about it. Lyapunov theory is named after Aleksandr Lyapunov, a Russian mathematician. Lyapunov consider the modifications necessary in nonlinear systems to the linear theory of stability based on linearizing near a point of equilibrium.

Consider a time invariant system with state x and dynamics $\dot{x} = f(x)$. The stability of the system can be proved using Lyapunov. Lyapunov function $V(x)$ has to be positive definite in a region Γ near $x = 0$.

Examined \dot{V}

$$\dot{V}(x) = \frac{\delta V(x)}{\delta t} = \frac{\delta V(x)}{\delta x} \frac{\delta x}{\delta t} = \frac{\delta V(x)}{\delta x} f(x) \quad (11)$$

The Lyapunov theory states that:

- I. If $\dot{V}(x)$ is negative semidefinite in the region Γ , then the solution is stable.
- II. If $\dot{V}(x)$ is negative definite in the region Γ , then the solution is asymptotically stable.
- III. If $\dot{V}(x)$ is positive definite and radially unbounded for all x and if $\dot{V}(x)$ is negative definite for all x , then the solution is globally asymptotically stable

where:

- Positive definite if $V(0) = 0$ and $V(x) > 0$ with $x \neq 0$.
- Positive semidefinite if $V(0) = 0$ and $V(x) \geq 0$ with $x \neq 0$.
- Negative semidefinite if $-V(x)$ is positive semidefinite.
- Radially unbounded if $V(x) \rightarrow \infty$ as $|x| \rightarrow \infty$.

4. Examples of Underactuated Systems Applied Backstepping Method

Although backstepping theory has rather short history, numerous practical applications can be found in the literature. Thus fact indicates that a need for nonlinear design methodology handling a number of practical problems. In this section, we review some publication of underactuated systems applied backstepping method.

4.1 Mobile Robots

Obviously, mobile robots have a variety of applications and besides the relevance in applications, the problem of control mobile robot attracted many researchers. Generally mobile robot difficulty divided by three basic problems [7]; tracking reference trajectory, following a path, and point stabilization. In practical, most mobile robot can be transformed into chained form in order to make designing controller more easily. Recursive backstepping control schemes for chained forms of mobile robot have been studied by past researches [8,9].

A discontinuous time invariant controller with backstepping approach presented [9]. The dynamical model of a car-like is an example of underactuated systems with 5 DOF, 2 control inputs and 2 velocities constrains [9].

Dynamics of car [9] written as:

$$\begin{aligned} \dot{x} &= \psi r \cos \theta \\ \dot{y} &= \psi r \sin \theta \\ \dot{\theta} &= \psi \frac{r}{\rho} \tan \theta \\ \ddot{\psi} &= \tau_1 \\ \ddot{\phi} &= \tau_1 \end{aligned} \quad (12)$$

where r is the radius of the wheel.

System in Eq. (12) have been transformed into chained form

$$\begin{aligned} \dot{x}_1 &= v_1 \\ \dot{x}_2 &= v_2 \\ \dot{x}_3 &= x_2 v_1 \\ \dot{x}_4 &= x_3 v_1 \end{aligned} \quad (13)$$

where $(x_1 \dots x_4)^T \in \mathfrak{R}^4$ are the states systems of the system and $(V_1, V_2) \in \mathfrak{R}^2$ are the control inputs.

In order to apply backstepping approach, consider the following change of coordinates $z_i = x_{n-i+1}$, $1 \leq i \leq 4$. System in Eq. (13) becomes

$$\begin{aligned} \dot{z}_1 &= z_2 v_1 \\ \dot{z}_2 &= z_3 v_1 \\ \dot{z}_3 &= v_2 \\ \dot{z}_4 &= v_1 \end{aligned} \quad (14)$$

Let used state feedback $v_1 = -k_4 z_4$, where k_4 is a positive constant in order to guarantee the exponential convergence.

$$\begin{aligned} \dot{z}_1 &= -k_4 z_4 z_2 \\ \dot{z}_2 &= -k_4 z_4 z_3 \\ \dot{z}_3 &= v_2 \\ \dot{z}_4 &= -k_4 z_4 \end{aligned} \quad (15)$$

Now the problem consists of finding a control law v_2 , if the initial state belongs to the set

$\Omega = \{(z_1(0), z_2(0), z_3(0), z_4(0))^T \in \mathfrak{R}^4 / z_4(0) = x_1(0) \neq 0\}$. The whole state of the closed loop system remains bounded and converges exponentially to zero. The design procedure is done in 3 steps.

A. Step 1

Here, z_2 is viewed as virtual control variable and Lyapunov function is considered

$$v_1 = \frac{1}{2k_4} z_1^2 \quad (16)$$

Derivative is given by

$$\dot{V}_1 = -z_1 z_2 z_4 \quad (17)$$

Consider using the following virtual control

$$\eta_1 = k_1 \frac{z_1}{z_4} \quad (18)$$

where k_1 is a positive constant and substitute z_2 by η_1 .

Eq. (18) become

$$\dot{V}_1 = -k_1 z_1^2$$

B. Step 2 and Step 3

Designing procedure in step 1 finished. For Step 2 and Step 3, same procedures are taken with considering Lyapunov function and new variable ε_2 and ε_3 been discovered.

Based on simulation results [9], we can conclude that $(z_1, \varepsilon_2, \varepsilon_3)^T$ is bounded and tends to zero when t approaches infinity. Therefore $z_i \rightarrow \eta_{i-1}$, $i=2, 3$ when $t \rightarrow \infty$. To guarantee the boundedness and the convergence to zero of $(z_2, z_3)^T$, the boundedness and the convergence of $(\eta_1, \eta_2)^T$ must zero.

Since $\eta_1 = k_1 \frac{z_1}{z_4}$ and z_4 assumed to be different from zero, then η_1 is bounded and converges to zero as $t \rightarrow \infty$. On the other hand, $\eta_2 = -z_1 + \frac{k_2 \varepsilon_2}{z_4} - \frac{\eta_1}{k_2 z_2}$, this function is bounded and converge to zero if $\dot{\eta}_1$ also bounded and converge to zero. $\dot{\eta}_1$ can be directly calculated as:

$$\dot{\eta}_1 = k_1 \frac{\dot{z}_1 z_4 - \dot{z}_4 z_1}{z_4^2} \quad (19)$$

Finally, it conclude that if $z_4(0) = x_1(0) \neq 0$ then

- I. The whole state remains in Ω since z_4 and then x_1 decays to zero.
- II. The state trajectory of the closed loop system is bounded and converges to zero.

Results [9] demonstrate the validity of proposed control, it smooth everywhere except at $x_1 = 0$. The discontinuity involved in the control not very restrictive since it occurs just for $x_1(0) = 0$.

4.2 Quadrotor

Quadrotor aerial robot is one of UAVs with highly nonlinear, multivariable, strongly coupled and it have 6 DOF and 4 actuators [10]. A nonlinear control strategy implemented in order to stabilize quadrotor aerial robot at hover. The altitude of the quadrotor is stabilized using vertical force input u_1 while rotational control using backstepping based PID which the inputs is u_2, u_3, u_4 . For rotational control, backstepping based PID is implemented. The angles and time derivatives of rotational subsystem not depend on translation components but the translations depend on the angles. Rotational control keeps the 3D orientation of the quadrotor aerial robot to the desired value. Roll and pitch angles are usually forced to zero which permits hovering flight. The rotational controller task is to compensate the initial error, stabilize roll, pitch and yaw angles and maintain them at zero. Rotational dynamics of quadrotor [10] written as:

$$J_x \ddot{\phi} = \dot{\theta} \dot{\psi} (J_y - J_z) + I(T_4 - T_2) + \sum_{i=1}^4 (-1)^{i+1} R_{xi} - h \sum_{i=1}^4 D_{yi} \quad (20)$$

$$J_y \ddot{\theta} = \dot{\phi} \dot{\psi} (J_z - J_x) + I(T_3 - T_1) + \sum_{i=1}^4 (-1)^{i+1} R_{yi} + h \sum_{i=1}^4 D_{xi} \quad (21)$$

$$J_z \ddot{\psi} = \begin{bmatrix} \dot{\phi} \dot{\theta} (J_x - J_y) + \sum_{i=1}^4 (-1)^i Q_i + \\ \left[(D_{x2} - D_{x4}) + (D_{y3} - D_{y1}) \right] I \end{bmatrix} \quad (22)$$

where R_x, R_y and $h(D_x), h(D_y)$ represent rolling and drag moments due to forward and sideward flight respectively, $(D_{x2} - D_{x4})$ and $(D_{y3} - D_{y1})$ represent drag force unbalance in forward and sideward flight respectively.

The roll tracking error be defined as

$$e = \phi - \phi_d \quad (23)$$

The first error in the backstepping design is

$$z_1 = K_1 e + K_d \int edt$$

where K_1 and K_2 are positive tuning parameters and $\int edt$ represents integral of roll error.

Lyapunov theorem is considered by using the Lyapunov function z_1 positive definite and time derivative negative semi definite

$$V_1 = \frac{1}{2} z_1^2 \quad (24)$$

Derivative is given by

$$\dot{V}_1 = z_1 \dot{z}_1 = z_1 (K_1 \dot{\phi} - K_1 \dot{\phi}_d + K_2 e) \quad (25)$$

There is no control input in Eq. (25). Then, consider $\dot{\phi}$ as virtual control. Then the desired virtual control $(\dot{\phi})_d$ is defined as,

$$(\dot{\phi})_d = \dot{\phi}_d - \frac{K_2}{K_1} e - \frac{C_1 z_1}{K_1} \quad (26)$$

where C_1 is positive constant for increasing the convergence speed of the roll tracking loop.

Here, the virtual control $\dot{\phi}$ represents the roll rate of quadrotor and has its own error given by

$$z_2 = \dot{\phi} - (\dot{\phi})_d = \frac{1}{K_1} [\dot{z}_1 + c_1 z_1] \quad (27)$$

Augmented Lyapunov function for second step is

$$V_1 = \frac{1}{2} z_1^2 + \frac{1}{2} z_2^2 \quad (28)$$

Then, derivation of Eq. (28) is defined. After that, PID is applied into u_2, u_3, u_4 as inputs for systems.

Based on simulation results [10], the backstepping based PID controller effectively controls roll, pitch and yaw angles of quadrotor aerial robot in less 7 seconds. This is a novel control strategy which the integral of the tracking error considered in the first step of backstepping procedure and applied to rotational subsystem of the quadrotor aerial robot. The results indicate effectiveness of the proposed control strategy for quadrotor aerial robot.

4.3 Marine Vehicles

Y. Han et.al [11] proposed control law of dynamic inversion combining with backstepping aiming at nonlinear planning force existing in supercavitating vehicle tail. Dynamic inverse control is applied as control inner-loop towards high speed underwater vehicles meanwhile backstepping is adopted as control out-loops in order to guarantee global stability of the system. Mathematical model of vehicles longitudinal model [11] written as:

$$\begin{aligned} \dot{z} &= w - V\theta \\ \dot{w} &= \frac{(C_1 - C_2)}{(MV)} w + \frac{(C_1 L_c - C_2 L_f)}{(MV)} q + \frac{C_1}{M} \delta_e + \frac{C_2}{M} \delta_c + \\ &\quad g + \frac{C_p}{M} F_{plane} \\ \dot{\theta} &= q \\ \dot{q} &= \frac{(-C_1 L_c + C_2 L_f)}{(I_{yy} V)} w + \frac{(-C_1 L_c^2 + C_2 L_f^2)}{(I_{yy} V)} q - \frac{C_1}{I_{yy}} L_c \delta_e \\ &\quad - \frac{C_2}{I_{yy}} L_f \delta_c - \frac{C_p}{I_{yy}} L_f F_{plane} \end{aligned} \quad (29)$$

where :

V is the velocity of body center, and assumed to be constant. L is the vehicle length, w is the vertical speed of body, θ is pitch angle and q is pitch rate. δ_c is a cavitator deflection angle and δ_e is an elevator deflection angle. Considering the existence of planning force F_{plane} in vehicle tail.

Define $e_z = Z - Z_d$, $X_Z = [e_z \quad \dot{e}_z \quad \ddot{e}_z]$ and Z_d is an order signal of vehicle depth, they can be written as

$$\begin{cases} X_{z_1} = e_z \\ \dot{X}_{z_1} = \dot{e}_z = X_{z_2} \\ X_{z_2} = \ddot{e}_z = X_{z_3} = \ddot{z} - \ddot{z}_d \end{cases} \quad (30)$$

The error variables is defined as

$$\begin{cases} Z_{z_1} = X_{z_1} \\ Z_{z_2} = X_{z_2} - \alpha_{z_1} (X_{z_1}) \end{cases} \quad (31)$$

Derivation for z_{z_1} is given by

$$\dot{Z}_{z_1} = X_{z_2} = -CZ_{z_1} + CX_{z_1} + X_{z_2} \quad (32)$$

For Z_{z_1} , defined Lyapunov function $V_{z_1} = \frac{1}{2}Z_{z_1}^2$ and choose $\alpha_{z_1} = -CZ_{z_1}$, therein $C > 0$, so

$$\begin{cases} \dot{Z}_{z_1} = -CZ_{z_1} + Z_{z_2} \\ \dot{V}_{z_1} = -C_1Z_{z_1}^2 + Z_{z_1}Z_{z_2} \end{cases} \quad (33)$$

$$\dot{Z}_{z_2} = X_{z_3} - \frac{\delta\alpha_{z_1}}{\delta Z_{z_1}} \dot{Z}_{z_1} = X_{z_3} + J_{z_2}(Z_{z_1}, Z_{z_2}) \quad (34)$$

For Z_{z_1} and Z_{z_2} , Lyapunov function is defined as

$$V_{z_2} = \frac{1}{2}Z_{z_1}^2 + \frac{1}{2}Z_{z_2}^2, \text{ therefore} \\ \dot{V}_{z_2} = \dot{V}_{z_1} + \dot{Z}_{z_2}Z_{z_2} = -C_1Z_{z_1}^2 + Z_{z_1}Z_{z_2} + \dot{Z}_{z_2}Z_{z_2} \quad (35)$$

Then, choose $\dot{Z}_{z_2} = -C_2Z_{z_2} - Z_{z_1}$ therein $C_2 > 0$, so

$$\dot{V}_{z_2} = -C_1Z_{z_1}^2 - C_2Z_{z_2}^2 < 0 \quad (36)$$

Based on Lyapunov theory, Eq. (33) and Eq. (34) is gradually stable. Simulation results [11] show vehicle can track order signal quickly and vertical speed of vehicle, pitch angle, cavitator deflection angle, elevator deflection angle approach respective stable value after the body in stable state. Results indicate that dynamic inversion control based backstepping for underwater supercavitating vehicles longitudinal motion has favorable control and guarantee vehicles can move stable.

4.4 Inverted Pendulum

Obviously the rail cart type for WIP is a one dimensional control structure. The interesting and challenging problem is how to control a WIP which the cart is no longer on a guide rail. The dynamic characteristics of WIP are nonlinear and precise models are difficult to obtain. The adaptive output recurrent cerebellar model articulation control (AORCMAC) backstepping tracking control system has been proposed [12]. The AORCMAC used to mimic an ideal backstepping control, and the compensate controller is designed to recover the residual approximation error. From the simulation results, the tracking errors converge quickly, and the robust control characteristics of the proposed control scheme can be clearly observed under the condition of external disturbances and various reference trajectories. The AORCMAC backstepping system achieves a good control performance for the WIP system.

5. Conclusion

This paper reviews the backstepping control for underactuated systems. Obviously, backstepping control method effective in designing stabilized controller and achieved stabilization for underactuated systems. The key idea in backstepping is let certain states act as a ‘virtual control’ of others and the ability to avoid cancellations of useful nonlinearities and achieve stability and tracking. Based on examples given in section 4, all results indicate effectiveness of the backstepping control for underactuated systems although differential equations describing different dynamical systems.

Acknowledgement

The authors would like to thank Ministry of Higher Education (Kementerian Pengajian Tinggi), Malaysia for sponsoring this research through Exploratory Research Grant Scheme (ERGS) Grant No. RDU130613.

References

- [1] R. A. Soltan, “Coordinated Tracking Control and Obstacle Avoidance for Underactuated,” July, 2009.
- [2] M. Zainah, “Underactuated Control for an Autonomous Underwater Vehicle with Four Thrusters,” 2012.
- [3] M. W. Spong, “Underactuated Mechanical Systems,” in Lecture notes in control and information sciences, Control problems in robotics and automation, 1998.
- [4] “Nonholonomic Behavior in Robotic Systems,” vol. 317, pp. 317–354.
- [5] R. W. Brockett, “Asymptotic Stability and Feedback Stabilization,” in Differential Geometric Control Theory, 1983.
- [6] M. Krstic, I. Kanellakopoulos, and P. Kokotovic, Nonlinear and Adaptive Control Design, 1995.
- [7] O. J. Sordalen and C. Canudas de Wit, “Exponential Control Law for a Mobile Robot: Extension to Path Following,” 1993.
- [8] Z. Jiang and H. Nijmeijer, “A Recursive Technique for Tracking Control of Nonholonomic Systems in Chained Form,” 1999.
- [9] F. Mnif, “Recursive Backstepping Stabilization of a Wheeled Mobile Robot,” 2004.
- [10] A. Mian and W. Daobo, “Nonlinear Flight Control Strategy for an Underactuated Quadrotor Aerial Robot,” 2008.
- [11] Y. Han, X. Bi, and T. Bai, “Dynamic Inversion Control Based on Backstepping for Underwater High-Speed Vehicle,” in Proceedings of the World Congress on Intelligent Control and Automation (WCICA), 2010.
- [12] C.-H. Chiu, Y.-F. Peng, and Y.-W. Lin, “Intelligent Backstepping Control for Wheeled Inverted Pendulum,” Apr. 2011.

3D Image Construction Using Single LRF Hokuyo URG-04LX

Hendriyawan Achmad¹, Mohd Razali Daud²

^{1,2} Faculty of Electrical & Electronics Engineering, University Malaysia Pahang, Pekan, 26600, Malaysia
(E-mail: hendriyawanachmad@gmail.com¹, mrazali@ump.edu.my²)

Abstract – Nowadays researchers who focus on robotic vision technology are facing with greater challenges, where the 2D technology has many flaws in robot navigation. Using 3D technology, the robot is able to make a more detailed map navigation making it easier to carry out its mission. 3D image is obtained by using the method of fusion between the Hokuyo URG-04LX with 6-DOF IMU consists of acceleration sensor and gyro sensor. IMU sensor outputs are the angle, speed, and position in 3D. However, only the value of the angle is used in this work. To eliminate noise in the sensors output, two types of filters are used; the gaussian filter used on the output 2D LRF, while the complementary filter is used on the output of the IMU sensor. The proposed systems has successfully generated a valid 3D image according to the indoor testing that has been done.

Keywords – 3D image, Hokuyo URG-04LX, IMU sensor, filter.

1. Introduction

Mapping is the most important part of the mission of a mobile robot to recognize the surrounding environment[1], thus autonomous robots capable of moving and finding ways to avoid obstacles[2]. Mobile robot navigation technology is now increasingly sophisticated, with applying techniques of 2D and 3D navigation. Many studies on the implementation of 2D navigation for SLAM (simultaneous localization and mapping) to determine the current position of the robot in an area that has not been recognized previously[3]. However, current robotic missions more complex, not only to avoid obstacles and to find a way but also able to measure the dimensions of each part of the surrounding which is used in the context of path planning information.

There are many ways to get a 3D image[4] as the basis for the construction of a 3D map. Experiments that have been done in previous studies by using the 2D LRF and the 6-DOF IMU sensor[4][5][6][7]. IMU sensors provide 3-axis angle information are used to construct a 3D image and a 3-axis position information to build a 3D map.

This paper will discuss the methods of 3D image construction using the 2D LRF sensor Hokuyo URG-04Lx and 6-DOF IMU sensor.

2. System Description

As mentioned before, in this paper uses two types of sensors are used; 2D LRF sensors Hokuyo URG-04LX to measure distances [8] and 6-DOF IMU sensor MPU6050 which is composed from 3-DOF acceleration sensor and 3-DOF gyro sensor to measure angles [9]. Figure 1 shows a picture from the 2 sensors.

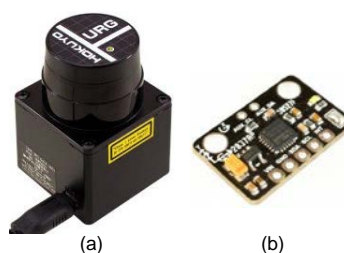


Fig. 1. (a) 2D LRF Hokuyo URG04LX (b) 6-DOF IMU sensor MPU6050

Since the 2D LRF sensor only capable of scanning in horizontal direction, a tilt mechanism with DC servo motor is used to enable the laser sensor scanning in vertical direction for $\pm 30^\circ$ range with 2° resolution. Changes in the angle will be measured by the IMU sensors, and used as input to establish 3D projection. Angle values are acquired from the fusion process between acceleration sensor and gyro sensor, at once as complementary filters that will be discussed in the next section. Arduino system is used for IMU sensor data acquisition and control DC servo tilt. Figure 2 shows a diagram of the system used in this work.

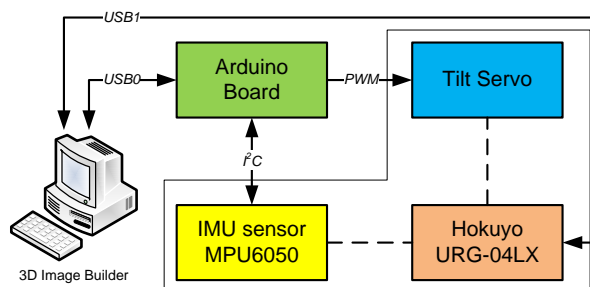


Fig. 2. Block diagram representation of control flow

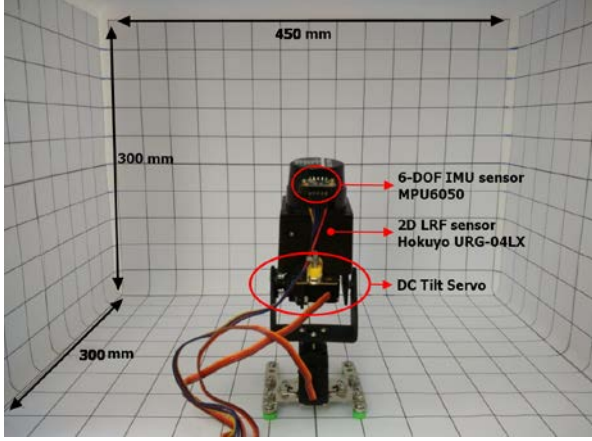


Fig. 3. Test Bed system for 3D space construction

On the other hand, Figure 3 shows the test bed used for the acquisition of 3D image data. In this work, Operational mode of 2D LRF sensor Hokuyo URG-04LX adjusted in accordance with the default, namely: horizontal scanning 240° with step 682 which gives the angular resolution 0.35° per step[10].

3. Geometry Invariant

By default, the number of valid data of Hokuyo URG-04LX are 682, start from 44th data to 725th data[10]. 2D projection of 682 data to form polar coordinates (r, θ) , thus must be converted into 2D Cartesian coordinates (x_n, y_n) as shown by figure 4.

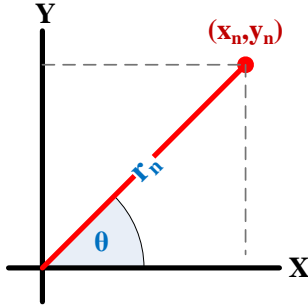


Fig. 4. Polar to cartesian projection

With the azimuth angle $(\theta) = \text{step-n} * 0.35^\circ$ respect to X axis. Equation (1) and (2) show conversion steps from polar into cartesian.

$$x_n = r_n * \cos(\theta) \quad (1)$$

$$y_n = r_n * \sin(\theta) \quad (2)$$

Thus obtained 2 matrix which are shown by equation (3) and (4).

$$X = [x_0, x_1, x_2, \dots, x_{681}] \quad (3)$$

$$Y = [y_0, y_1, y_2, \dots, y_{681}] \quad (4)$$

To construct a 3D image in addition to the X axis and Y axis, Z axis is needed. To obtain the value of Z, scanning depth is required for each measurement angle in the range $\pm 30^\circ$. Figure 5 shows the spherical polar coordinates are used for 3D projection..

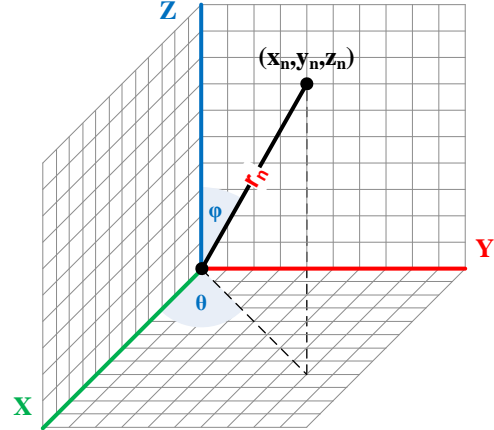


Fig. 5. Polar Spherical to 3D cartesian projection

Inclination angle (φ) obtained from IMU sensor and azimuth angle $(\theta) = \text{step-n} * 0.35^\circ$. Equation (5-7) show conversion steps from polar spherical into cartesian.

$$x_n = r_n * \cos(\theta) * \sin(\varphi) \quad (5)$$

$$y_n = r_n * \sin(\theta) * \sin(\varphi) \quad (6)$$

$$z_n = r_n * \sin(\theta) * \cos(\varphi) \quad (7)$$

Thus obtained 3 matrix shown by equation (8-10).

$$X = [x_0, x_1, x_2, \dots, x_{681}] \quad (8)$$

$$Y = [y_0, y_1, y_2, \dots, y_{681}] \quad (9)$$

$$Z = [z_0, z_1, z_2, \dots, z_{681}] \quad (10)$$

4. Data Filtering

LRF and IMU sensor outputs could be disrupted by noise that are influenced by the factors of the instrument from inside and outside. thus the filters are used to remove the noises. This paper uses two types of filters. Complementary filter applied to the 2 outputs of the IMU sensor (Acceleration and gyro), while 1D gaussian filter is applied to the 2D LRF sensor output.

4.1 Complementary Filter

This filter uses the input of acceleration sensor and gyro sensor to obtain clean output of noise with complementary method. Acceleration sensor measure all forces not only from the gravity vector alone, and easily distracted even with small force. Data from the acceleration sensor only reliable on the long term and the most appropriate filter is a low pass filter to remove noise on acceleration sensor. Gyro sensor measure angular velocity and less affected by external force, but the drift will always produce the result that can not go to zero when the system returns to its original position. Complementary filter utilizes the advantages from the both sensors. On the short term, we use the data from the gyroscope, because it is very precise and not susceptible to external forces. On the long term, we use the data from the accelerometer, as it does not drift. Figure 6 shows a basic diagram of complementary filter.

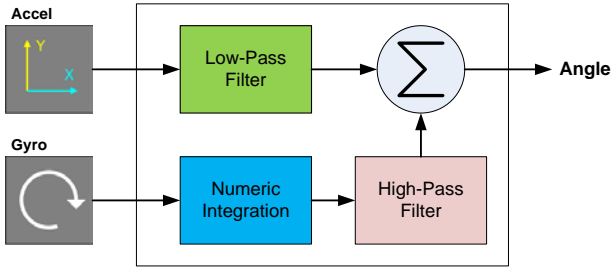


Fig. 6. Basic diagram of complementary filter

The diagram can be translated into mathematical equation as shown by equation 11.

$$angle = (0.98) * (angle + G_{out} * dt) + (0.02) * (A_{out}) \quad (11)$$

Time constant of the filter (τ) could be obtained based on equation 12.

$$\tau = \frac{\alpha \cdot dt}{1 - \alpha} \quad (12)$$

In this work, $dt = 20\text{mSec}$. Thus;

$$\tau = \frac{0.98 \cdot 0.02}{0.02} = 0.98 \text{ sec}$$

This number as threshold value which is used to choose the between accelerometer and gyroscope function. If the value shorter than 0.98 sec, the gyroscope integration function is chosen and the noisy accelerations are filtered out. Otherwise, the accelerometer average function is given more weighting than the gyroscope.

4.2 Gaussian Filter

This filter is used to smooth the output of LRF sensor. In contrast to the 2D image smoothing method that uses a two-dimension gaussian filter, in this work used a one-dimensional gaussian filter. In mathematics, the 1D gaussian filter is written as shown by equation 13.

$$G(x) = \frac{1}{\sqrt{2\pi\sigma^2}} e^{-\left(\frac{x^2}{2\sigma^2}\right)} \quad (13)$$

Where σ is the standard deviation of the distribution. The distribution is assumed to have a mean (μ) of 0.

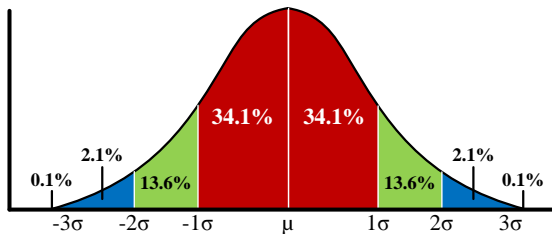


Fig. 7. Gaussian distribution function

The Standard deviation of the Gaussian function gives an important role in its action. The values located between $\pm 1\sigma$ from the mean (red) account for 68% of the set, while $\pm 2\sigma$ from the mean (red and green) account for 95%, and $\pm 3\sigma$ from the mean (red, green and blue) account for 99.7%. Figure 7 shows gaussian distribution function.

5. Experimental Results

5.1 2D Polar to Cartesian

Output of LRF sensors Hokuyo URG-04LX in the form of a 2D polar coordinate converted into 2D Cartesian coordinate using equation 1 and 2. Figure 8 shows the experimental results of 2D data acquisition.

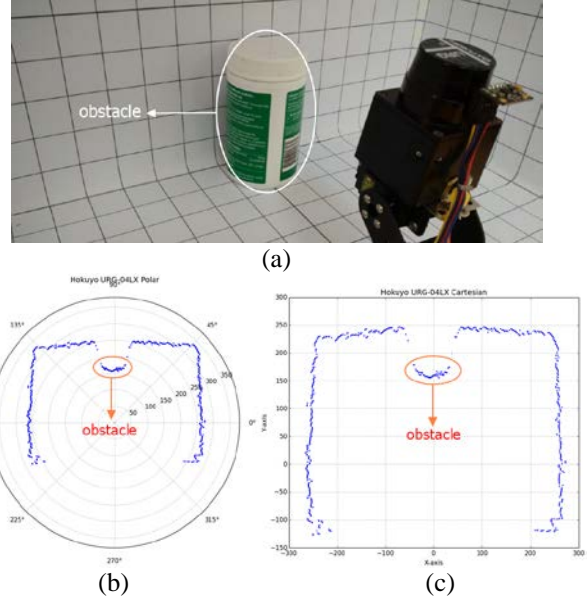


Fig. 8. (a) Obstacle pose (b) Polar plot (c) Cartesian plot

5.2 Output Smoothing of LRF Sensor

Noises at the output of LRF sensor are difficult to avoid and it is strongly influenced by the surfaces characteristic from the observed object, such as color and reflectivity of the light [11][12]. So it requires process of smoothing for the output of the LRF sensor. Gaussian filter is used in this work. Equation 13 shows the mathematical functions from the 1D gaussian filter. Figure 9 shows the results of filtering using 1D gaussian filter for the value of $\sigma = 3$ and 7.

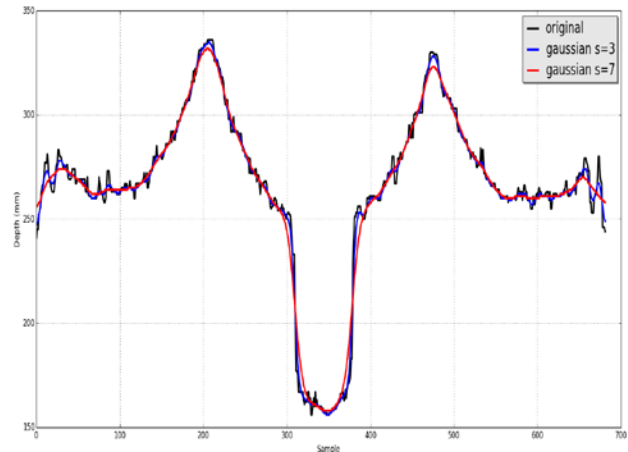


Fig. 9. 1D gaussian smoothing filter comparison

Based on the figure 9, with the value of sigma = 7 has provided a better filter output when compared with the value of sigma = 3. This is indicated by the number of ripples that occur throughout the measurement data.

5.3 Construct 3D Image

After filtering the output of the LRF sensor using 1D gaussian filter, the next step is building a 3D image based on the equation 5,6,7 from the several point of the angle of inclination (φ) which is read by the IMU sensor. Figure 10 shows the 3D image which successfully constructed.

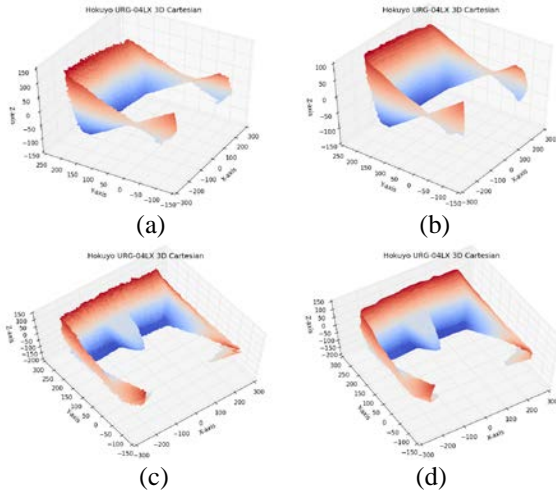


Fig. 10. 3D image build (a) No obstacle – prior filtering (b) No obstacle – post filtering (c) With obstacle – prior filtering (d) With obstacle – post filtering

6. Conclusions

This paper presents a method of 3D image acquisition using 2D LRF sensor Hokuyo URG-04LX sensor with tilt servo mechanism which obtain correction tilt angle from the IMU sensor MPU6050. Filtering process was carried out to eliminate noise (smoothing), both from outputs of the IMU sensors and LRF sensor. Complementary filter does not much discussed in this paper and specifically discussed in another paper. In this work, LRF sensor output smoothed using a 1D gaussian filter. Based on the results of trials in 1D gaussian filter, better results are obtained with a value of $\sigma = 7$. Further research, developed a 3D SLAM with Kalman prediction to produce a better 3D map, and develop an object segmentation method which is used in the robot path planning.

References

- [1] D. F. Wolf, G. S. Sukhatme, and S. Member, "Semantic Mapping Using Mobile Robots," *IEEE Trans. Robot.*, vol. 24, no. 2, pp. 245–258, 2008.
- [2] C. Chen and Y. Cheng, "Research on Map Building by Mobile Robots," *IEEE - Second Int. Symp. Intell. Inf. Technol. Appl.*, pp. 673–677, Dec. 2008.
- [3] B. B. Cortes, U. Valle, B. Piv, and X. C. Solé, "Indoor SLAM using a Range-Augmented Omnidirectional Vision," in *IEEE International Conference on Computer Vision Workshops*, 2011, pp. 280–287.

- [4] M. Bosse, R. Zlot, and P. Flick, "Zebedee : Design of a Spring-Mounted 3-D Range Sensor with Application to Mobile Mapping," *IEEE Trans. Robot.*, vol. 28, no. 5, pp. 1104–1119, 2012.
- [5] S. Oßwald and A. Hornung, "Autonomous Climbing of Spiral Staircases with Humanoids," *IEEE/RSJ Int. Conf. Intell. Robot. Syst. Sept. 25-30. San Fr. CA, USA*, pp. 4844–4849, 2011.
- [6] Y.-S. Hawng, K. Hyun-Woo, and J.-M. Lee, "A 3D Map building algorithm using a single LRF on a mobile robot," in *9th International Conference on Ubiquitous Robots and Ambient Intelligence (URAI)*, November 25-29, Daejeon, Korea, 2012, vol. 1, pp. 321–324.
- [7] D. Magree and E. N. Johnson, "Combined Laser and Vision-aided Inertial Navigation for an Indoor Unmanned Aerial Vehicle," in *American Control Conference (ACC) June 4-6. Portland, Oregon, USA*, 2014, pp. 1900–1905.
- [8] H. Kawata, A. Ohya, S. Yuta, W. Santosh, and T. Mori, "Development of ultra-small lightweight optical range," in *IEEE International Conference on Intelligent Robots and Systems (IROS)*, 2005, no. 42 50, pp. 1078 – 1083.
- [9] InvenSense, "MPU-6000 and MPU-6050 Product Specification Rev 3.4," 2013.
- [10] M. Ogaz, R. Sandoval, and M. Chacon, "Data Processing from a Laser Range Finder Sensor for the Construction of Geometric Maps of an Indoor Environment," in *Midwest Symposium on Circuits and Systems*, 2009, pp. 306–313.
- [11] L. Kneip, F. Tache, G. Caprari, and R. Siegwart, "Characterization of the compact Hokuyo URG-04LX 2D laser range scanner," in *IEEE International Conference on Robotics and Automation*, 2009, pp. 1447–1454.
- [12] Y. Okubo, C. Ye, and J. Borenstein, "Characterization of the Hokuyo URG-04LX Laser Rangefinder for Mobile Robot Obstacle Negotiation," 2009, vol. 7332, pp. 1–10.

Simulation Study of Space Robot Dynamics

Md. Mahmud Hasan¹ and Shafina Sultana²

¹Dept. of Information Technology and Mathematical Modeling, International IT University
050040, 34A Manas/8A Dzhandossov St, Almaty, Kazakhstan

²Dept. of Computer Engineering, Kazakh-British Technical University, 59 Tole-bi Street, 050000
Almaty, Kazakhstan
(Email: mail2mahmud@gmail.com)

Abstract - The attempt of this simulation study was to test the capability of the Virtual Manipulator (VM) ideas as originally proposed by Vafa and Dubowsky, (1987, 1988, 1990). It has been observed that the fixed-base manipulator's dynamic formulations are not suitable for the space manipulator consideration. The dynamic problems of the space manipulator requires a unique solution to be undertaken. The dynamic formulations for these systems are complex. Several simulation tests has been performed over the free-floating space robotics system, whereby the spacecraft's angular velocity was fixed. The most beneficial knowledge of this simulation test was the total understanding of the dynamic behavior of space-robotic systems that comprises of space manipulator and the space platform. It appears that the proposed Virtual Manipulator concepts had further enhanced the understanding of space manipulator systems.

Keywords – Space Robotics, Dynamics, Virtual Manipulator, free-floating robot.

1. Introduction

The control of space manipulators poses planning and control problems that are not found in terrestrial fixed-base manipulators due to the dynamic coupling of space manipulators and its spacecraft. There have been several control techniques that has been proposed by previous researchers, which can be subdivided into three categories. In the first category, the spacecraft position and attitude are controlled by reaction jets to compensate for any manipulator dynamics forces exerted on the spacecraft. In this case, the control laws for earth-bound manipulators can be used. However, the utility of such systems can be limited. This is because the manipulator's motions can both saturate the reaction jet system and consume relatively large amount of attitude control flue, limiting the usefulness of the system [1]. In the second category, the spacecraft attitude is controlled, using reaction wheels or attitude control jets in a non translation manner [2][3]. The control problem of these systems can be simplified using the Virtual Manipulator (MV)

technique [3][4][5][6]. The third proposed category assumes a free-floating system in order to conserve fuel or electrical power [7][6]. Such a system permits the spacecraft to move freely in response to manipulator motions. This mode becomes feasible when no external forces and torques act on the system, and when its total momentum is negligible, since the spacecraft's attitude control system does not operate during this mode of space manipulation. In practice, momentum dump maneuvers would be employed to remove any momentum that may accumulate [8]. In this light, two identification methods for space robots can be used. In the first method the space robot manipulators can be considered on an initially fixed base. The dynamic parameters of these space robots can be determined from the relations between motions of a manipulator and applied joint forces and/or torques. In the second method, a novel identification method for space robots can be proposed which can freely move in both translational and rotational directions. This method is based upon the conservation laws of linear and angular momentum of a space robot. In a free-flying space manipulator system, and during the activity of its manipulator, the position and attitude of the system's spacecraft is controlled actively by reaction jets. The free-floating space robotic system is one in which the spacecraft's position and attitude are not actively controlled during manipulator activity to conserve attitude control fuel.

In cases where there are external forces and torques acting on the system, such as forces caused by reaction jets or by contact with external object the VB (Virtual Base) will accelerate and change its position in inertial space. The VB accelerations are proportional to the external forces on the manipulator/spacecraft. The forces and torques will also rotate the system about the center of mass. The systems considered are assumed to be free-floating, and hence the virtual manipulator base will be a VG (Virtual Ground) shown in Fig 1.

2. Dynamic of Base-Fixed Manipulators

Kinematic and kinetic (dynamic) characteristics of a manipulator will have a major influence on the base-fixed manipulator operation. The physical and geometric parameters such as masses, moments of inertia and link dimensions are used to identify the dynamics parameters of a base-fixed robot. The equation of motion of free-floating systems with no external forces or moments can be formulated as follows:

$$\tau = M(q)\ddot{q} + h(q, \dot{q}) \quad (1)$$

where $M(q)\ddot{q}$ is the inertia matrix and $h(q, \dot{q})$ is the centrifugal and Coriolis term.

The dynamic analysis of a base-fixed manipulator can be achieved by considering a satellite base fixed on an inertial foundation with two links of the manipulator moving in a plane. The first and second joint angles are denoted as $q = (q_1, \dots, q_n)^T$ and its corresponding joint torques as $\tau = (\tau_1, \dots, \tau_n)^T$. The superscript T indicates the transpose of a vector. Again by adding the joint frictional resistant torque the dynamic equations of motion of the manipulator can be re-described as follows:

$$M(q)\ddot{q} + h(q, \dot{q}) + f_f = \tau \quad (2)$$

where

$$M(q) = \begin{bmatrix} m_{11} + 2m_c \cos q_2 & m_{22} + m_c \cos q_2 \\ m_{22} + m_c \cos q_2 & m_{22} \end{bmatrix} \quad (3)$$

is the standard inertial matrix of the manipulator. The vector $h(q, \dot{q})$ represents the centrifugal and Coriolis' forces, and that is:

$$h(q, \dot{q}) = \begin{bmatrix} -m_c \sin q_2 \dot{q}_2^2 - 2m_c \sin q_2 \dot{q}_1 \dot{q}_2 \\ m_c \sin q_2 \dot{q}_2 \end{bmatrix} \quad (4)$$

The vector f_f is the joint frictional resistant torque defined as

$$f_f = \begin{bmatrix} f_{v1} \dot{q}_1 \\ \cdot \\ \cdot \\ f_{vn} \dot{q}_n \end{bmatrix} + \begin{bmatrix} f_{c1} \\ \cdot \\ \cdot \\ f_{cn} \end{bmatrix} \quad (5)$$

The first term of the right hand side of the equation denotes viscous damping torques and the second term the Coulomb damping torques m_{11}, m_{22} and m_c which are the dynamic parameters of the manipulator. Note that the $f_{v1}, \dots, f_{vn}, f_{c1}$ and \dots, f_{cn} are the frictional parameters.

In the analysis, the base reactions of a space manipulator are directly transmitted to the supporting structure, which is generally part of the space vehicle or space station. These base reaction forces are in fact disturbance that can have significant adverse effects on the control and performance of the space robot. Clearly, it is not trivial to take into account the reaction force on the space structure in the associated control schemes. Furthermore, since the coupling between the manipulator and the space structure is dynamic in nature, the performance of the manipulator will also be affected by these dynamic interactions. It follows that, ideally, one would desire zero base reactions for robot manipulators used in space applications.

3. Dynamic of Free-Floating Space Robots

Consider a platform/manipulator system as shown in Fig 1. Suppose there are no external forces acting on the system, the system Center of Mass (CM) does not accelerate, and the system linear momentum is constant, i.e., ${}^0\dot{r}_{cm} = 0$. With the further assumption of zero initial momentum, the system CM remains fixed in inertial space, and can be taken as the origin of a fixed frame of reference.

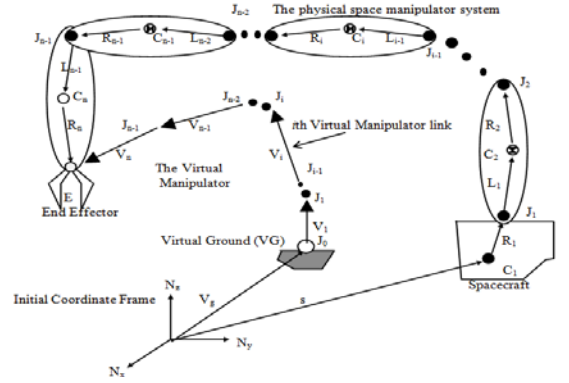


Fig 1. The VM concept for the space robot.

The spacecraft's initial position and orientation in body fixed axes are $X_b = [x, y, z]^T$, and $R_b = [\phi, \theta, \psi]^T$, respectively. The manipulator joint angles are $q = [q_1, q_2, \dots, q_n]^T$. Infinitesimal changes in the spacecraft's attitude measured with respect to its body-fixed axes, δb^c , can be expressed as a function of infinitesimal manipulator joint motions, δq , as $\delta b^c = G(q)\delta q$, where G is a 3 by N disturbance sensitivity matrix (Vafa and Dubowsky, 1990). The vector δb^c is defined as the instantaneous disturbance.

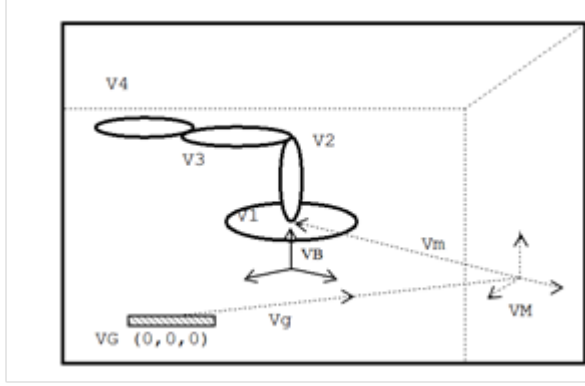


Fig 2. Satellite platform and the manipulator arm.

The end-effector inertial linear and angular velocities, \dot{r}_E , and, ω_E are functions of the joint rates \dot{q} and of the spacecraft angular velocity, ${}^0\omega_0$, as,

$$[\dot{r}_E, \omega_E]^T = J^* \dot{q} \quad (6)$$

The conservation of angular momentum is,

$${}^0\omega_0 = -{}^0D^{-1} {}^0D_q \dot{q} \quad (7)$$

where 0D is the 3 by 3 system inertia matrix with respect to the system CM, and as such it is a positive definite symmetric matrix. The 0D_q is a 3 by N matrix. The matrices 0D and 0D_q are the functions of the configuration q . The inverse of 0D always exist because the system inertia matrix is positive definite. Equation (7) can be used to express ${}^0\omega_0$ from

$$v_E = J^+ v = [\dot{r}_E^T, \omega_E^T]^T \quad (8)$$

where v_E is the end-effector velocity and J^+ is the 6 by $N+6$ non-square matrices, even when $N=6$. Again, ${}^0\omega_0$ is a function of \dot{q} , which can be used to derive a free-floating system's Jacobian J^* , defined by,

$$[\dot{r}_E, \omega_E]^T = J^* \dot{q} \quad (9)$$

where J^* is a $6 \times N$ matrix given by,

$$J^*(\theta_s, q) = \text{diag}(T_0(\theta_s), T_0(\theta_s)) {}^0J^*(q) \quad (10)$$

Since Eq. (6) was used in constructing J^* , this Jacobian depends not only on the kinematic properties of the system, but also on configuration dependent inertias. Therefore, the

singular configuration for a free-floating system, i.e., ones in which ${}^0J^*$ has rank less than six, are not the same to the ones for fixed based systems, as they depend on the mass distribution.

The equations of motion for a free-floating system can be found either using a Lagrangian approach or by setting all external forces and moments equal to zero. The resulting equation becomes,

$$\tau = M(q)(\ddot{q}) + h(q, \dot{q}) \quad (11)$$

where $M(q)(\ddot{q}) \equiv {}^0D_q {}^0D_q^T {}^0D^{-1} {}^0D_q$ is the reduced system inertia matrix, and $h(q, \dot{q})$ contains the non-linear centrifugal and Coriolis terms. The vector τ is the manipulator joint force/torque vector $[\tau_1, \tau_1, \dots, \tau_N]^T$. Therefore, $M(q)(\ddot{q})$ is the $N \times N$ positive definite symmetric inertia matrix, which depends on q and the system mass properties, as defined in Eq. (3).

4. Simulation Results

A simulation study was conducted by considering the Puma 560 robot structure shown in Table 1. The VM to an arbitrary point on the real manipulator body, and end-effector VM coincide with the real manipulator end-effector. These VM constructions enable the dynamic motions of a space manipulator system to be described by the motions of its Virtual Manipulator representation that has its base at the VG.

Table 1. The Puma 560 robot's parameter.

i	q _i	a _i (cm)	a _i (deg)	d _i (cm)	Rotor Inertia (kgm ²)	M _i (Kg)
1	var	0	-90	60	2.5x10 ⁻²	1.5
2	var	175	0	0	2.5x10 ⁻³	1.3
3	var	266	0	0	2.5x10 ⁻³	1.2
4	var	0	90	0	1.5x10 ⁻⁴	0.25
5	var	20	0	-55	1.5x10 ⁻⁴	0.12
6	var	0	90	0	7.8x10 ⁻⁵	0.05

The systems Jacobian can be calculated from the Eq. (9) as,

$$\dot{x} = \dot{r}_E = \frac{d}{dt} [x, y, z]^T = J^* \dot{q} \quad (12)$$

where, $x = r_E = [x, y, z]^T$ and $q = [q_1, q_2, q_3, q_4, q_5, q_6]^T$.

Thus the J^* is,

$$J^*(\theta, q) = T_0(\theta)^0 J^*(q) \quad (13)$$

The transformation matrices 0T_i are found according to,

$$\begin{aligned} {}^0T_1 &= \text{Rot}(q_1) \\ {}^0T_2 &= \text{Rot}(q_1)\text{Rot}(q_2) \\ {}^0T_3 &= \text{Rot}(q_1)\text{Rot}(q_2)\text{Rot}(q_3) \\ {}^0T_6 &= \text{Rot}(q_1) \dots \text{Rot}(q_5)\text{Rot}(q_6) \end{aligned} \quad (14)$$

Finally the system Jacobian J^* is,

$$\begin{aligned} {}^0J^*(q) &= \text{Diag}(T_0, T_0)^0 J^*(q) \\ &\equiv \begin{bmatrix} -{}^0J_{11} & {}^0D^{-1} & {}^0D_q + {}^0J_{12} \\ -{}^0D^{-1} & {}^0D_q + {}^0J_{22} \end{bmatrix} \end{aligned} \quad (15)$$

where 0D_j are the inertia matrices corresponding to the scalars ${}^0d_{ij}$ for the planar robot. Thus, the matrices can be given by,

$$\begin{aligned} {}^0D_j &\equiv D_j = \sum_{i=0}^6 {}^0d_{ij} \quad (j=0,1\dots,5,6) \\ D &\equiv D = D_0 + D_1 + \dots + D_5 + D_6 \\ {}^0D_q &= [D_1 + D_2 + \dots + D_5 + D_6] \end{aligned} \quad (16)$$

Finally, from the above Eqs. (13-16), the system Jacobian J^* is assembled.

To demonstrate this space robot dynamic algorithm, the manipulator end-point is commanded to reach the workspace point (200cm, 340cm, 100cm) starting from the initial location of (100cm, 300cm, 300cm) with initial attitude of joint angles. A constant spacecraft angular velocity was considered at the rate of 100 cm/sec. The simulated control algorithm calculates the end-effector inertial position and velocity, x and \dot{x} , by using the control law,

$$\tau = J^{*T} \{ K_p (x_{\text{des}} - x) - K_d \dot{x} \} \quad (17)$$

where, x represents the Cartesian location of the end-effector,

and, x_{des} is the inertial desired point location. The gain matrices K_p and K_d are diagonal. Note that this algorithm will specify the desired end-effector location. The path of the end-effector to the desired location is not specified in advance. If the control gains are large enough, then the motion of the end-point will be a straight line. The torque

vector τ is nonzero until the $(x_{\text{des}} - x)$ and \dot{x} are zero with the vector in the brackets of Eq. (17) being in the null space of J^{*T} . In this space robot dynamic simulations test the control gain matrices used are $K_p = \text{Diag}(25,25,25,5,5,5)$ and

$$K_d = \text{diag}(100,80,60,30,10,10)$$

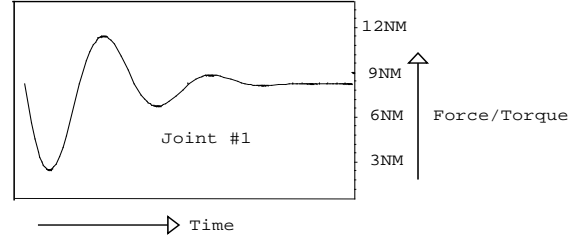


Fig 3. The force/torque profile of joint 1.

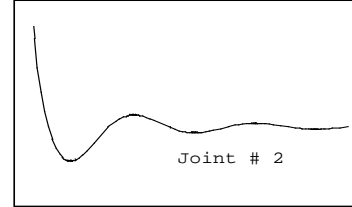


Fig 4. The force/torque profile for joint 2.

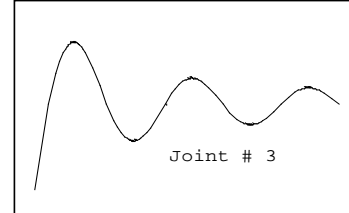


Fig 5. The force/torque profile of joint 3.

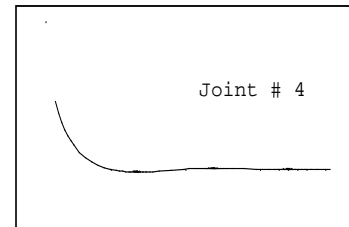


Fig 6. The force/torque profile of joint 4

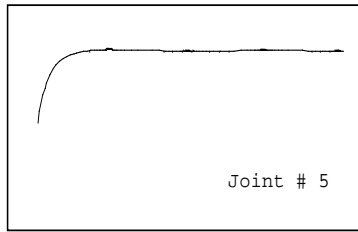


Fig 7. The force/torque profile of joint 5.

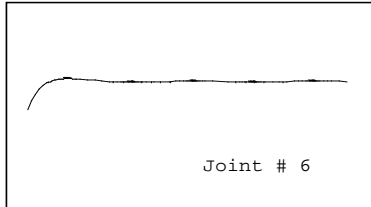


Fig 8. The force/torque profile of joint 6.

The initial joint position of the space manipulator was $(0^0, 90^0, -90^0, 0^0, 0^0, 0^0)$, which reaches the commanded position with the following configuration of $(10^0, -30^0, -15^0, -50^0, 45^0, 25^0)$. The control gain

matrices parameters K_p and K_d has significant effects on the final force/torque value. The space manipulator's system Jacobian was calculated with consideration of the spacecraft angular velocity.

A 3D simulation environment has been developed, where the initial and final position of the space robot has been shown. For this visual simulation purpose a 3-DOF manipulator with base attached to a large platform was considered. The simulated system parameter values are shown in Table 2. The mass of the manipulator is less than 10% of the total system mass. The equations describing the system are derived using Mathematica. The moment of inertia considered for the link one is much more than the link 2 and 3. The link one is body attach joint with the space platform and links 2 and 3 are the robot joints in the zero gravity environment.

Table 2. The robot parameter values.

Link	Mass (m kg)	Moment of Inertia (I) kgm^2	Length of link (d) cm
1	30	5	0
2	1.5	2.5×10^{-2}	60
3	1.3	2.5×10^{-3}	175

For simulation purposes the initial and final configurations are chosen as follows. Figure 9 show the starting from the initial configuration at the top left, desired final configuration (as shown the joint angle values) was achieved as shown in the bottom right snapshot.

$$\theta_0 = \begin{bmatrix} 45.0^0 \\ -10.0^0 \\ 90.0^0 \end{bmatrix} \text{ and } \theta_f = \begin{bmatrix} -30.0^0 \\ 0.0^0 \\ 90.0^0 \end{bmatrix}$$

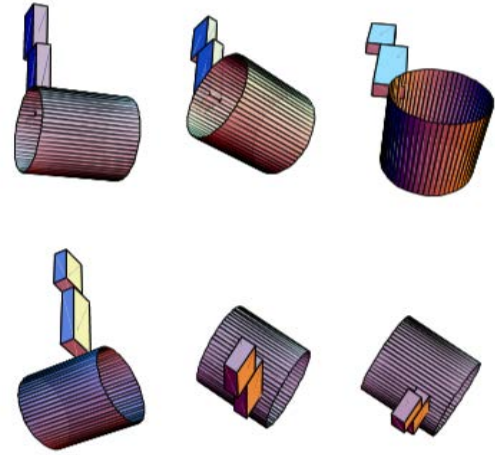


Fig 9. Snapshots of 3D simulation

This simulation indicates that the space platform's attitude of such space robotic system depends upon the motion of the manipulator. The means the attitude control of a space manipulator can only be possible through internal motion of the space manipulator.

5. Conclusion

The attempt of this simulation study was to test the capability of the Virtual Manipulator (VM) ideas as originally proposed by Vafa and Dubowsky, (1988, 1987, 1990). It was observed that the base-fixed manipulator's dynamic formulations are not suitable for the space manipulator consideration. The dynamic problems of the space manipulator requires a unique solution to be undertaken. The dynamic formulations for these systems are complex. Several simulation tests were performed over the free-floating space robotics system, whereby the spacecraft's angular velocity was fixed. The most beneficial knowledge of this simulation test was the total understanding of the dynamic behavior of these systems. It appears that the proposed Virtual Manipulator concepts had further enhanced the understanding of space manipulator systems.

References

- [1] Dubowsky, S., Vance, E., and Torres, M., (1989) "The control of space manipulators subject to spacecraft attitude control saturation limits", *Proc. of the NASA Conference on space Telerobotics*, JPL, Pasadena, CA. Jan 31- Feb. 2.
- [2] Dubowsky, S., and Torres, M., (1990) "Path planning for space manipulators to minimize the use of attitude control fuel", *Proc of the Inter. Symposium on Artificial Intelligent Robotics and Automation in Space (I-SAIRAS)*, Kobe, Japan.
- [3] Vafa, Z., and Dubowsky, S., (1987) "On the dynamics of manipulators in space using the virtual manipulator approach", *Proc. of the IEEE Inter. Conference on Robotics and Automation*, Raleigh, NC.
- [4] Dubowsky, S., and Vafa, Z., (1987) "A virtual manipulator for space robotics system", *Proc. of the workshop on space telerobotics*, Pasadena, CA.
- [5] Vafa, Z., and Dubowsky, S., (1990) "On the dynamics of space manipulators using the virtual manipulator, with applications to path planning", *The Journal of Astronautical Science*, 4(38): 441-471.
- [6] Vafa, Z., and Dubowsky, S., (1990) "The kinematics and dynamics of space manipulators: the virtual manipulator approach", *The Inter. Journal of Robotics Research*, 4(9): 3-21.
- [7] Nakamura, Y., and Mukherjee, R., (1989) "Nonholonomic path planning of space robots", *Proc. of the IEEE Inter. Conference on Robotics and Automation*, Scottsdale, AZ.
- [8] Papadopoulos, E., (1990) "On the dynamics and control of space manipulators", Ph.D. Thesis, *Department of Mechanical Engineering*, MIT.

CRUSC 2014 at a Glance



Organized by:



ISBN978-967-0691-42-8

